

Discovering the world of non-toxic nanocrystals

Synthesis and luminescence of CuInS_2 nanocrystals



Master thesis

Anne C. Berends

July 11, 2014

Supervisors:

Ward van der Stam, MSc

Dr. Celso de Mello Donegá

Condensed Matter and Interfaces
Debye Institute for Nanomaterials Science



Universiteit Utrecht

Abstract

In this master thesis, the optical properties of colloidal copper indium sulfide (CIS) nanocrystals (NCs), directly synthesized following a heating-up protocol or prepared *via* cation exchange, are described. The influence of the synthesis variables, such as reaction time and temperature, precursors and precursor ratios and reaction atmosphere are studied, aiming at understanding the formation mechanisms. Not only colloidal CIS NCs are synthesized and studied, also copper indium zinc sulfide alloy NCs, CIS/ZnS and CIS/CdS core/shell NCs are prepared following a heating-up and hot-injection protocol and the changes in luminescence characteristics are analyzed. The absorption and emission spectra and exciton lifetimes measured not only provide the optical characteristics of the NCs, but also form a start of understanding the electronic structure of the CIS NCs and the origin of their photoluminescence.

It is observed that the higher the indium concentration in the NCs is, the brighter the luminescence is. NCs with an excess of copper show no photoluminescence at all. The CIS NCs prepared *via* cation exchange possess similar structural and optical characteristics with those obtained *via* direct synthesis. Copper indium zinc sulfide alloy NCs are formed after an exchange of indium for zinc and these alloyed NCs show an even brighter luminescence. The luminescence of the CIS/ZnS and CIS/CdS core/shell NCs is stable under air and shows a very bright luminescence as well. CIS/CdS core/shell NCs show a large Stokes shift and long exciton lifetimes, which is consistent with previous works and characteristic for the Type II band alignment. Finally, Cu_{2-x}S -CIS heteronanorods are synthesized following a heating up and seeded injection protocol. The formation of the heteronanorods is a three step process: first copper-dodecanethiol precursor complexes develop, after which Cu_{2-x}S NCs form from these complexes and finally CIS crystals grow epitaxially on these Cu_{2-x}S NC seeds. The presence of oxygen plays an important role in controlling the reaction rate. To form Cu_{2-x}S NCs Cu^{2+} has to be reduced to Cu^+ . Under an oxidizing atmosphere this process is slow, thereby enabling better control over the size and shape of the Cu_{2-x}S -CIS heteronanorods.

Contents

1. Introduction	1
1.1. What are these 100 pages all about?	1
1.2. References	3
2. Theory	5
2.1. Semiconductor nanocrystals: origin of their properties	5
2.1.1. Electronic energy level structure	5
2.1.2. Electrons and holes	6
2.2. Optical properties of semiconductor NCs	7
2.2.1. Excitation and relaxation processes	7
2.2.2. Decay rates	7
2.2.3. Measuring electronic transitions	8
2.3. Heteronanocrystals	10
2.4. Properties determined by surfactants	11
2.5. Synthesis of colloidal nanocrystals	11
2.5.1. A closer look on the formation of a nanocrystal in solution	11
2.5.2. Cation exchange	13
2.6. Applications of colloidal semiconductor nanocrystals	14
2.6.1. Light emitting diodes and displays	14
2.6.2. Solar cells	15
2.6.3. Luminescent solar concentrators	16
2.6.4. Bio-labeling	17
2.7. References	18
3. Synthesis and optical properties of luminescent colloidal copper indium sulfide nanocrystals	21
3.1. Introduction	21
3.2. Experimental	21
3.2.1. Chemicals	21
3.2.2. Synthesis	21
3.2.3. Characterization	22
3.3. Results & discussion	22
3.3.1. Reaction steps	22
3.3.2. Tuning of optical properties	22
3.3.3. Exciton lifetimes	27
3.4. Conclusions & outlook	31
3.5. References	32
4. Synthesis and optical properties of colloidal CIS-based alloy and core/shell nanocrystals..	33
4.1. Introduction	33
4.2. Experimental	33
4.2.1. Materials	33
4.2.2. Synthesis	34
4.2.3. Characterization	35

4.3.	Results & discussion	35
4.3.1.	Reaction steps towards shell formation and competing processes	35
4.3.2.	Cadmium sulfide shell	35
4.3.3.	Precursor reactivity and synthesis temperature	36
4.3.4.	Exciton lifetimes	47
4.4.	Conclusion & outlook	51
4.5.	References	53
5.	Synthesis of CuInS₂ nanocrystals by partial cation exchange in Cu_{2-x}S nanocrystals	55
5.1.	Introduction	55
5.2.	Experimental	55
5.2.1.	Materials	55
5.2.2.	Synthesis	56
5.2.3.	Characterization	56
5.3.	Results & discussion	57
5.3.1.	13-15 nanometer sized nanocrystals at elevated temperatures	57
5.3.2.	4 nanometer sized nanocrystals at elevated temperatures	60
5.3.3.	3 nanometer sized nanocrystals at room temperature	60
5.3.4.	4 and 15 nanometer sized nanocrystals at room temperature	63
5.3.5.	Lattice and crystal structure	65
5.4.	Conclusion & Outlook	66
5.5.	References	68
6.	Colloidal Cu_{2-x}S-CIS heteronanorods	69
6.1.	Introduction	69
6.2.	Experimental	70
6.2.1.	Materials	70
6.2.2.	Synthesis	70
6.2.3.	Characterization	70
6.3.	Results & discussion	71
6.3.1.	Reaction steps and synthesis variables	71
6.3.2.	Seeded injection	82
6.3.3.	Self-assembly	83
6.4.	Conclusion & Outlook	84
6.5.	References	85
7.	Acknowledgments	87
8.	Appendices.....	88

1. Introduction

1.1. What are these 100 pages all about?

Colloidal semiconductor nanocrystals (NCs) are very small ($1 \text{ nm} = 1 \cdot 10^{-9} \text{ m}$) crystals in the size range of 1 to 50 nanometer and made of a semiconductor material that can be dispersed in a liquid medium. The research into these colloidal semiconductor NCs is booming since the beginning of the '90s, when the improbable but amazing properties of materials at this length scale were discovered.^{1,2} At the nanoscale semiconductor materials are in the gray area between molecular and macroscopic properties. Characteristics such as band gap, melting temperature and magnetism, suddenly become size dependent, allowing them to be tuned by synthesis procedures that control the size and shape of the nanocrystals. Over the years, many researchers around the world looked into these materials with great success. As we speak, only 30 years after the first fundamental discoveries,³ colloidal NCs are already used in commercial products such as LEDs^{4,5} and in bio-imaging.^{6,7} Extensive research is being done to implement them in solar cells^{8,9} and lasers¹⁰ (see Figure 1.1). The most studied materials (and therefore today's most used ones) are those containing cadmium, such as cadmium sulfide, cadmium selenide and cadmium telluride¹¹ or lead in photovoltaic applications.^{12,13} Since cadmium and lead are very toxic elements^{14,15} the search for alternative colloidal semiconductor NCs based on non-toxic elements and

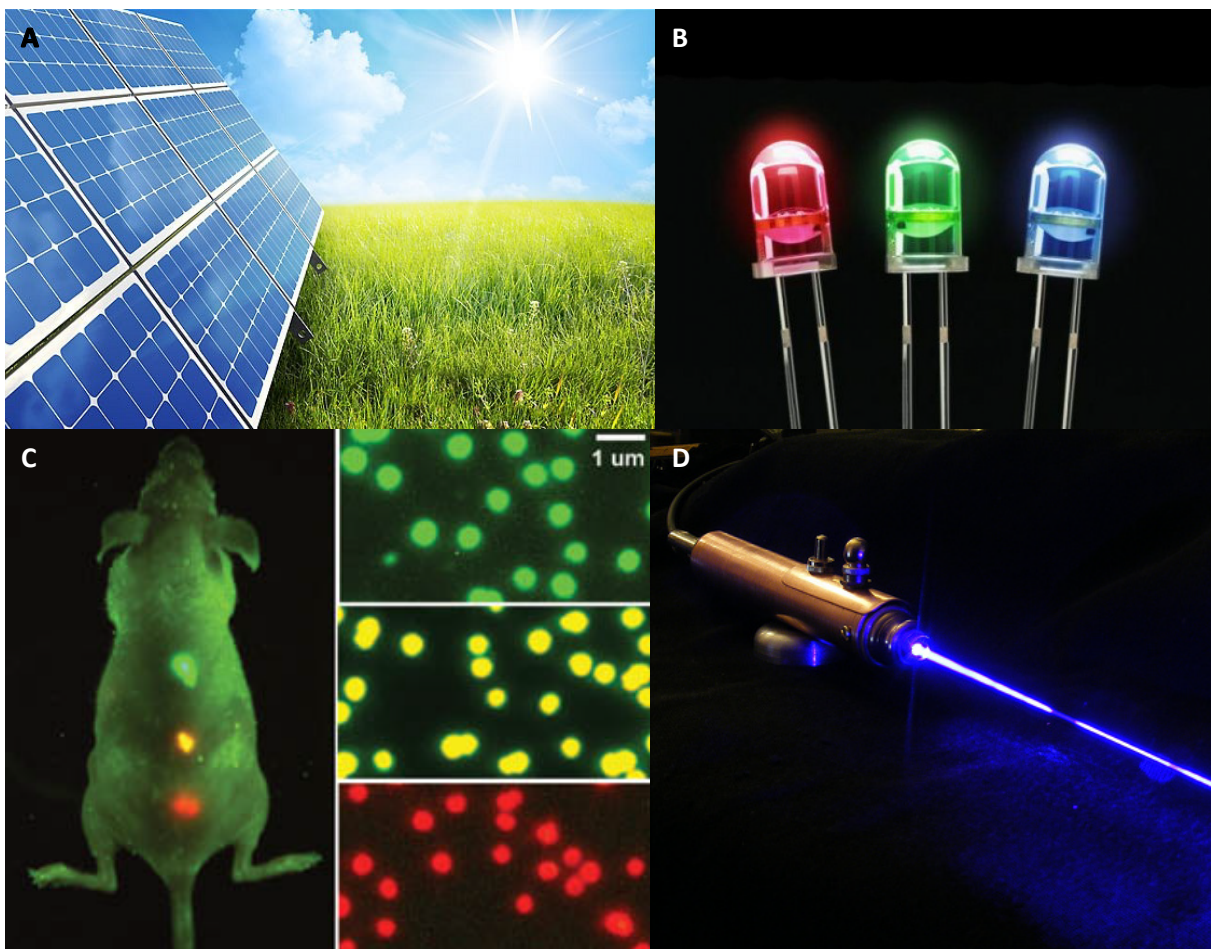


Figure 1.1. A: The well known crystalline silicon solar cell. Reproduced from ref. [16]. B: Bright LEDs not yet making use of NC science. Reproduced from ref. [17]. C: Example of in vivo imaging, making use of colloidal NCs. Reproduced from ref. [18]. D: A blue laser, not making use of NCs. Reproduced from ref. [19].

possessing the same, or even better, optoelectronic properties, is of major importance.

Copper indium sulfide (CIS) is a semiconductor material that shows optical properties at the nanoscale similar to the cadmium containing nanocrystals, but is made of non-toxic elements. However, although several papers on the synthesis and properties of CIS NCs are published²⁰ little is known about the influence of synthesis conditions on the resulting NC size, shape, stoichiometry and optical characteristics; let alone about ways to improve these properties to meet requirements for industrial and commercial products. It will thus not come as a surprise that the synthesis and investigation of optical properties of colloidal CIS NCs is the subject of this thesis, with as goal to provide a thorough analysis of the characteristics and possibilities of colloidal CIS NCs.

This thesis is organized as follows. In the first chapter some basic and fundamental theory concerning the origin of the changing material characteristics at the nanoscale, so called quantum confinement, will be discussed, as well as fundamentals on NC synthesis and application in devices. In chapter 3 the influence of variations in synthesis parameters on the properties of the resulting colloidal CIS NCs is investigated and a start is made with the analysis of the origin of the emission of CIS NCs. In chapter 4 the influence of alloying with zinc and shell growth on the optical properties of the CIS NCs is described. A completely new way of preparing CIS NCs is *via* cation exchange, a method described in chapter 5 and in chapter 6 the formation mechanism and possible applications of colloidal Cu_{2-x}S -CIS heteronanorods are discussed.

1.2. References

1. Brus, L. Quantum Crystallites and Nonlinear Optics. *Appl. Phys. A* **53**, 465–474 (1991).
2. Alivisatos, A. P. Semiconductor clusters, nanocrystals and quantum dots. *Science* **271**, 933–937 (1996).
3. Brus, L. E. A simple model for the ionization potential, electron affinity, and aqueous redox potentials of small semiconductor crystallites. *J. Chem. Phys.* **79**, 5566 (1983).
4. Shirasaki, Y., Supran, G. J., Bawendi, M. G. & Bulović, V. Emergence of colloidal quantum-dot light-emitting technologies. *Nat. Photonics* **7**, 933–933 (2013).
5. NWO & FOM. Onderzoekers halen meer licht uit LEDs dankzij nanodeeltjes. (2013). at <http://www.fom.nl/live/nieuws/archief_persberichten/persberichten2013/artikel.pag?objectnumber=225228>
6. NOS. Nieuwe diagnose kankeruitzaaiing. (2014). at <<http://nos.nl/artikel/610096-nieuwe-diagnose-kankeruitzaaiing.html>>
7. Bruchez Jr., M., Moronne, M., Gin, P., Weiss, S. & Alivisatos, A. P. Semiconductor Nanocrystals as Fluorescent Biological Labels. *Science* **281**, 2013–2016 (1998).
8. Nozik, A. J. Quantum dot solar cells. *Phys. E Low-dimensional Syst. Nanostructures* **14**, 115–120 (2002).
9. NU.nl & Soeteman, K. Efficiëntere zonnecellen door nanodraadjes. (2013). at <<http://www.nu.nl/wetenschap/3379231/efficiëntere-zonnecellen-nanodraadjes.html>>
10. Klimov, V. I. Optical Gain and Stimulated Emission in Nanocrystal Quantum Dots. *Science* **290**, 314–317 (2000).
11. Zhang, F., Yi, D., Sun, H. & Zhang, H. Cadmium-Based Quantum Dots: Preparation, Surface Modification, and Applications. *J. Nanosci. Nanotechnol.* **14**, 1409–1424 (2014).
12. Atomsa Gonfa, B. et al. Air-processed depleted bulk heterojunction solar cells based on PbS/CdS core–shell quantum dots and TiO₂ nanorod arrays. *Sol. Energy Mater. Sol. Cells* **124**, 67–74 (2014).
13. Ma, W. et al. Photovoltaic performance of ultrasmall PbSe quantum dots. *ACS Nano* **5**, 8140–7 (2011).
14. MSDS - Sigma-Aldrich - Cadmium. Mater. Saf. Data Sheet (2013). at <<http://www.sigmaaldrich.com/MSDS/MSDS/DisplayMSDSPage.do?country=NL&language=nl&productNumber=265365&brand=ALDRICH&PageToGoToURL=http://www.sigmaaldrich.com/catalog/product/aldrich/265365?lang=en>>
15. MSDS - Sigma-Aldrich - Lead. Mater. Saf. Data Sheet (2014). at <<http://www.sigmaaldrich.com/MSDS/MSDS/DisplayMSDSPage.do?country=NL&language=nl&productNumber=391352&brand=ALDRICH&PageToGoToURL=http://www.sigmaaldrich.com/catalog/product/aldrich/391352?lang=en>>
16. Trebuchet. EVOLUTION INSPIRES MORE EFFICIENT SOLAR CELLS. (2013). at <<http://www.trebuchet-magazine.com/evolution-inspires-more-efficient-solar-cells/>>
17. Reefbuilders & Bentley, C. The LED as we know it turns 50 today. (2012). at <<http://reefbuilders.com/2012/10/09/led-turns-50-today/>>

18. Henry, C. Targeting Cancer Cells. (2004). at <<http://pubs.acs.org/cen/news/8229/8229qdots.html>>
19. Harris, L. Violet Laser- Beam and Housing 2. (2008). at <<https://www.flickr.com/photos/ima-jilon/3108908751/>>
20. Kolny-Olesiak, J. & Weller, H. Synthesis and application of colloidal CuInS₂ semiconductor nanocrystals. *ACS Appl. Mater. Interfaces* **5**, 12221–37 (2013).

2. Theory

2.1. Semiconductor nanocrystals: origin of their properties

2.1.1. Electronic energy level structure

To explain the observed unique properties for semiconductor materials on the nanoscale, either a top-down or bottom-up approach can be used. The first makes use of the known properties of bulk semiconductors, their energy levels and transitions between these levels, the second regards a nanocrystal as a cluster of atoms and assumes that the electronic structure of the NC is built up from the electronic levels of the individual atoms, making use of molecular orbital theory and quantum mechanics. The latter explanation is used in this chapter. When atomic orbitals (AOs) combine, they form molecular orbitals (MOs). The highest molecular orbital that is occupied by electrons is called the highest occupied molecular orbital (HOMO) and the molecular orbital that lies at the lowest energy level that is not occupied, is called the lowest unoccupied molecular orbital (LUMO).¹ When the amount of orbitals is large enough, the discrete energy levels cannot be distinguished anymore and a band of electronic states is formed. The band that originates from the occupied molecular orbitals is called the valence band (VB), the band that originates from the unoccupied molecular orbitals is called the conduction band (CB).¹ Between the two bands is an energy gap: the band gap (E_g). This process is schematically depicted in Figure 2.1A.² Room temperature provides enough thermal energy to allow electrons to move freely through the band. The highest density of electronic states is found in the middle of the bands (see Figure 2.1B). For materials at the nanoscale the density at the edges of the bands is so much lowered compared to bulk, that even discrete energy levels appear³ (see Figure 2.1A and B). These effects (the size dependence of the band gap and the appearance of discrete energy levels) is called the quantum

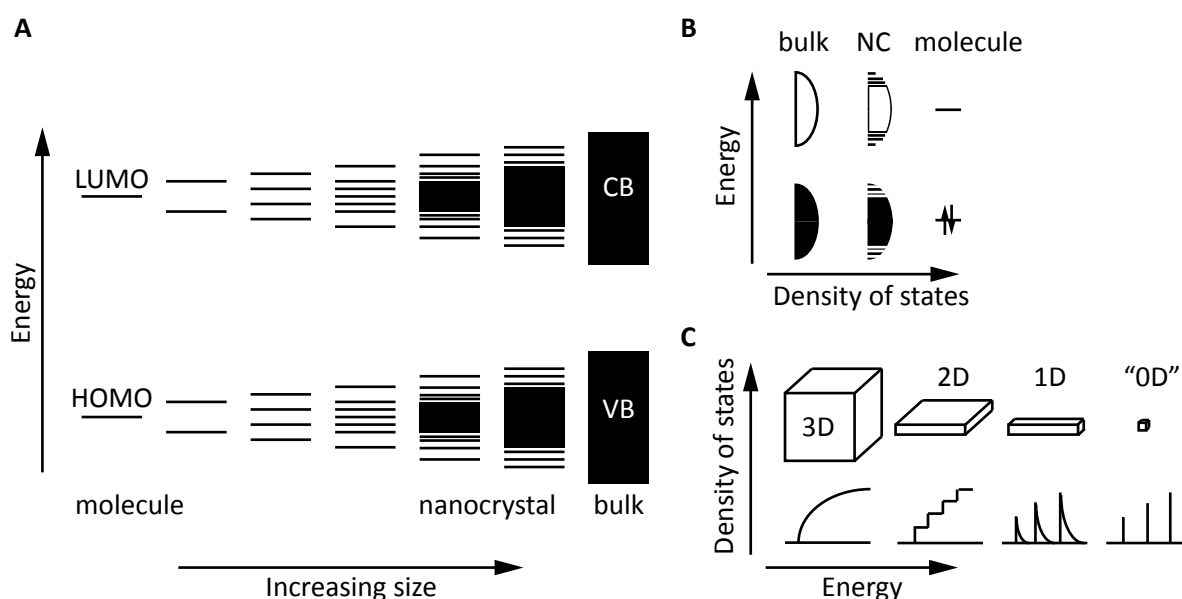


Figure 2.1. A: Schematic representation of LUMO and HOMO levels on molecular level, forming continuous bands with discrete energy levels near the edges in nanocrystals. Adapted from ref. [2]. B: Schematic representation of the density of electronic states in bulk, a nanocrystal and a molecule. Adapted from ref. [3]. C: Density of states in one band of a semiconductor as a function of dimension. Adapted from ref. [3]

size effect, or quantum confinement.

2.1.2. Electrons and holes

In a semiconductor electrons (which have a negative charge) can be promoted (excited) from the VB to the CB when enough energy (light or heat) is added to overcome the band gap energy, leaving a positive charged hole in the VB. Both the electron and hole are treated as particles, whose quantum mechanic characteristics are assembled in a wavefunction. In bulk, an excited electron is due to Coulombic interactions bound to a hole in the VB. This electron-hole pair is called an exciton and can be treated as a particle with a wavefunction as well. The distance between an electron and a hole (the size of the exciton) is given by the electron Bohr radius (a_0) and differs per material. When the size of a NC is smaller than the exciton Bohr radius, the exciton is confined to the NC size, leading to an increase in energy for both charge carriers (electron and hole). This increase in energy is much larger than the Coulombic attraction, which means that the electron and hole then can be treated as independent particles.² The excitation of electrons and recombination of excitons are the key phenomena determining the optical properties of semiconductor NCs. This means that when the size of a NC approaches or is smaller than a_0 and thereby energy levels are altered, the optical properties are subject to (a large) change. In general, materials with a smaller band gap have a larger a_0 and therefore show a change in optical properties at larger NC sizes (Figure 2.2).⁴ For copper indium sulfide a_0 is 4.1 nm⁵ which is comparable with the well-known and often studied cadmium selenide ($a_0 = 4.9$ nm)⁶ and cadmium sulfide ($a_0 = 2.9$ nm).⁷ Depending on the exact shape and dimensions of the semiconductor nanocrystal, the exciton can be confined in three or less dimensions, which influences the density of states (Figure 2.2C) and thereby optical properties.^{8,9} The NCs synthesized, analyzed and discussed in this thesis are all confined in three dimensions.

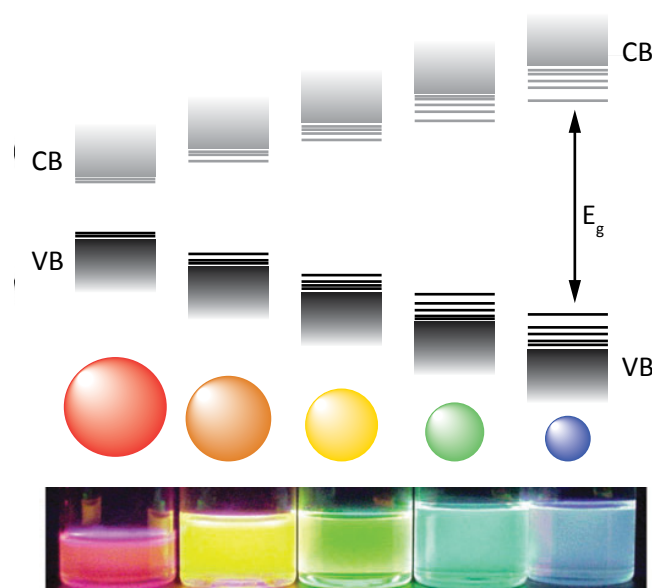


Figure 2.2. Evolution of the band gap, and thereby emission wavelength, with decreasing particle size. Adapted from ref. [4]

2.2. Optical properties of semiconductor NCs

2.2.1. Excitation and relaxation processes

When a photon is absorbed by a semiconductor NC, an electron is excited to a higher energy state and an exciton is created. Depending on the energy of the photon, the electron is promoted from the VB edge to the CB edge (Figure 2.3B) or to higher energy states (Figure 2.3A, which can also happen for the hole). These charge carriers that are located at higher excited states are called ‘hot carriers’, since they relax to the band edge while releasing the excess energy as heat. After relaxation to the band edges, the electron and hole recombine while releasing energy by emitting a photon (Figure 2.3A, radiative recombination) or as heat when coupled to lattice vibrations (Figure 2.3D, non-radiative recombination). When there are localized intra band energy levels present (so called trap states), it is also possible that the electron (or hole) first relaxes to this trap state and then recombines, either radiatively (Figure 2.3C) or non-radiatively. Another decay pathway is energy transfer between different NCs. When two NCs are close together, non-radiative energy transfer can occur, where the exciton moves from a small NC with a large band gap to a large NC with a small band gap. In this larger crystal both charge carriers first relax, thereby losing energy as heat, after which they recombine while emitting a photon (see Figure 2.4A). When two NCs in solution are further away, radiative energy transfer can occur. This is a process whereby an electron of the larger NC with smaller band gap is excited by a photon emitted by a smaller NC, see Figure 2.4B.

2.2.2. Decay rates

Every recombination pathway has a certain probability to happen and therefore a certain rate. This decay rate (w_{tot}) can be measured and is defined as follows:²

$$\tau^{-1} = w_{\text{tot}} = w_{\text{rad}} + w_{\text{non-rad}} + w_{\text{ET}} \quad (1)$$

where τ^{-1} is the decay time, w_{rad} is the radiative decay rate, $w_{\text{non-rad}}$ is the non-radiative decay rate and

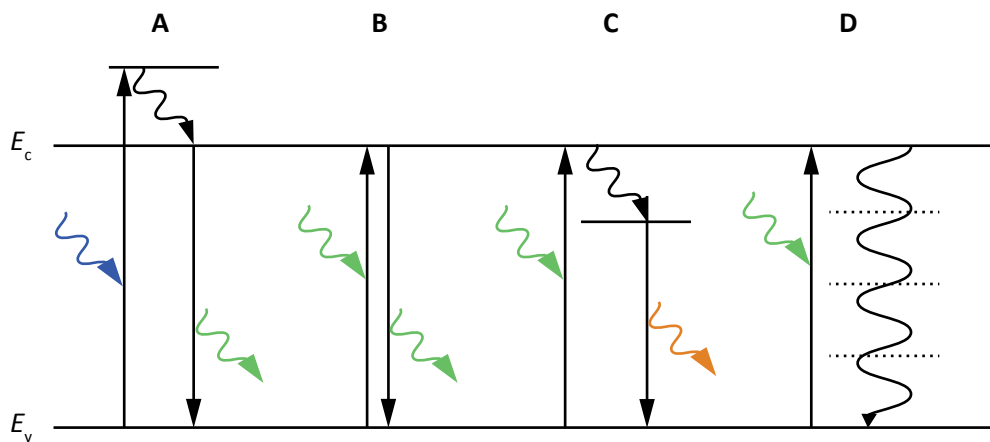


Figure 2.3. Schematic representation of decay and recombination mechanisms. A: Excitation to a higher excited state, thereby creating a ‘hot electron’, followed by non-radiative decay to the CB edge and radiative recombination. The energy of the emitted photon is less than the absorbed photon. B: Excitation to the CB edge followed by radiative band-edge recombination. C: Excitation to the CB edge, followed by non-radiative decay to a trap state and radiative recombination from the trap state to the valence band edge. The energy of the emitted photon is less than the absorbed photon. D: Excitation to the CB edge, followed by non-radiative recombination *via* phonons.

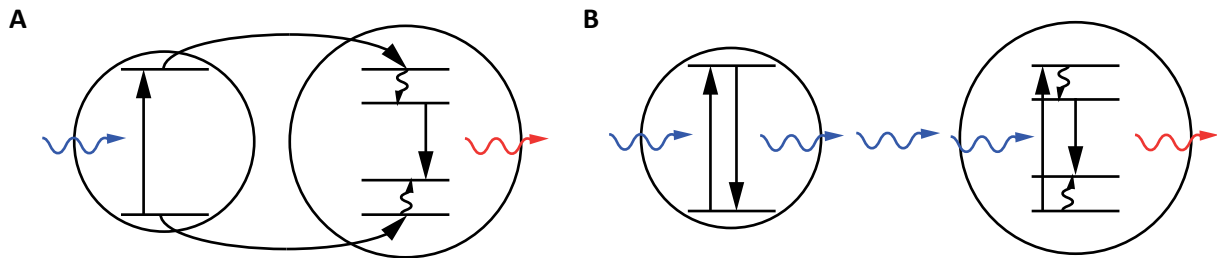


Figure 2.4. A: Schematic representation of non-radiative energy transfer. B: Schematic representation of radiative energy transfer.

w_{ET} is the energy transfer rate. In diluted solutions of NCs the energy transfer rate can be neglected. The lifetime of the exciton τ is determined by the decay channels present and their probability to happen. In the simplest case of band edge excitation and emission (process B in Figure 2.3), the decay rate measured would be a single exponential. When the total exciton lifetime in the ensemble is distributed (i.e. some NCs have fast trap-assisted non-radiative decay and the rest does not) the total decay rate measured consists of more than one component which results in a multi-exponential curve from which the different components can be extracted. This situation is still not too complicated, as schematically depicted in Figure 2.5A and B.

The model becomes more complicated when the electronic structure of the luminescent NC is not straight forward and different trap levels with different properties (i.e. assisting radiative, Figure 2.5C, or non-radiative decay, Figure 2.5B) are present. In the case of CIS NCs the emission is expected to be trap assisted^{10,11} but the exact electronic structure is not known. Interpretation of exciton lifetime measurements is therefore difficult and not unambiguous, as will become clear in later chapters.

2.2.3. Measuring electronic transitions

With spectroscopic measurements the electronic transitions described above can be analyzed. In this section the characteristics of several transitions in absorption and emission spectra will be explained, thereby providing background knowledge to understand the interpretation of spectra later on in this thesis.

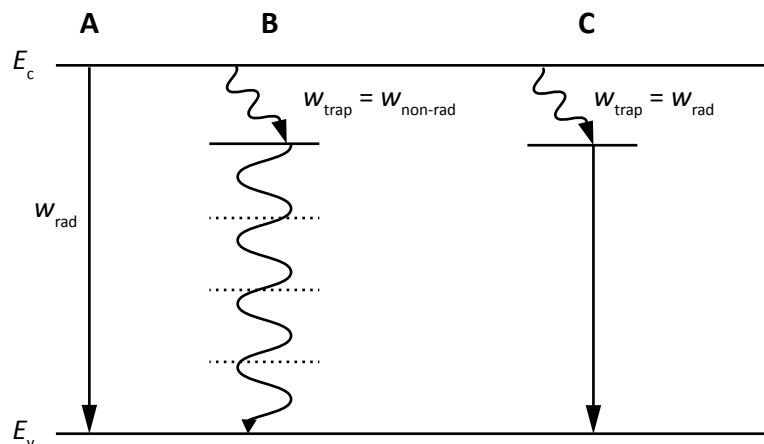


Figure 2.5. Schematic representations of A: Radiative band-edge recombination. B: Non-radiative decay to a trap state followed by non-radiative recombination via phonons. C: Non-radiative decay to a trap state followed by radiative recombination.

In absorption spectra the energies at which an electron can be excited to a higher energy state can be observed. In theory, at every energy corresponding with a transition to a discrete level a peak is observed, but due to coupling to lattice vibrations and size distribution in the ensemble only broad peaks will appear in the spectrum.¹ This phenomenon is known as inhomogeneous line broadening.³ When an ensemble of NCs is measured, the shape of the absorption spectrum that is obtained, is strongly affected by the composition of the ensemble. Transitions in small NCs are more intense and therefore the peaks in an absorption spectrum are observed at relatively short wavelengths with regard to the band gaps that are actually present in the ensemble.⁶ At sufficient high energies the electrons in the NCs are excited to energy states in the bulk-like part of the density of states. At these wavelengths all photons are absorbed, resulting in a continuous high absorption intensity, dominated by the large NCs in the ensemble, due to their volume.⁶

In emission spectra, the energy of the emitted photons can be observed. Again, the size dispersion, and thereby the different band gaps present in the ensemble, broadens the peak that is measured. To ensure that all NCs in the ensemble are excited, the excitation wavelength is chosen at a high energy. Because these photons are more absorbed by the large NCs, their emission at longer wavelengths dominates the spectrum measured.⁶ In concentrated samples energy transfer can take place, which also results in a spectrum measured at relatively long wavelengths. When not only band edge emission takes place, but radiative recombination via trap states is a decay pathway as well (process C in Figure 2.5) the peak arising from this process will be much broader than the peak arising from band edge recombination. Localized trap states vibrate, leading to small deviations in the exact energy level and thus deviations in the energy of the emitted photon. Furthermore, trap states can diffuse through the crystal, a process that also results in alterations of the exact energy level of the state.

With excitation spectroscopy more accurate information on single NC properties can be obtained by an ensemble measurement. In contrast to emission spectroscopy, the ensemble is excited with different energies, while the detection energy of the emitted light is fixed, usually at the energy of maximum emission intensity. Thus, the resulting spectrum shows the emission intensity as function of excitation energy. At lower excitation energies, not the whole ensemble is excited, but only the large NCs with matching small band gaps, thereby preventing a shift to the blue due to the more intense transitions in smaller NCs, the phenomenon observed in an absorption spectrum.

When comparing absorption and emission energies, it is possible to deduce the energy difference of the absorbing and emitting state. This energy difference is called the Stokes shift. As described above, the energy difference in absorption and emission spectra of ensemble measurements is larger than the difference at single crystal level and it is therefore not a good measure for quantitative analysis and modeling. However, this global Stokes shift certainly gives a qualitative indication for the width of the Stokes shift for single NCs.

2.3. Heteronanocrystals

When different semiconductors are joined in one NC via a heterojunction, a hetero NC (HNC) is created. The confinement of the electron and hole depends strongly on the materials chosen and three localization regimes can be distinguished: type I, type I $\frac{1}{2}$ and type II (Figure 2.6A).⁴ In a type I HNC, the band gap of one material lies completely within the band gap of the other material. After excitation both charge carriers are confined in the material with the small band gap. Because of their large wavefunction overlap the radiative recombination is fast or in other words: the exciton lifetime is short. In the type I $\frac{1}{2}$ HNC one of the charge carriers is confined in the core and the other is delocalized over the whole NC.⁴ This leads to longer exciton lifetimes in comparison with type I materials due to less overlap of the electron and hole wavefunctions.⁴ In a type II material the conduction band minimum and the valence band maximum are located in different materials. Therefore the charge carriers become spatially separated and the wavefunction overlap is minimized.^{12,13} This minimization of the wavefunction overlap leads to longer exciton lifetimes and larger Stokes shifts.⁴ The emission wavelength for both the type I $\frac{1}{2}$ and type II HNCs will shift to lower energies compared to the core NC, due to the loss in confinement energy.² Furthermore, the growth of a shell around a luminescent core can increase the luminescent efficiency and stability under air. When charge carriers are confined to the core, they are protected from trap states because the surface dangling bonds of the core are satisfied and the shell protects the core against oxidizing under air.

For copper indium sulfide the bulk band gap is 1.45 eV.⁵ Due to their wider band gap, possible shell materials are zinc sulfide (bulk band gap of 3.9 eV),¹⁴ cadmium sulfide (bulk band gap of 2.4 eV),¹⁴ cadmium selenide (bulk band gap 1.8 eV)¹⁴ and zinc selenide (bulk band gap 2.7 eV).¹⁴ Their relative band offsets are shown in Figure 2.6B. From this figure it becomes clear that only a zinc sulfide shell around

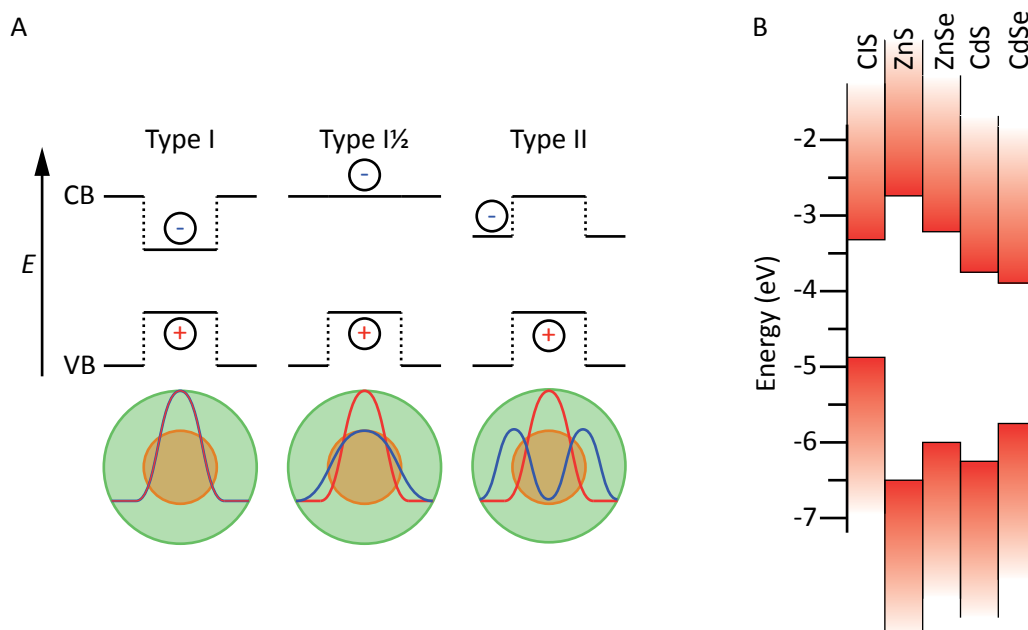


Figure 2.6. A: Schematic representation of the three possible types of band alignment. Reproduced from ref. [4]. B: Band offsets of CIS and often used shell materials. Figure is composed by using data from ref. [15], where the band offsets of CIS and Si were measured, and from ref. [16] where the absolute band positions of the shell materials and Si were calculated.

a CIS core will result in a type I HNC, zinc selenide would result in a type I½ material and both cadmium shells would lead to a type II HNC.

2.4. Properties determined by surfactants

The surface to volume ratio of small crystals is much larger than for bulk material. As a result, surface atoms have a large contribution to the total free energy of the NC. This energy contribution influences properties such as phase transitions, solubility and reactivity.^{3,17} The dangling bonds of surface atoms can form trap states and thereby facilitate non-radiative recombination. To enhance the desired radiative recombination, surface passivation is required. This is achieved by binding the dangling bonds of the surface atoms by organic ligand molecules (surfactants) or growing a shell around the luminescent core. Organic surfactant molecules can bind to surface dangling bonds with head groups containing free electron pairs.⁴ Besides the removal of trap states, surfactants play an important role in growth kinetics (see section 2.5.1 below), solubility in solvents and preventing aggregation by steric hindrance. With ligands binding more or less strongly to monomers, the building blocks of a NC, or crystal facets, the size and shape of the NC can be controlled. Furthermore, surfactants may give rise to a gamut of new functionalities, tunable with their tail groups, such as redox activity,¹⁸ specific bio-imaging applications¹⁹ and inter-NC interaction resulting in super structures²⁰ or enhancement of the conductivity of a larger assembly of NCs.²¹

2.5. Synthesis of colloidal nanocrystals

2.5.1. A closer look on the formation of a nanocrystal in solution

For the formation of small clusters of molecules, atoms or ions in solution, classical nucleation theory states that the total change in free energy consists of a term for the bulk volume (ΔG_v) and a term for the surface (ΔG_s).^{4,22,23} This can be described as follows:

$$\Delta G_{\text{tot}} = \Delta G_v + \Delta G_s = \frac{1}{3}\pi r^3 \rho \Delta\mu + 4\pi r^2 \gamma \quad (2)$$

where r is the radius of the cluster, ρ is the density of the crystalline phase, γ is the interfacial tension between the crystalline phase and the solution and $\Delta\mu$ is the chemical potential difference between the crystalline phase and the monomers in solution, with

$$\Delta\mu = -k_b T \ln(x/x_{\text{sat}}) \quad (3)$$

where x is the concentration in the solution and x_{sat} the saturation concentration. Due to the energy that is released by the formation of chemical bonds, ΔG_v has a negative contribution to ΔG_{tot} . ΔG_s has a positive contribution to ΔG_{tot} due to the unsaturated bonds of the molecules, atoms or ions located at the surface. ΔG_v and ΔG_s have a different sign and scale with a different factor with the radius (r^3 and r^2 respectively). For clusters with a size smaller than a certain r , this means that ΔG_s is dominant and ΔG_{tot} positive. The maximum in ΔG_{tot} (denoted as ΔG_c) is the activation barrier and the corresponding radius is the critical radius r_c . For $r < r_c$ the addition of monomers to the cluster is not energetically favored and

the cluster will break down, while for $r > r_c$ addition of monomers will cause a decrease in ΔG_{tot} and thus this is a spontaneous process,²² see Figure 2.7.

$$r_c = -2\gamma/\rho\Delta\mu \quad (4)$$

From equation 3 follows that higher temperature and higher supersaturation lead to a larger chemical potential difference. From equation 4 then follows that the critical radius will be smaller, leading to smaller clusters.

As in reaction rate theory, the reaction rate is given by the Arrhenius equation²⁴

$$k = A \exp[-E_a/k_B T] \quad (5)$$

the number of critical clusters formed per volume per unit time is given by

$$J = J_0 \exp[-\Delta G_c/k_B T] \quad (6)$$

where J_0 is the collision frequency (collisions per unit cm^3 per second) that depends on the diffusion rate and the number of monomers per critical cluster.^{4,23}

At the moment critical clusters form, the concentration of monomers in solution and the temperature drop. From that point the clusters grow by addition of monomers from solution and no new clusters are formed.⁴ Reaction parameters affecting the critical values of solutions can be adjusted to eventually obtain NCs that meet requirements on size and size distribution. For small size distributions the nucleation and growth stages should be separated. First, all nuclei are formed within the same time frame, leading to very similar sizes. Then, in the growth stage, the nuclei will grow with the same rate as long as the monomer concentration is high enough. When the monomer concentration is too low Ostwald ripening will occur leading to size broadening.

Separation of nucleation and growth may be achieved with both the hot-injection method and the

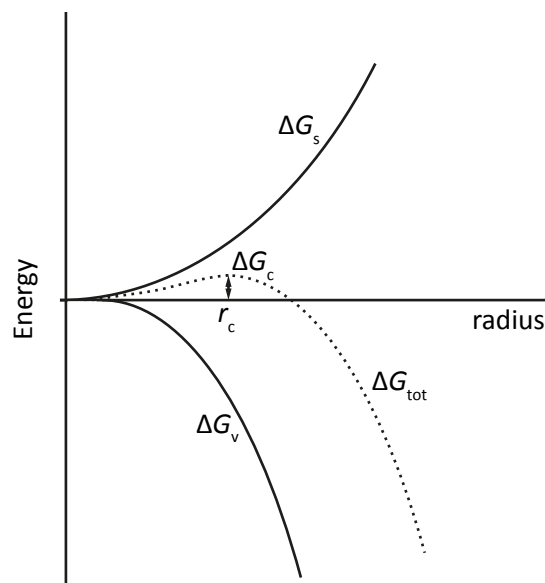


Figure 2.7. Change in free energy (ΔG_{tot}) depending on the changes in surface (ΔG_s) and a bulk volume energy (ΔG_v) and the resulting r_c . Reproduced from ref. [23]

heating-up method. In the hot-injection method, precursors are added to the heated reaction mixture separately. They immediately dissociate, which induces supersaturation. At the moment the precursors are injected, the temperature drops and the clusters grow larger at a (slightly) lower temperature.⁴ In the heating-up method all the precursors are mixed and heated up to reaction temperature. While increasing the temperature the supersaturation is increased until the energy or concentration is high enough to overcome the nucleation barrier.²⁵ An important factor is the rate of heating up, since only fast heating can induce supersaturation. For small NC sizes the supersaturation should be high, so many small clusters will form and many monomers will be consumed in the cluster formation. This way only a small amount of monomers is still available for growth. For large NC sizes the parameters should be adjusted so that only a few clusters form, that then can grow much larger with the large amount of monomers still present in solution.

2.5.2. Cation exchange

Apart from conventional direct-synthesis methods, it is also possible to prepare NCs via cation exchange. In a cation exchange reaction a cation precursor is dissolved in a dispersion with pre-synthesized NCs and small amounts of cation extracting ligands. The cations diffuse through the crystal (the original ions diffuse out and the new ions in) and the exchange takes place, whereby the original anionic sublattice usually remains intact.²⁶ The size, shape and crystal structure of the parent NC are usually preserved, thereby allowing access to materials that are not accessible via direct synthesis methods.²⁷ This diffusion mechanism in principle is very simple and intuitively understood, but the exact mechanism is not yet known. Many kinetic and thermodynamic factors, such as stability of the reactant and product phases, cation solvation and ligation, and the role of ligands and their binding energy to the different cations, play an important but not yet well understood role.^{27,28} During a cation exchange reaction, first ions at the surface of a NC are replaced after which diffusion through the crystal takes place. The exchange at the surface leads to a gradient in the NC and thereby forms a driving force for directional diffusion.²⁸ To preserve the anionic lattice the reaction zone, the atomic layers where the actual exchange takes place which exact size is dependent on the material, has to be smaller than the size of the NC.^{28,29} Depending on the driving force of the cation exchange reaction, roughly two exchange mechanisms can take place: homogeneous and heterogeneous exchange. Homogeneous exchange yields a solid solution.²⁷ The chemical interface formation energy is negative, meaning that there is no specific preferential crystal facet to nucleate, the activation barrier is low and is usually the case when cations with a higher valency are exchanged for monovalent cations.²⁸ Heterogeneous exchange takes place when the chemical interface formation energy is positive. Epitaxial nucleation will take place on the crystal facet with the lowest energy interface followed by growth of the new phase through the crystal until the whole NC is converted.^{27,28} The two phase have a sharp interface boundary, making it possible to synthesize heteronanocrystals.

2.6. Applications of colloidal semiconductor nanocrystals

2.6.1. Light emitting diodes and displays

Luminescent colloidal NCs have intrinsic properties that make them promising materials for use in light emitting diodes (LEDs) and displays (Figure 2.8). The full width at half maximum (FWHM) of their emission spectra can be as narrow as 0.25 eV, depending on the size distribution of the ensemble, which results in emission of light of a very specific color.^{30,31} Another feature of colloidal NCs is their absorption spectrum. Photons with high energies are strongly absorbed by all NCs, independent of their size, shape or composition, which makes it possible to excite many different sizes of NCs with one blue light source. This is a large advantage over organic dyes which only absorb specific wavelengths.³⁰ The down-converting properties of quantum dots makes them applicable in displays where they convert the blue backlight to red and green and thereby optimize the color balance.^{31,32} The most recent developments however, are no longer based on the optically induced emission but electrically induced emission, making flat-panel displays possible.³² In lighting devices NCs are, due to their stability and durability combined with an inexpensive and simple fabrication and processing procedure, with the above mentioned features, a promising new possibility.³³

Inside a LED the luminescent NCs are put between an electron transport layer (ETL) and a hole transport layer (HTL). These layers can be made of either organic or inorganic materials.³² A transparent conducting oxide (TCO) injects electrons in the ETL and the back contacts injects holes into the HTL (see Figure 2.9). The NCs can be excited through direct charge injection by the HTL and ETL or exciton transfer from the HTL.³⁰⁻³² In the first LED designs, the NCs were not only used as luminescent material, but also as charge transport material, which resulted in limited brightness.³² In later designs, only a very thin NC layer was used that no longer hindered charge transport.³² When the electron and hole recombine in the NC light is emitted. A challenge is to fabricate NCs with a high quantum yield that are stable under operating conditions of different devices³⁰ and to improve their electroluminescence: electrically induced emission.³¹ Improvement of quantum yields is of course desirable. This requires re-

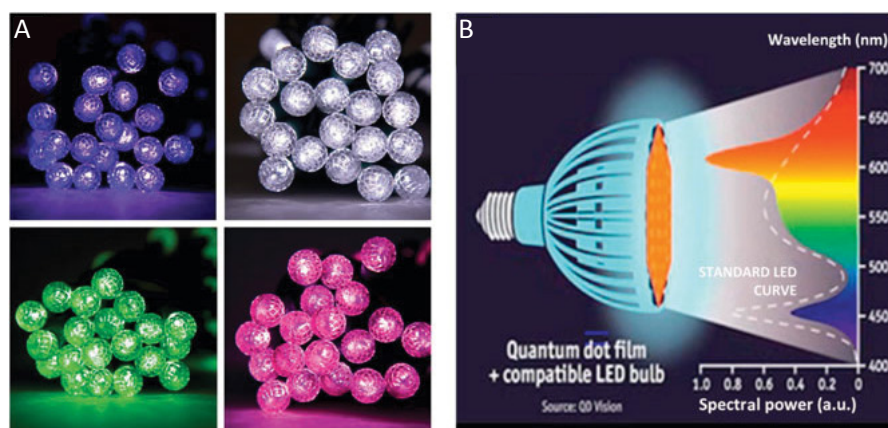


Figure 2.8. NCs in applications. A: Holiday lights introduced by Evident Technologies in 2008. A mixture of CdSe/ZnS NCs is dispersed in a polymer matrix and excited by the blue light emitting LEDs. B: Red-emitting NCs placed in front of a LED to produce 'warmer' white light. Reproduced from ref. [30]

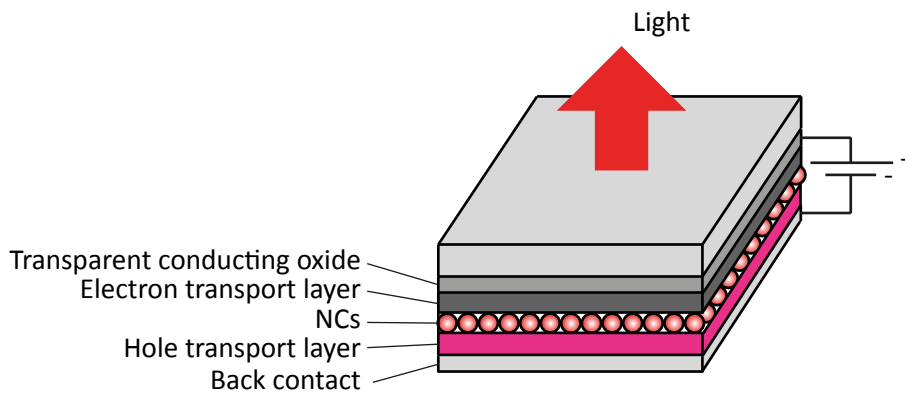


Figure 2.9. Schematic representation of a NCs containing LED, where the luminescent NCs are sandwiched between charge transporting layers. Reproduced from ref. [30]

duction of non-radiative recombination via surface defects, hot-electron trapping, exciton transfer and Auger decay.³⁴ On the latter problem first steps to a solution have been made by growing a rod shaped shell around a spherical luminescent NC core, with a gradient interface.³⁴

2.6.2. Solar cells

Semiconductor NCs can also be used in solar cells. The working mechanism of most solar cells is based on the separation of the electron and hole, which recombine when the electron has traveled through an external circuit, resulting in a current.³⁵ This can be achieved by connecting a n-type semiconductor with a p-type semiconductor. N-type materials have electrons as the main charge carriers, in p-type materials the holes are the main charge carriers. Three types of quantum dot solar cell configurations are mostly studied: the Schottky junction based quantum dot solar cells, the quantum dot sensitized solar cells and the polymer-quantum dot solar cells.^{36,37} An efficiency of 4.6% is reported for the most novel design of the Schottky cell³⁸ where NCs are close together and electrons flow to a metal contact and holes to an ohmic contact. It is important that the NCs are close together, so electron and hole transport from one NC to another is allowed. This is schematically depicted in Figure 2.10. Major issues for this design are array disorder caused by NC orientation and shape and surface states, surface structure and surface passivation. The latter issues give rise to trap states that capture charge carriers and thereby hinder their transport through the NC film. Quantum dot sensitized solar cells are very similar to dye sensitized solar cells, in which an organic dye or in this case NCs are chemisorbed on the surface of TiO₂ nanocrystals. Upon photo excitation the excited electrons are injected from the dye/NCs into the tin oxide conduction band and via other tin oxide NCs transported to an electrode. The holes are

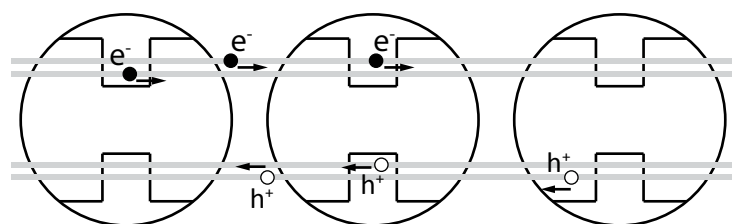


Figure 2.10. Electron and hole transport from one NC to another *via* minibands in a Schottky junction based solar cell. Reproduced from ref. [36]

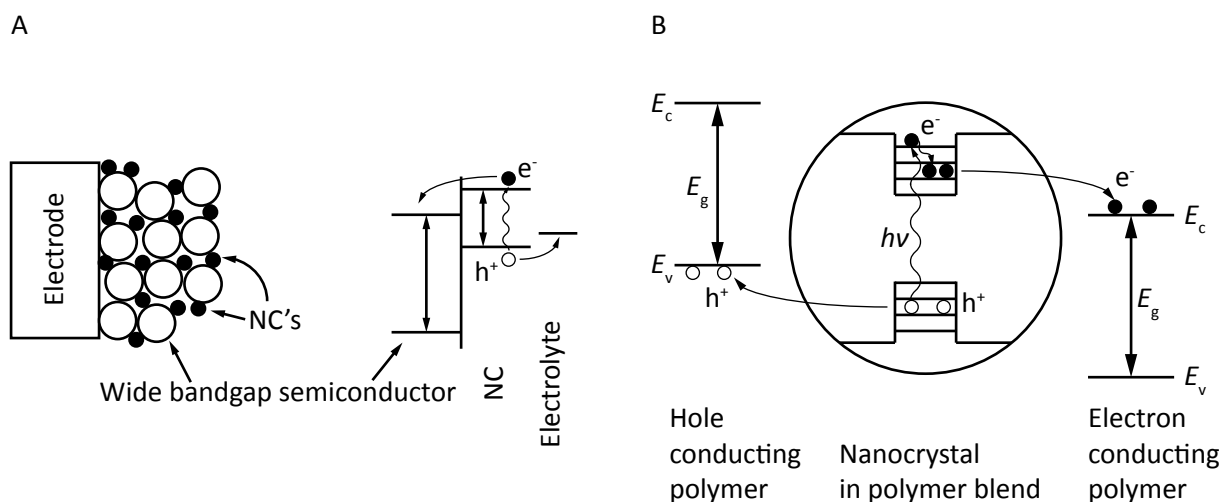


Figure 2.11. A: NCs used to sensitize a wide band gap material, such as tin oxide. Reproduced from ref. [36] B: Holes and electrons are transferred from a NC to polymers in a polymer-nanocrystal solar cell. Reproduced from ref. [36]

transported via the electrolyte to the other electrode (see Figure 2.11A).^{36,37} NCs have advantages over dyes, because their band gap is better tunable, absorption is stronger and over a broader energy range and they are more stable upon prolonged irradiation and in water and oxygen rich environments.³⁷ In the polymer-quantum dot solar cell the NCs are dispersed in a polymer layer, consisting of two types of polymers: molecules that transport holes and others that transport electrons, or just one polymer that transports holes (see Figure 2.11B). In the last case electrons are transported by the NCs. A critical factor in this type of solar cells is to prevent recombination of electrons and holes at polymer interfaces and the role of ligands is still unclear.^{36,37}

2.6.3. Luminescent solar concentrators

Luminescent solar concentrators (LSCs) are devices that can enhance solar cell efficiencies. Incident light is absorbed by a luminescent material (for example luminescent NCs) dispersed in a thin plastic sheet. The emitted light is transported through the sheet by total internal reflection to the solar cell (Figure 2.12).³⁹ The surface of the relatively cheap plastic sheet is much larger than the surface of the expensive solar cell which results in a large cost reduction.^{39,40} Several loss mechanisms reduce the efficiencies of the LSC: partial surface reflection by the plastic sheet, parasitic absorption by the plastic sheet itself, non-radiative decay of the luminescent material, escape of the light due to non-perfect total internal reflection and re-absorption of the emitted light by other NCs so that all loss mechanisms

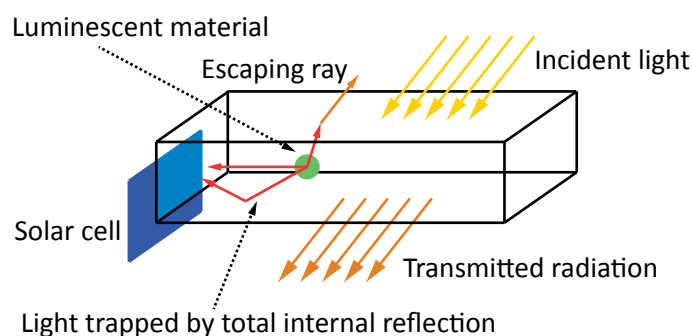


Figure 2.12. Schematic representation of the working principle of a luminescent solar concentrator. Reproduced from ref. [39]

can take place again.³⁹ To prevent re-absorption the overlap of the absorption and emission bands of the luminescent material, the self-absorption cross-section, should be as small as possible. This can be achieved in HNCs with a type II band alignment^{39,40} or by NC doping with transition-metals.⁴⁰

2.6.4. Bio-labeling

Bio-labeling is the labeling of biological molecules with a luminescent material, for example colloidal NCs. NCs are very promising for this application because, as stated earlier in this section, the FWHM of their emission can be narrow, the exact emission energy can be tuned and they can be excited within a broad wavelength range. It is therefore possible to label different molecules (within a cell for example) with different colors and image them simultaneously.⁴¹ Before NCs can be used in biological environments they have to be made water soluble without losing their luminescent properties and preferably have an engineered outer layer that specifically binds to the target. For *in vivo* imaging (Figure 2.12A, labeling in living organisms) an emission between 650 and 900 nm is required, to prevent absorption and emission by other molecules present in the organism.⁴² Despite the broad absorption range, excitation of the NCs is difficult, because the penetration depth of blue light in tissue is short.⁴² Strategies to circumvent this problem are fluorescence resonant energy transfer (FRET), bioluminescence resonant energy transfer (BRET) and chemiluminescence resonant energy transfer (CRET)⁴³ or the use of energies in the near infrared (NIR) spectral region.⁴⁴

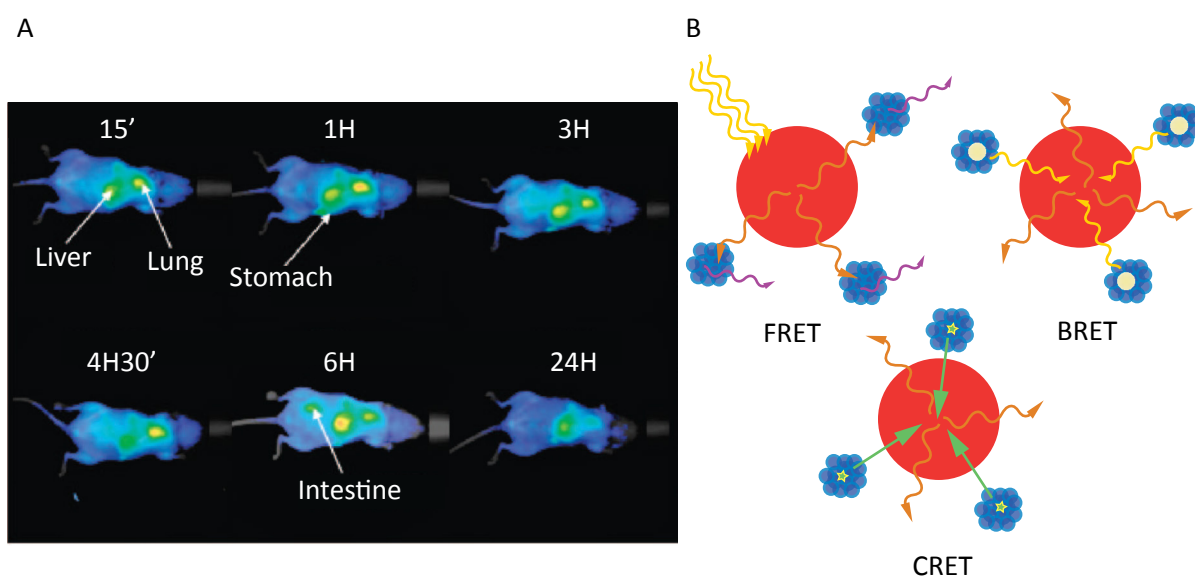


Figure 2.13. A: *In vivo* imaging in a mouse using luminescent CIS/ZnS NCs. Reproduced from ref. [42]. B: Schematic representation of fluorescence resonant energy transfer (FRET), bioluminescence resonant energy transfer (BRET) and chemiluminescence resonant energy transfer (CRET). Reproduced from ref. [43]

2.7. References

1. Steigerwald, M. L. & Brus, L. E. Semiconductor Crystallites: A Class of Large Molecules. *Acc. Chem. Res.* **23**, 183–188 (1990).
2. Koole, R., Groeneveld, E., Vanmaekelbergh, D., Meijerink, A. & de Mello Donega, C. in *Nanoparticles: Workhorses of Nanoscience* (Springer-Verlag, 2015).
3. Alivisatos, A. P. Perspectives on the Physical Chemistry of Semiconductor Nanocrystals. *J. Phys. Chem.* **100**, 13226–13239 (1996).
4. De Mello Donegá, C. Synthesis and properties of colloidal heteronanocrystals. *Chem. Soc. Rev.* **40**, 1512–46 (2011).
5. Kolny-Olesiak, J. & Weller, H. Synthesis and application of colloidal CuInS₂ semiconductor nanocrystals. *ACS Appl. Mater. Interfaces* **5**, 12221–37 (2013).
6. De Mello Donegá, C. & Koole, R. Size Dependence of the Spontaneous Emission Rate and Absorption Cross Section of CdSe and CdTe Quantum Dots. *J. Phys. Chem. C* **113**, 6511–6520 (2009).
7. Kumar, P. et al. Nanotwinning and structural phase transition in CdS quantum dots. *Nanoscale Res. Lett.* **7**, 584 (2012).
8. Brus, L. Quantum Crystallites and Nonlinear Optics. *Appl. Phys. A* **53**, 465–474 (1991).
9. Ithurria, S. et al. Colloidal nanoplatelets with two-dimensional electronic structure. *Nat. Mater.* **10**, 936–41 (2011).
10. Ueng, H. Y. & Hwang, H. . The defect structure of CuInS₂. Part I: intrinsic defects. *J. Phys. Chem. Solids* **50**, 1297–1305 (1989).
11. Hamanaka, Y. et al. Defect-induced photoluminescence and third-order nonlinear optical response of chemically synthesized chalcopyrite CuInS₂ nanoparticles. *Chem. Phys. Lett.* **466**, 176–180 (2008).
12. She, C., Bryant, G. W., Demortière, A., Shevchenko, E. V. & Pelton, M. Controlling the spatial location of photoexcited electrons in semiconductor CdSe/CdS core/shell nanorods. *Phys. Rev. B* **87**, 155427 (2013).
13. De Mello Donegá, C. Formation of nanoscale spatially indirect excitons: Evolution of the type-II optical character of CdTe/CdSe heteronanocrystals. *Phys. Rev. B* **81**, 165303 (2010).
14. Strehlow, W. H. & Cook, E. L. Compilation of Energy Band Gaps in Elemental and Binary Compound Semiconductors and Insulators. *J. Phys. Chem. Ref. Data* **2**, 163–199 (1973).
15. Hunger, R., Pettenkofer, C. & Scheer, R. Dipole formation and band alignment at the Si(111)/CuInS₂ heterojunction. *J. Appl. Phys.* **91**, 6560 (2002).
16. Van de Walle, C. G. & Neugebauer, J. Universal alignment of hydrogen levels in semiconductors, insulators and solutions. *Nature* **423**, 626–8 (2003).
17. Roduner, E. Size matters: why nanomaterials are different. *Chem. Soc. Rev.* **35**, 583–92 (2006).
18. Weiss, E. A. Organic Molecules as Tools To Control the Growth, Surface Structure, and Redox Activity of Colloidal Quantum Dots. *Acc. Chem. Res.* **46**, 2607–2615 (2013).
19. Mulder, W. J. M. et al. Quantum dots with a paramagnetic coating as a bimodal molecular imaging probe. *Nano Lett.* **6**, 1–6 (2006).

20. Nie, Z., Petukhova, A. & Kumacheva, E. Properties and emerging applications of self-assembled structures made from inorganic nanoparticles. *Nat. Nanotechnol.* **5**, 15–25 (2010).
21. Kovalenko, M. V, Scheele, M. & Talapin, D. V. Colloidal nanocrystals with molecular metal chalcogenide surface ligands. *Science* **324**, 1417–20 (2009).
22. Everett, D. H. in *Basic Principles of Colloid Science* 54–62 (The Royal Society of Chemistry, 1988).
23. Roduner, E. in *Nanoscopic Materials. Size Dependend Phenoma*. 119–161 (The Royal Society of Chemistry, 2006).
24. Chorckenforff, I. & Niemantsverdriet, J. W. *Concepts of Modern Catalysis and Kinetics*. 23–73 (Wiley, 2006).
25. Kwon, S. G. et al. Kinetics of monodisperse iron oxide nanocrystal formation by “heating-up” process. *J. Am. Chem. Soc.* **129**, 12571–84 (2007).
26. Jain, P. K., Amirav, L., Aloni, S. & Alivisatos, A. P. Nanoheterostructure cation exchange: anionic framework conservation. *J. Am. Chem. Soc.* **132**, 9997–9999 (2010).
27. Rivest, J. B. & Jain, P. K. Cation exchange on the nanoscale: an emerging technique for new material synthesis, device fabrication, and chemical sensing. *Chem. Soc. Rev.* **42**, 89–96 (2013).
28. Beberwyck, B. J., Surendranath, Y. & Alivisatos, a. P. Cation Exchange: A Versatile Tool for Nanomaterials Synthesis. *J. Phys. Chem. C* **117**, 19759–19770 (2013).
29. Son, D. H., Hughes, S. M., Yin, Y. & Paul Alivisatos, a. Cation exchange reactions in ionic nanocrystals. *Science* **306**, 1009–12 (2004).
30. Talapin, D. V. & Steckel, J. Quantum dot light-emitting devices. *MRS Bull.* **38**, 685–691 (2013).
31. Supran, G. J. et al. QLEDs for displays and solid-state lighting. *MRS Bull.* **38**, 703–711 (2013).
32. Shirasaki, Y., Supran, G. J., Bawendi, M. G. & Bulović, V. Emergence of colloidal quantum-dot light-emitting technologies. *Nat. Photonics* **7**, 933–933 (2013).
33. Bae, W. K., Brovelli, S. & Klimov, V. I. Spectroscopic insights into the performance of quantum dot light-emitting diodes. *MRS Bull.* **38**, 721–730 (2013).
34. Rabouw, F. T. et al. Reduced Auger recombination in single CdSe/CdS nanorods by one-dimensional electron delocalization. *Nano Lett.* **13**, 4884–92 (2013).
35. Nelson, J. in *Physics of Solar Cells* 1–16 (Imperial College Press, 2013).
36. Nozik, A. J. Quantum dot solar cells. *Phys. E Low-dimensional Syst. Nanostructures* **14**, 115–120 (2002).
37. Albero, J., Clifford, J. N. & Palomares, E. Quantum dot based molecular solar cells. *Coord. Chem. Rev.* **263-264**, 53–64 (2014).
38. Ma, W. et al. Photovoltaic performance of ultrasmall PbSe quantum dots. *ACS Nano* **5**, 8140–7 (2011).
39. Krumer, Z. et al. Tackling self-absorption in luminescent solar concentrators with type-II colloidal quantum dots. *Sol. Energy Mater. Sol. Cells* **111**, 57–65 (2013).
40. Meinardi, F. et al. Large-area luminescent solar concentrators based on “Stokes-shift-engineered” nanocrystals in a mass-polymerized PMMA matrix. *Nat. Photonics* (2014). doi:10.1038/nphoton.2014.54

41. Bruchez Jr., M., Moronne, M., Gin, P., Weiss, S. & Alivisatos, A. P. Semiconductor Nanocrystals as Fluorescent Biological Labels. *Science* **281**, 2013–2016 (1998).
42. Li, L. et al. Highly Luminescent CuInS₂/ZnS Core/Shell Nanocrystals: Cadmium-Free Quantum Dots for In Vivo Imaging. *Chem. Mater.* **21**, 2422–2429 (2009).
43. Frasco, M. F. & Chaniotakis, N. Bioconjugated quantum dots as fluorescent probes for bioanalytical applications. *Anal. Bioanal. Chem.* **396**, 229–40 (2010).
44. Zhao, Y. Quantum Dots and Doped Nanocrystals: Synthesis, Optical Properties and Bio-applications. 21–23 (2013).

3. Synthesis and optical properties of luminescent colloidal copper indium sulfide nanocrystals

3.1. Introduction

Copper indium sulfide (CIS) nanocrystals (NCs) are made of non-toxic elements, in contrast to the common used semiconductor NCs containing cadmium or lead, which makes them interesting for use in several applications. In general, tunable optical properties, high efficiencies and a narrow full width at half maximum (FWHM) are required for use in applications as light emitting diodes (LEDs), solar cells, biolabeling and luminescent solar concentrators (LSCs). Colloidal CIS NCs meet many of these requirements, however the FWHM is still an issue. Research into the nature of the emitting state of CIS NCs, should provide more insight into the possible improvements of this property. For use in LSCs, the large Stokes shift that is observed for CIS NCs¹ is ideal.

In this chapter an easy direct-synthesis method is described to obtain colloidal luminescent copper indium sulfide NCs. The size of the NCs and thereby emission wavelength, can be tuned by small variations in synthesis conditions. Little is known about the nature of the luminescence of CIS NCs. The results presented here provide a first step towards understanding the electronic structure and the optical properties of these NCs.

3.2. Experimental

3.2.1. Chemicals

Copper (I) iodide (Sigma Aldrich, 98%), Indium (III) acetate (Sigma Aldrich, 99.99%), 1-dodecanethiol (DDT, Sigma Aldrich, ≥98%), Oleic acid (OA, Sigma Aldrich, 90%), Toluene (Sigma Aldrich, 99.8%), Methanol (Sigma Aldrich, 99.8%), 1-Butanol (Sigma Aldrich, 99.8%), Ethanol (Sigma Aldrich, ≥99.8%).

3.2.2. Synthesis

The synthesis procedure is based on the earlier reported protocol by Lu *et al.*² In a typical synthesis CuI (0.4 mmol), In(Ac)₃ (0.4 mmol) and 5 mL DDT were mixed under inert atmosphere and degassed for 1 hour at 80 °C. Then the temperature was raised to 230 °C under N₂ flow and after 11 minutes reaction cooled to room temperature. The NCs were washed with ethanol or a methanol/butanol mixture and dispersed in toluene. Reaction time and temperature, precursor ratio, atmosphere and ligands were varied to study their influence. An overview of the exact reaction conditions per sample is given in

3.2.3. Characterization

Absorption spectra were recorded with a Perkin Elmer Lambda 950 UV/VIS/NIR spectrophotometer. Luminescence measurements were performed with an Edinburgh Instruments FLS920 spectrofluorimeter equipped with a 450 W Xe lamp and double excitation monochromator with a grating blazed at 300 nm. The signal was detected with a Hamamatsu R928 PMT detector with a grating blazed at 500 nm or, when the emission was at 800 nm or longer wavelengths, with an Acton research SpectraPro 300i CCD camera with optical fiber. For lifetime and time-resolved emission map measurements excitation was carried out with an Edinburgh Instruments EPL445 picosecond pulsed diode laser at 441.1 nm and a pulse width of 80.2 ps. The signal was detected with a Hamamatsu photosensor module H10720-01. Lifetimes were obtained from a bi-exponential fit of the decay curve. Transmission electron microscopy (TEM) images were taken with a Philips Tecnai microscope (FEI company), with an accelerating voltage of 100 or 120 kV. Energy dispersive X-ray spectroscopy (EDS) measurements were performed with a FEI Tecnai-20F microscope equipped with a Field Emission Gun, a Gatan 694 CCD camera and an EDA spectrometer. The microscope was operated at 200 kV. Acquisition time for the EDS measurements was 45 s. Large areas (containing approximately 10^4 - 10^5 NCs) were measured to obtain representative data.

3.3. Results & discussion

3.3.1. Reaction steps

In the sections that follow, the influence of variations in reaction conditions on the resulting nanocrystal size are discussed. In this discussion, the formation mechanism of colloidal CIS NCs is assumed to consist of the following reaction steps. First, copper sulfide monomers will form, then indium monomers are incorporated, either by diffusion of indium into the copper sulfide clusters or by fusing of copper sulfide and indium sulfide monomers. Then these CIS clusters grow to NCs. Monomer formation and diffusion and their actual reaction are the processes that determine the final rate of the CIS NC formation.

3.3.2. Tuning of optical properties

A. Variation in reaction time and temperature

The influence of reaction time and temperature on the resulting NCs was investigated by synthesizing NCs at 230 °C and 210 °C for various reaction times. TEM pictures of small (2-4 nm) CIS NCs are very unclear due to resolution of the instrument used and are therefore not suitable for reliable size determination (see Appendix B for a few examples). Therefore, the emission wavelength of the CIS nanocrystals was used as a measure for their size, since larger NCs have a smaller band gap and thus emit at longer wavelengths than smaller NCs. The absorption and emission spectra of the NCs are

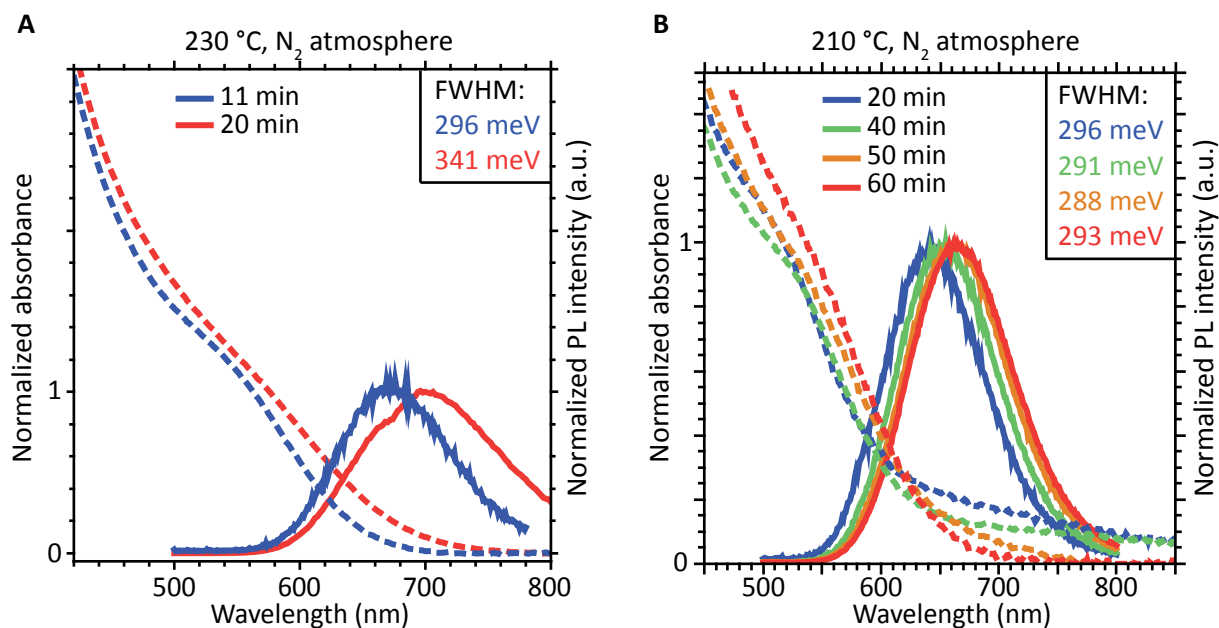


Figure 3.1. A: Absorption (dashed lines) and emission (solid lines) of CIS NCs synthesized at 230 °C for 11 (blue) and 20 (red) minutes. B: Absorption (dashed lines) and emission (solid lines) of CIS NCs synthesized at 210 °C for 20–60 minutes. For both syntheses a longer reaction time results in larger NCs and thus a red shift in the absorption and emission spectra.

shown in Figure 3.1A and B. The red shift in emission and absorption clearly shows that longer reaction times and/or higher reaction temperatures lead to larger NCs, which is consistent with earlier reports on CIS NCs.³ After 10 minutes reaction at the lower temperature (210 °C) no NCs were formed yet, after 40–50 minutes reaction at 210 °C (emission peak at 662–666 nm) the NC size is comparable to 11 minutes reaction at the higher temperature of 230 °C (emission peak at 672 nm). According to classical nucleation theory, it is remarkable that at lower temperatures the nanocrystals are smaller. A lower supersaturation is expected, leading to the formation of fewer critical clusters that can grow larger with many monomers still in solution. Apparently the difference in temperature does not lead to a significant change in supersaturation of the solution and the NC size is only determined by the growth temperature. This indicates that the formation of critical clusters is not the rate limiting step in this process but the formation of monomers or the diffusion of the monomers to the clusters is. The FWHM of the emission peak of the NCs synthesized at 230 °C for 20 minutes is much larger than for the other NCs, suggesting that Ostwald ripening or undefined nucleation and growth has taken place.

B. Variation in reaction atmosphere

The influence of the reaction atmosphere was investigated by synthesizing CIS NCs under N₂ atmosphere and under atmospheric conditions, at 230 °C for 11 minutes. When both emission peaks are compared (Figure 3.2A) it is remarkable that the NCs synthesized under air have a much better signal to noise ratio and are apparently unaffected by the presence of oxygen. In contrast, NCs synthesized under air degrade rapidly under air after purification, as shown in Figure 3.2B. After 2 hours the intensity decreases by 6% and after 3 hours by 18% relative to the initial intensity. After 24 hours the emission is completely quenched. These results clearly show that the oxidation of the surface of the NCs results in an increase of surface defect states, leading to domination of the decay by non-radiative relaxation

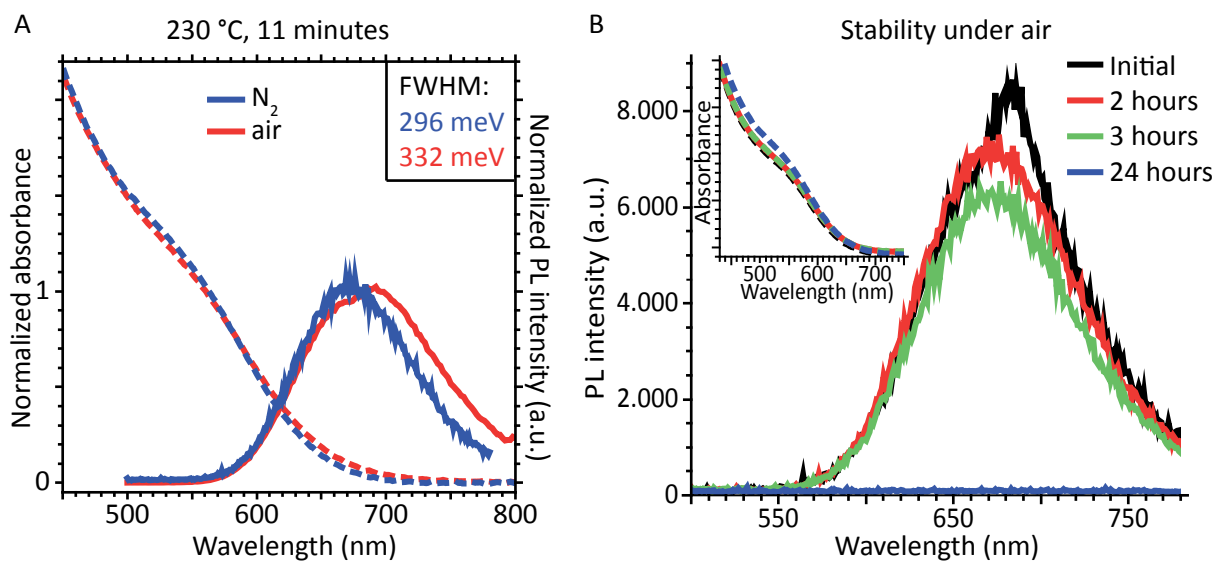


Figure 3.2. A: Absorption (dashed lines) and emission (solid lines) spectra of CIS NCs synthesized under N_2 atmosphere (blue) and air (red). The NCs synthesized under air have a much better signal-to-noise ratio than the NCs synthesized under N_2 . There is no shift of the spectra observed. B: Stability of the photoluminescence of CIS NCs synthesized under N_2 when exposed to air. After 24 hours under air the emission is completely quenched.

via these states

C. Variation in precursor ratio

To study the influence of the copper to indium ratio on CIS NC size and optical properties, the Cu:In ratio was varied over several synthesis, under N_2 for 11 minutes at 230 °C. EDS measurements (Figure 3.3, Table 3.1) indicate that the copper:indium ratio used during the synthesis is directive for the resulting copper:indium ratio in the NCs. The EDS results also suggest that at least the same amount of indium as copper should be present in the NC (Cu:In ratio at maximum 1:1) to observe luminescence, since the sample with a 1.5:1 ratio did not luminesce. In Figure 3.4B the absorption spectrum of the Cu:In 2:1 sample is shown and the characteristic absorption peak for CIS around 550 nm is not visible. These observations show that, instead, $Cu_{2-x}S$ NCs were formed in this synthesis. This differs from earlier reported results, in which luminescent CIS NCs with a Cu:In ratio of 1.5:1 were observed.⁴ The large amount of sulfur detected in region 3 of the Cu:In 2:1 sample and the high iodide peaks in the spectrum are most probably due to an artifact in the device, since it has shown a sudden higher sensitivity to anions before. The other two regions for this $Cu_{2-x}S$ sample show a clear copper-rich result, with stoichiometries that differ between the regions. These differing ratios within the ensemble are probably caused by vacancies in the $Cu_{2-x}S$ NCs, a well-known property for $Cu_{2-x}S$ materials, in which numerous stoichiometric changes can occur. In Figure 3.4A a blue shift compared to the stoichiometric CIS NCs is observed in absorption and emission for the indium rich NCs (Cu:In 1:2 and 1:4). This has been reported earlier and explained as a band gap widening due to the lowering of the energy level of the valence band (composed of Cu 3d and S 3p orbitals) induced by copper deficiencies.^{5,6} According to this explanation the wavelength shifting is not due to differences in NC size. It is unclear why the emission of the sample with Cu:In 1:4 precursor ratio is not shifted further to the blue, since the Cu:In ratio in the reaction mixture was even lower than 1:2, however since the resulting dispersion was very viscous and

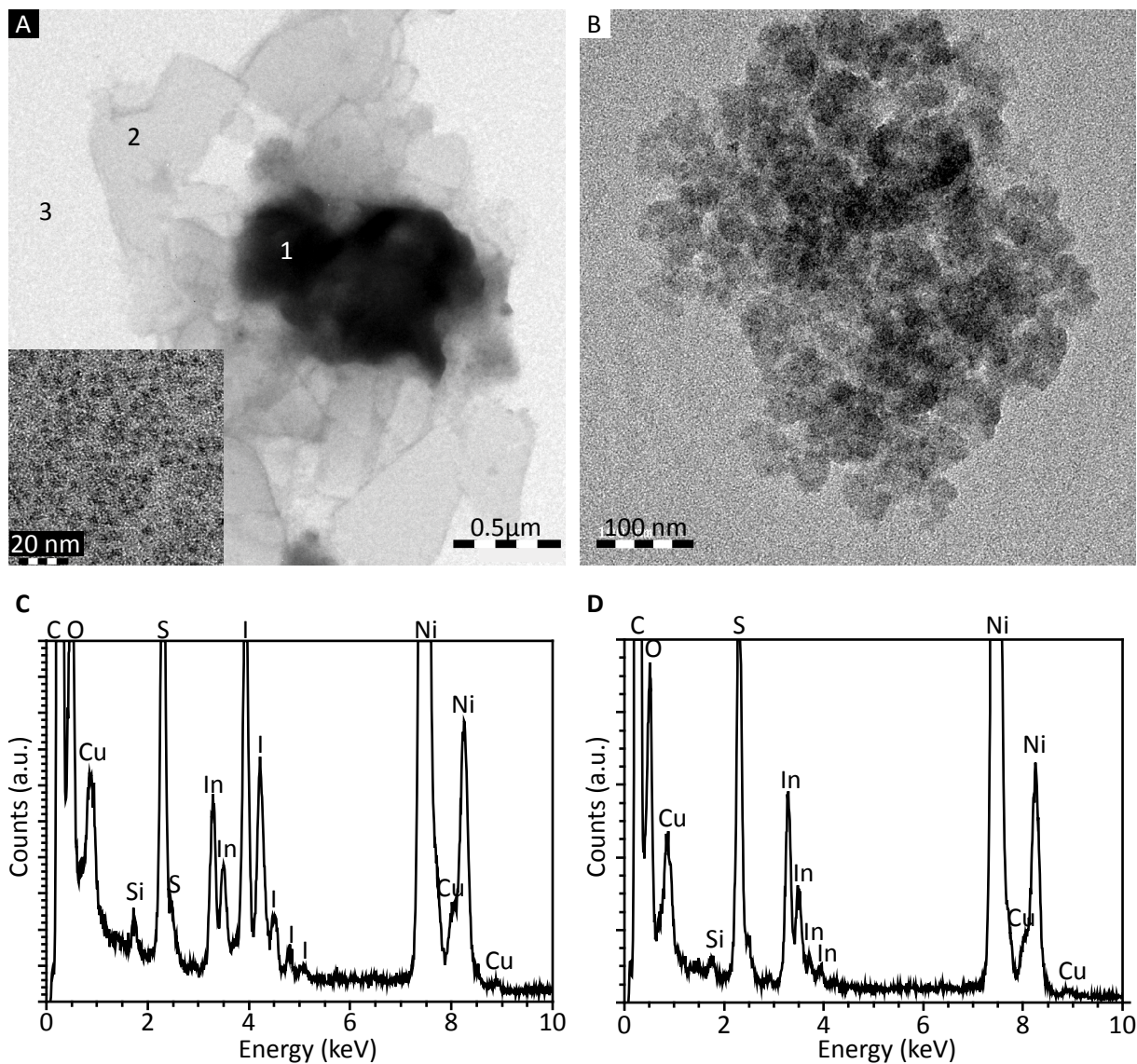


Figure 3.3. A: Three positions on the TEM grid with different looking material where EDS measurements were performed in the sample with Cu:In precursor ratio of 2:1. Inset: zoom in on region 3. B: Location of EDS measurement on sample with Cu:In precursor ratio 1:2. C: EDS spectrum of region 3 of the Cu:In 2:1 sample shown in A. D: EDS spectrum of Cu:In 1:2 sample shown in B.

Table 3.1. Elemental ratio of NCs synthesized with a Cu:In 2:1 precursor ratio (left columns) and with a 1:2 Cu:In precursor ratio (right columns). The numbers between brackets refer to the regions shown in Figure 3.3.

	Cu:In 2:1 (1)	Cu:In 2:1 (2)	Cu:In 2:1 (3)	Cu:In 1:2 (1)	Cu:In 1:2 (2)
	atomic%	atomic%	atomic%	atomic%	atomic%
S	48.981	62.387	70.069	67.179	63.527
Cu	31.618	26.01	12.52	9.664	10.219
In	19.399	11.602	17.41	23.156	26.253
S:In	2.5	5.4	4.0	7.0	6.2
Cu:In	1.6	2.2	0.7	1	1
In	1	1	1	2.4	2.6
	$\text{Cu}_{1.6}\text{In}_1\text{S}_{2.5}$	$\text{Cu}_{2.2}\text{In}_1\text{S}_{5.4}$	$\text{Cu}_{0.7}\text{In}_1\text{S}_4$	$\text{Cu}_1\text{In}_{2.4}\text{S}_7$	$\text{Cu}_1\text{In}_{2.6}\text{S}_{6.2}$

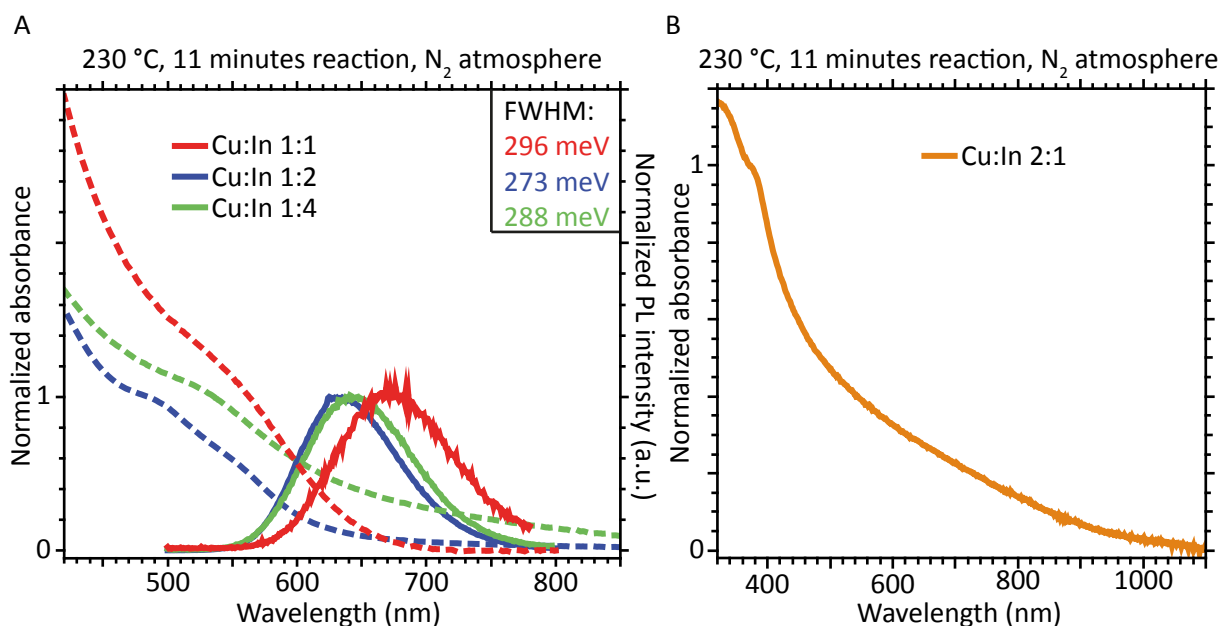


Figure 3.4. A: Absorption (dashed lines) and emission (solid lines) spectra of samples synthesized with different Cu:In precursor ratios. A blue shift in both emission and absorption is observed for the In-rich NCs, indicating a shift of the valence band edge to lower energies. B: Absorption spectrum of sample synthesized with Cu:In 2:1 precursor ratio. The sample did not luminesce and is expected to be Cu_{2-x}S .

the absorption spectrum is very broad (see Figure 3.4A) the Cu:In ratio may have been too low resulting in a side reaction forming a gelly substance or the limit of the possible CIS stoichiometries was reached.

The influence of reaction atmosphere and reaction temperature on the synthesis with a Cu:In ratio of 1:2 was studied as well. NCs were synthesized under N_2 atmosphere at a temperature of 230 °C for 11 minutes and a temperature of 210 °C for 15 minutes. One synthesis was performed under air, at a temperature of 230 °C for 11 minutes. The absorption and emission spectra of the NCs obtained are shown in Figure 3.5. It is clear that the position of the peaks does not shift when the reaction atmosphere is changed, however, for the NCs synthesized at 210 °C under N_2 flow the absorption spectrum shows a

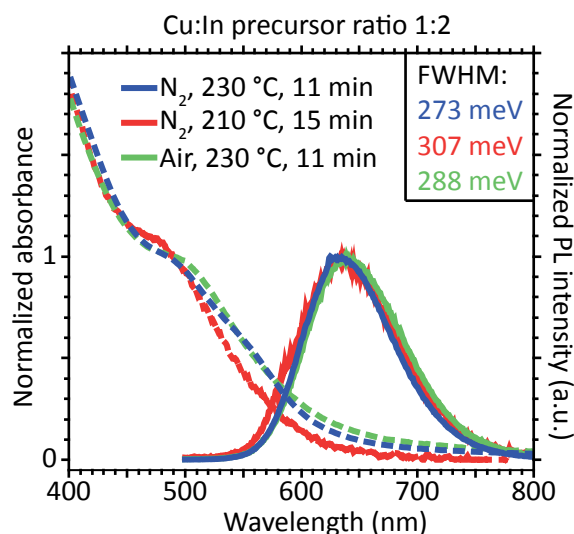


Figure 3.5. Absorption (dashed lines) and emission (solid lines) of In-rich NCs synthesized at different temperatures and under different atmosphere. In contrast to the Cu:In 1:1 syntheses the changes in reaction conditions have no influence on the NC size and thereby absorption and emission wavelength.

sharper peak. This is a different result than obtained for the regular Cu:In 1:1 NCs, where the reaction temperature had a large influence on the resulting NCs size (see Figure 3.1). This result indicates that when indium is present in excess (more than one equivalent copper), the rate limiting step in the reaction is no longer the formation of monomers, but the chemical reaction to form NCs. It also shows that the monomer formation limitation that was observed for the Cu:In 1:1 case (see section A on page 22) was, more specific, the formation of the indium monomers.

3.3.3. Exciton lifetimes

The decay curves of regular CIS NCs (Cu:In 1:1, synthesized for 40 min at 210 °C) and indium rich CIS NCs (Cu:In 1:2, synthesized for 11 min at 230 °C) were measured to obtain more information on the origin of their emission. The results were analyzed using the model discussed in chapter 2, where the total decay rate (w_{tot}) depends on the radiative decay rate (w_{rad}) and the non-radiative decay rate ($w_{\text{non-rad}}$) and the exciton lifetime (τ) is inversely proportional to the total decay rate.

Lifetimes at different positions within the emission peaks of the CIS and In-rich CIS samples were obtained with a bi-exponential fit and the results are summarized in Table 3.2 and Figure 3.6. For the indium rich sample a fourth wavelength was measured to obtain a dataset comparable with the stoichiometric CIS NCs. The general trend that the lifetimes are longer on the red side of the peak, is explained by the composition of the ensemble, which always consists of some nanocrystals that are smaller and some larger nanocrystals. In the smaller NCs the band gap is larger, which means that they emit light in the blue. Because they are smaller, the exciton is more confined and the wavefunctions of the electron and hole strongly overlap, resulting in faster radiative decay. The reasoning for the larger NCs is the other way around. They emit in the red due to their smaller band gap and because the exciton is less confined and the wavefunction overlap of the electron and hole is smaller, the radiative decay is slower. This size dependence of the decay rate was earlier observed for CdSe and CdTe NCs.⁷

The lifetimes of the excited states of the indium rich NCs are much longer, for both the fast component (τ_1) and the slow component (τ_2) which is in agreement with previous results.⁸ The longer lifetimes are clearly recognizable in both Figure 3.6C and D where the decay curves recorded at different wavelengths within the emission peak of the In-rich nanocrystals (C) decay less steeply than for the stoichiometric CIS NCs (D). When following the reasoning above, stating that $w_{\text{non-rad}}$ is faster than w_{rad} , the longer lifetimes for the In-rich NCs indicate an increase in radiative recombination (and thus decrease of non-radiative recombination) in comparison with the stoichiometric CIS NCs. This explanation makes use of the model depicted in Figure 2.5A and B, where trap energy levels facilitate non-radiative decay and radiative decay is band-edge recombination. If this model is correct, it would mean that the luminescence efficiency is increased, when the exciton lifetime becomes longer. When comparing both emission peaks (Figure 3.6A and B) the emission peak of the In-rich NCs shows a higher signal to noise ratio which is indeed an indication that the luminescence efficiency of the indium rich NCs is higher.

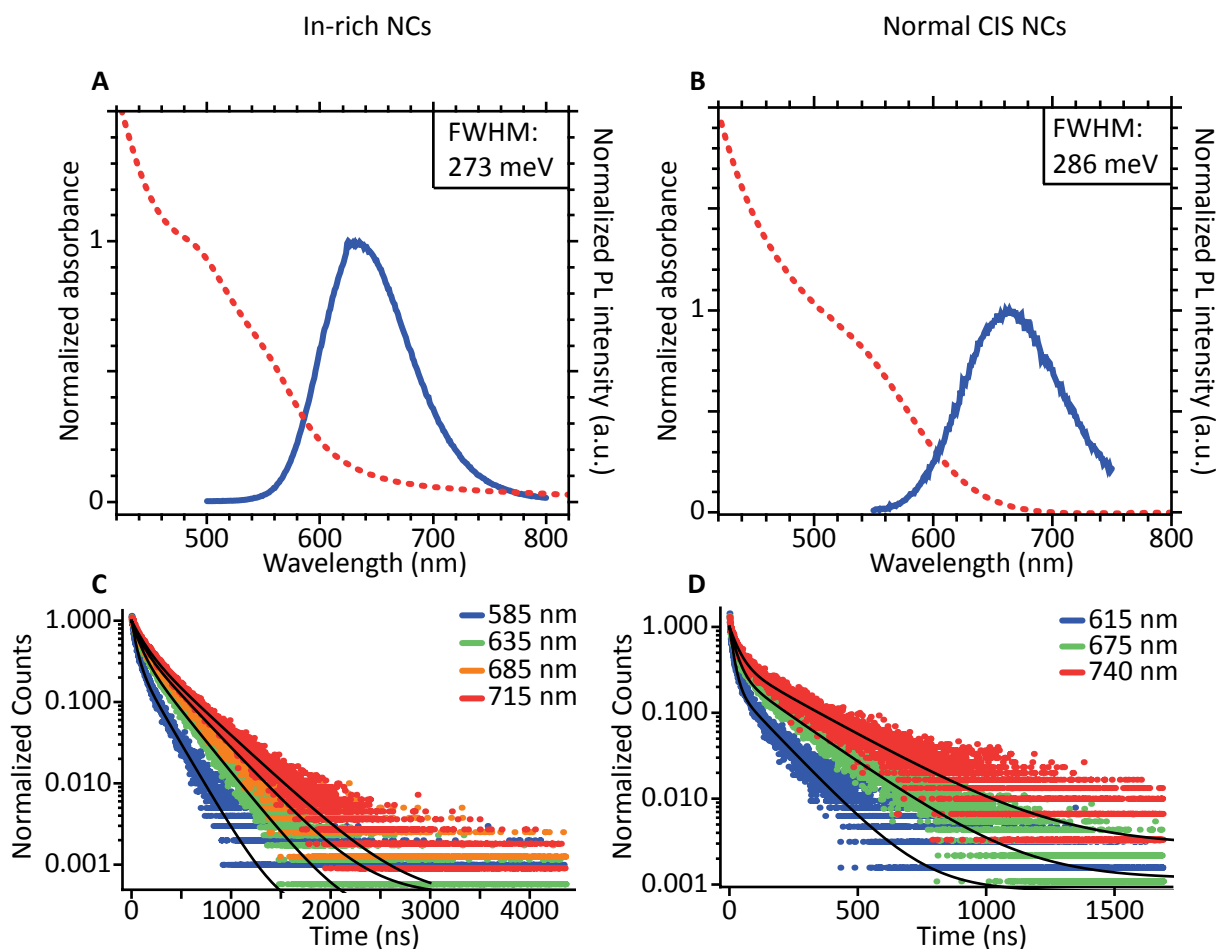


Figure 3.6. A and B: Absorption (dashed red line) and emission (solid blue line) spectra of In-rich and stoichiometric CIS NCs. The signal-to-noise ratio of the In-rich sample is better, suggesting a decrease in non-radiative recombination. C and D: Decay curves and bi-exponential fits at different wavelengths within the emission peaks of the In-rich and stoichiometric sample. The exciton lifetimes in the In-rich sample are much longer than in the stoichiometric sample.

These results suggest an important role of indium (or copper deficiency) as origin of the luminescence of CIS nanocrystals.

Ueng *et al.*⁹ reported in 1989 that the luminescence of bulk CIS crystals might be due to intrinsic crystal defects. Sulfur vacancies, interstitial indium atoms and indium at copper vacancies are donor levels, while copper vacancies form acceptor levels (see Figure 3.7). This model leads to the conclusion that bulk CIS is a n-type material and the emission originates from donor-acceptor recombination. An

Table 3.2. Exciton Lifetimes of stoichiometric CIS NCs and In-rich CIS NCs, obtained at different wavelengths within the emission peaks and with a bi-exponential fit.

Sample	Wavelength	Wavelength	Wavelength	Wavelength
Lifetime	(nm)	(nm)	(nm)	(nm)
Normal CIS		615	675	740
τ_1 (ns)		16	26	34
τ_2 (ns)		137	206	257
In-rich CIS	585	635	685	715
τ_1 (ns)	45	77	86	111
τ_2 (ns)	207	285	335	384

even more extended band diagram was proposed by Lewerenz *et al.*¹⁰ in 1993, where two extra defect states in the very middle of the band gap are positioned. Binsma *et al.*¹¹ report the possibility of n-type as well as p-type bulk copper indium sulfide and two possible types of direct band gap emission in indium-rich samples, besides various defect channels. The increase of radiative decay rates with more indium present in the nanocrystal agrees with the model proposed by Ueng *et al.* since when more donor levels are present in a n-type material the luminescence is enhanced. On the other hand, In-rich can also be regarded as Cu-poor. Less copper means more copper-vacancies, leading to self-compensation when the emission originates from band edge recombination and this vacancy acts as an electron acceptor.⁹ When the emission originates from donor-acceptor recombination, this self-compensation is in fact the desired process. The essential question is how the addition of extra donor levels (due to extra indium) and the addition of extra acceptor levels (due to less copper) balance each other in the nanocrystal. At this point, with the results obtained so far, it is not possible to be conclusive on this matter.

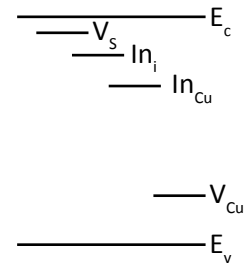


Figure 3.7. Proposed energy levels of CuInS_2 according to Ueng *et al.*⁹ Reproduced from ref. [9]

In Figure 3.8A and B the total decay curves of the In-rich and the normal CIS NCs are fitted bi-exponentially. In C (for the In-rich NCs) and D (for the normal NCs) the lifetime of the fast components are plotted as function of energy. A shorter exciton lifetime is observed at higher energies, which is expected for smaller NCs: the exciton is more confined and the wave functions of the electron and hole overlap stronger than for larger NCs. Earlier studies⁷ show a linear dependence of the decay rate and emission energy for CdSe and CdTe NCs and the same behavior is observed here, for CIS NCs.

This linear dependence of decay rate and emission energy was earlier observed by Hamanaka *et al.*⁴ who argues that donor-acceptor transitions cannot be the origin of this phenomenon, since the Stokes shift is too large (550 meV in his study, 450-618 meV measured for the samples in this chapter) compared to the positions of the defect states and the emission peak does not shift when excited at different energies. Only the states postulated by Lewerenz *et al.*¹⁰ to be in the very middle of the gap would give rise to Stokes shifts of this magnitude, but in the same paper he proposed only non-radiative relaxation *via* these states. Hamanaka therefore suggests the 'trap hopping' mechanism as origin for the luminescence in CIS NCs and explanation of the large Stokes shift observed.⁴ In the trap hopping mechanism charge carriers recombine after stepwise hopping among surface sites with relatively lower energies. When NCs become smaller, the surface to volume ratio increases leading to an increase in the relative concentration of surface defect states. This increase in surface trap states can indeed explain the shorter exciton lifetimes at higher energies, when the lifetime is dominated by the fast w_{trap} . With these observations Hamanaka *et al.*⁴ state that they contradict the earlier statement of Ueng *et al.*⁹ that intrinsic defects leading to acceptor and donor states are the origin of emission. However, when $w_{\text{trap-non-rad}}$ increases, leading to a shorter exciton lifetime, the $w_{\text{trap-rad}}$ can still originate from donor-acceptor recombination. Furthermore, as discussed in chapter 2, the global Stokes shift is always larger

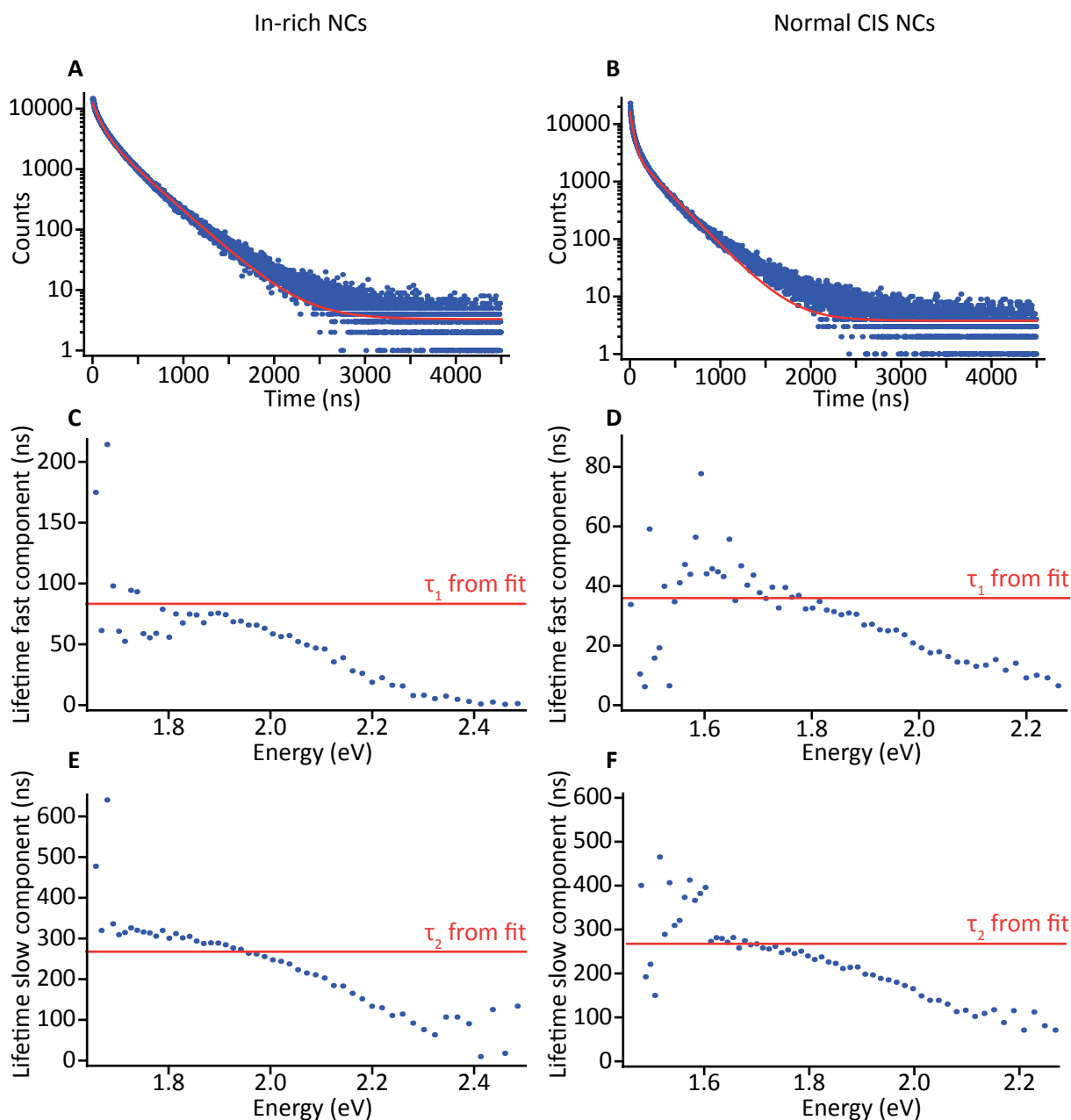


Figure 3.8. A: Bi-exponential fit of the total decay curve of the In-rich NCs. B: Bi-exponential fit of the total decay curve of the stoichiometric CIS NCs. C: Plot of the lifetime of the fast component as function of energy in the In-rich NCs. D: Plot of the lifetime of the fast component as function of energy in the stoichiometric NCs. E: Plot of the lifetime of the slow component as function of energy in the In-rich NCs. F: Plot of the lifetime of the slow component as function of energy in the stoichiometric CIS NCs.

than the actual Stokes shift at single crystal level, therefore Hamanakas proposition that the Stokes shift is too large to be explained by donor-acceptor transitions⁴ is debatable.

When comparing Figure 3.8C and E, showing the lifetime of the fast component (C) and the slow component (E) of the In-rich NCs as function of energy, it becomes clear from the large difference in timescale that at least two completely different radiative decay channels are present in the NCs. The same holds for the lifetime of the fast (D) and slow (F) components of the normal CIS NCs. The red horizontal line in the plots with lifetime versus energy (Figure 3.8C t/m F) indicates the average lifetime of the fast and slow component obtained from the fit (Figure 3.8A and B). It is clear from all these figures that the

bi-exponential fit may not be the best choice and a more complicated model for the different decay channels should be developed. Although a tri-exponential fit for CIS NCs has been reported several times,¹²⁻¹⁴ a validated physical explanation or proposed model for this fit has not yet been proposed.

3.4. Conclusions & outlook

CIS NCs were synthesized and their emission and absorption wavelengths are easy to tune by varying reaction conditions. The luminescence of the colloidal CIS NCs synthesized under inert atmosphere is not stable under air and it would be interesting to investigate the behavior of the under air synthesized NCs. EDS measurements indicate that the copper indium ratio should be at maximum 1:1 to observe luminescence. When the 1:1 ratio is decreased the luminescence becomes stronger while the lifetimes become longer. The longer decay times are a strong indication that the indium atoms are very important for the luminescent behavior of the CIS NCs. Given the fact that CIS is a n-type semiconductor, the increase in luminescence efficiency suggests that indium atoms are the main source of the electrons involved in the decay mechanism. The decreasing lifetimes with increasing band gap energies are explained by Hamanaka *et al.* using the hopping mechanism, thereby concluding that surface energy states are the (or an) origin of the CIS emission. Measurements on more samples, at lower temperatures and excitation measurements could reveal more about the origin of the luminescence in CIS. For all samples high-resolution TEM analysis would give more insight in the influence of synthesis conditions on the crystal structure of the NCs and possibly leads to more information on the luminescence dependence thereof.

3.5. References

1. Kolny-Olesiak, J. & Weller, H. Synthesis and application of colloidal CuInS₂ semiconductor nanocrystals. *ACS Appl. Mater. Interfaces* **5**, 12221–37 (2013).
2. Lu, X., Zhuang, Z., Peng, Q. & Li, Y. Controlled synthesis of wurtzite CuInS₂ nanocrystals and their side-by-side nanorod assemblies. *CrystEngComm* **13**, 4039 (2011).
3. Li, L. et al. Efficient Synthesis of Highly Luminescent Copper Indium Sulfide-Based Core/Shell Nanocrystals with Surprisingly Long-Lived Emission. *J. Am. Chem. Soc.* **133**, 1176–1179 (2011).
4. Hamanaka, Y. et al. Defect-induced photoluminescence and third-order nonlinear optical response of chemically synthesized chalcopyrite CuInS₂ nanoparticles. *Chem. Phys. Lett.* **466**, 176–180 (2008).
5. Uehara, M., Watanabe, K., Tajiri, Y., Nakamura, H. & Maeda, H. Synthesis of CuInS₂ fluorescent nanocrystals and enhancement of fluorescence by controlling crystal defect. *J. Chem. Phys.* **129**, 134709 (2008).
6. Chen, B. et al. Highly Emissive and Color-Tunable CuInS₂-Based Colloidal Semiconductor Nanocrystals: Off-Stoichiometry Effects and Improved Electroluminescence Performance. *Adv. Funct. Mater.* **22**, 2081–2088 (2012).
7. De Mello Donegá, C. & Koole, R. Size Dependence of the Spontaneous Emission Rate and Absorption Cross Section of CdSe and CdTe Quantum Dots. *J. Phys. Chem. C* **113**, 6511–6520 (2009).
8. Kim, Y.-K., Ahn, S.-H., Chung, K., Cho, Y.-S. & Choi, C.-J. The photoluminescence of CuInS₂ nanocrystals: effect of non-stoichiometry and surface modification. *J. Mater. Chem.* **22**, 1516 (2012).
9. Ueng, H. Y. & Hwang, H. . The defect structure of CuInS₂. Part I: intrinsic defects. *J. Phys. Chem. Solids* **50**, 1297–1305 (1989).
10. Lewerenz, H. J. & Dietz, N. Defect identification in semiconductors by Brewster angle spectroscopy. *J. Appl. Phys.* **73**, 4975–4987 (1993).
11. Binsma, J. J. M., Giling, L. J. & Bloem, J. Luminescence of CuInS₂. II exciton and near edge emission. *J. Lumin.* **55–72** (1982).
12. Seo, J. et al. Time-resolved and temperature-dependent photoluminescence of ternary and quaternary nanocrystals of CuInS₂ with ZnS capping and cation exchange. *J. Appl. Phys.* **114**, 094310 (2013).
13. Komarala, V. K., Xie, C., Wang, Y., Xu, J. & Xiao, M. Time-resolved photoluminescence properties of CuInS₂/ZnS nanocrystals: Influence of intrinsic defects and external impurities. *J. Appl. Phys.* **111**, 124314 (2012).
14. Ramasamy, K., Malik, M. A., Revaprasadu, N. & O'Brien, P. Routes to Nanostructured Inorganic Materials with Potential for Solar Energy Applications. *Chem. Mater.* **25**, 3551–3569 (2013).

4. Synthesis and optical properties of colloidal CIS-based alloy and core/shell nanocrystals

4.1. Introduction

In order to be used in devices, colloidal NCs must have a high photoluminescence quantum yield and stability under ambient conditions. As shown in the previous chapter, the emission of the CIS NCs is not stable under air. Stability and efficiency of the luminescence of NCs could be improved by growth of a shell of a wide band gap semiconductor.¹ When a shell with a larger band gap is grown around a luminescent core NC, a heteronano-crystal (HNC) is created. Because the surface dangling bonds of the core NCs are satisfied, less trap states exist leading to a possible increase in luminescence efficiency. Depending on the band offsets of the core and shell materials the exciton as a whole or only one of the charge carriers becomes more confined.

In this chapter the growth of shells of different materials over CIS NCs is investigated. Cadmium sulfide, leading to a type II HNC, resulting in a red shift in emission, was grown over pre-synthesized CIS NCs. However, the main focus was on zinc sulfide shells, since the non-toxicity of CIS/ZnS NCs combined with possibly enhanced stability and optical properties, is a unique selling point. A zinc sulfide shell around a CIS core would result in a type I HNC. Cadmium sulfide and zinc sulfide are not only suitable shell materials regarding their bandwidths and offsets, the lattice mismatch with CIS is also very small. The lattice parameter a of CIS is 0.5517 nm, for ZnS $a=0.5345$ nm and for CdS $a= 0.5820$ nm.²

Although a lot of studies have already been performed on growing a zinc sulfide shell around CIS cores, only blue-shifted results are reported.³⁻⁷ This blue shift in emission and absorption indicates alloying of the NC instead of shell growth, since none of the possible band alignment types could explain an increase in the band gap. We investigated numerous precursor combinations, reaction temperatures and synthesis methods, to obtain the right reaction conditions for the desired heteroepitaxial growth. Analysis of the resulting NCs indeed indicates the formation of true CIS/ZnS core/shell nanocrystals.

4.2. Experimental

4.2.1. Materials

Copper (I) iodide (Sigma Aldrich, 98%), Indium (III) acetate (Sigma Aldrich, 99.99%), 1-dodecanethiol (DDT, Sigma Aldrich, $\geq 98\%$), Trioctylphosphine (TOP, Fisher Scientific), Zinc (II) Chloride (Sigma Aldrich, 98+%), Zinc (II) stearate (Sigma Aldrich, 10-12% Zn basis), Cadmium (II) oxide (Sigma Aldrich, 99.5%),

Oleic Acid (Oleic acid (OA, Sigma Aldrich, 90%), 1-octadecene (ODE, Sigma Aldrich, tech. 90%), Sulfur (Sigma Aldrich, 99.98%), Oleylamine (OLAM, Sigma Aldrich, tech. 70%), Octadecylamine (ODA, Sigma Aldrich, tech. 90%), Toluene (Sigma Aldrich, 99.8%), Methanol (Sigma Aldrich, 99.8%), 1-Butanol (Sigma Aldrich, 99.8%), Ethanol (Sigma Aldrich, ≥99.8%). ODE, OLAM, ODA and zinc stearate were degassed at for 2 hours at 150-220 °C before usage.

4.2.2. Synthesis

For the synthesis of the CIS cores, a protocol reported by Lu *et al.*⁸ was followed. CuI (0.4 mmol), In(Ac)₃ (0.4 mmol) and 5 mL DDT were mixed under inert atmosphere and degassed for 1 hour at 80 °C. Then the temperature was raised to 210 °C under N₂ flow and after 40 minutes reaction cooled to room temperature. The NCs were washed with ethanol or a methanol/butanol mixture and dispersed in toluene. The optical properties of the obtained CIS NCs showed to be very reproducible, see Appendix D.

Cadmium oleate was prepared by dissolving 3 mmol CdO in 3.9 mL OA and 3.9 mL ODE. The mixture was heated to 260 °C under N₂ flow and then degassed for 20 min at 100 °C. Sulfur-ODE was prepared by dissolving 160 mg sulfur in 50 mL ODE. The mixture was heated to 220 °C and stirred until a clear solution was obtained.

Following the protocol of Li *et al.*,³ the cadmium sulfide shell was grown directly in the crude reaction mixture of the CIS cores. Half of this crude mixture was diluted with 2.5 mL ODE. Cadmium oleate (4 mL, 0.1 M), 0.4 mL TOP, 12.8 mg sulfur and 1 mL ODE were mixed and added drop wise over 20 minutes at temperatures of 210 °C or 230 °C. After addition at 210 °C there was no additional reaction time and the reaction was immediately quenched by cooling to room temperature (RT). After addition at 230 °C the mixture was allowed to react for 20 minutes, after which the reaction was quenched by cooling to RT.

Most of the zinc sulfide shell experiments were performed with the seed-injection technique: the zinc precursor (zinc chloride or zinc stearate, 0.32 mmol) was dissolved in 4 mL ODE and degassed for 30 min at 100 °C. The CIS core NCs (4 mL of the purified NCs in toluene) were redispersed in 2 mL DDT or 3 mL S-ODE. The cores and sulfur precursor were injected to the zinc solution at 150-210 °C and reacted 30-180 min. In other ZnS shell experiments, the drop wise addition method, the CIS NCs (4 mL of the purified NCs in toluene) were redispersed in 3 mL S-ODE, 1 mL ODE and 0.09 mmol ODA and heated to 210 °C. Zinc chloride (0.15 mmol) dissolved in 3 mL ODE and 1 mL OLAM was added drop wise, in portions of 0.5-1.5 mL, 0.1 mL per minute and 10 minutes between two additions.

An overview of the exact reaction conditions per sample is given in Appendix E.

4.2.3. Characterization

Absorption spectra were recorded with a Perkin Elmer Lambda 950 UV/VIS/NIR spectrophotometer. Luminescence measurements were performed with an Edinburgh Instruments FLS920 spectrofluorimeter equipped with a 450 W Xe lamp and double excitation monochromator with a grating blazed at 300 nm. The signal was detected with a Hamamatsu R928 PMT detector with a grating blazed at 500 nm or, when the emission was at 800 nm or longer wavelengths, with an Acton research SpectraPro 300i CCD camera with optical fiber. For lifetime and time-resolved emission map measurements excitation was carried out with an Edinburgh Instruments EPL445 picosecond pulsed diode laser at 441.1 nm and a pulse width of 80.2 ps. The signal was detected with a Hamamatsu photosensor module H10720-01. Lifetimes were obtained from a bi-exponential fit of the decay curve. Transmission electron microscopy (TEM) images were taken with a Philips Tecnai microscope (FEI company), with an accelerating voltage of 100 or 120 kV. TEM pictures were used to measure NC sizes. Typically 100 NCs were measured by hand in the program iTEM from Soft Imaging System GmbH, after which the average and standard deviation were given. Energy dispersive X-ray spectroscopy (EDS) measurements were performed with a FEI Tecnai-20F microscope equipped with a Field Emission Gun, a Gatan 694 CCD camera and an EDA spectrometer. The microscope was operated at 200 kV. Acquisition time for the EDS measurements was 45 s. Large areas (containing approximately 10^4 - 10^5 NCs) were measured to obtain representative data. Quantum yield estimations for a few samples were made based on the assumed quantum yield of 60% of the sample RM 571 and with the formula:

$$QY_{\text{sample}} = (1 - T_{\text{ref}}) / (1 - T_{\text{sample}}) \cdot \Phi_{\text{sample}} / \Phi_{\text{ref}} \cdot QY_{\text{ref}}$$

where T is the transmission at 400 nm and Φ the integrated photon flux. An overview of the values obtained is given in Appendix C.

4.3. Results & discussion

4.3.1. Reaction steps towards shell formation and competing processes

The growth rate of a shell around a seed nanocrystal is determined by the same processes described in chapter 3: monomer formation and diffusion and their final reaction at the NC surface to form the shell material. Hetero epitaxial growth, the formation of a material on the surface of another material, is influenced by several other factors, such as the binding strength of the ligands to the surface of the NC and interfacial strain due to lattice mismatch.¹ When the growth rate of the shell is too slow and it takes too long to form a stable layer of the material around the seed NC, the monomers can react with the seed NC and cation exchange or alloying processes can occur. In the sections below, the formation of CdS and ZnS shells around the CIS NCs is discussed in this context.

4.3.2. Cadmium sulfide shell

In the first synthesis the shell precursors were added at 210 °C, after which the reaction was immedi-

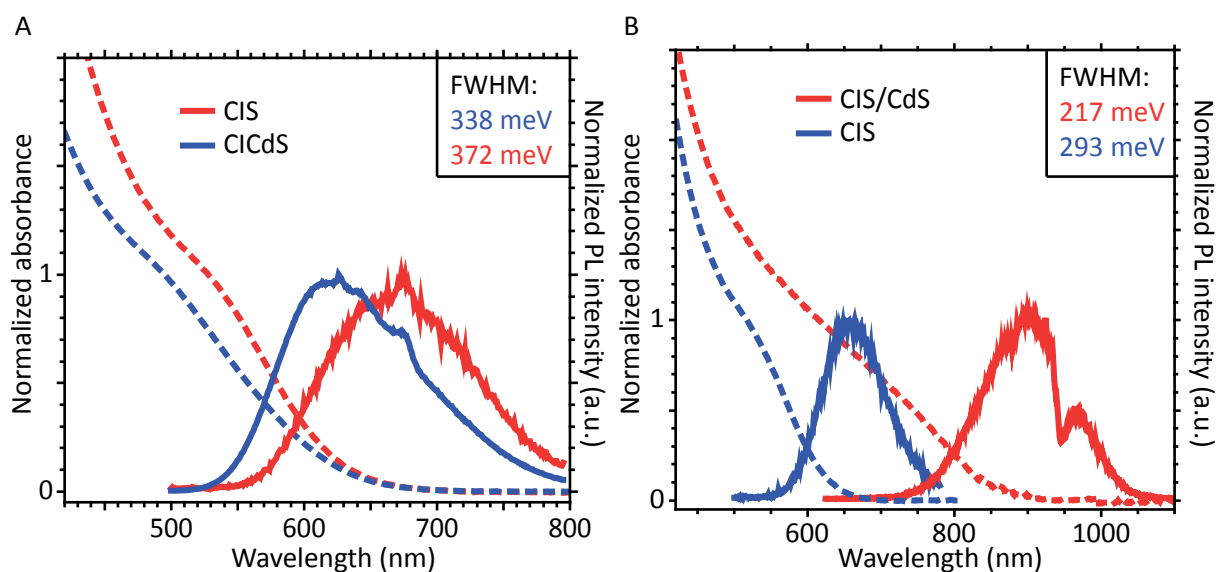


Figure 4.1. A: Absorption (dashed lines) and emission (solid lines) of the CIS seeds and the resulting NCs after dropwise addition at 210 °C of cadmium precursor and no reaction time. The absorption and emission spectra of the resulting sample are shifted to the blue, indicating alloying. B: Absorption (dashed lines) and emission (solid lines) of the CIS seeds and the resulting NCs after dropwise addition of cadmium precursor at 230 °C and 20 minutes reaction. The absorption and emission spectra of the resulting sample are shifted to the red, indicating shell growth.

ately stopped. The absorption and emission spectra of the obtained samples are blue shifted by 224 meV with respect to those of the original CIS cores (Figure 4.1A). This means that the NCs were alloyed resulting in a larger band gap since the band gap of CdS is larger (2.4 eV for bulk) than that of CIS. The blue shifted emission peak shows a better signal-to-noise ratio than the emission peak of the seeds, which can be an indication of an increased luminescence efficiency.

To accelerate the shell growth, a synthesis was carried out at a higher temperature of 230 °C. Due to the high temperature, the reactivity of the precursors increases and the diffusion of the monomers and the final reaction are faster. To allow growth of a shell with reasonable thickness, the mixture was left 20 minutes at 230 °C after addition of the cadmium precursors. The absorption and emission spectra of the resulting samples are shown in Figure 4.1B. A large red shift of 507 meV with respect to the seeds is observed, indicating that a shell has formed. A red shift after shell growth is explained by the type II band alignment (see chapter 2), where the charge carriers are spatially separated, leading to a minimized overlap of their wave functions. A type II band alignment an expected result with regard to the band offsets of CIS and CdS (see figure Figure 2.6B) and the results reported earlier by Li *et al.*³ and Huang *et al.*⁹ Since TOP is present in the reaction mixture and this ligand binds very strongly to copper which is then extracted from the core, presumably first alloying takes place before the shell grows. This is confirmed with the observations regarding the first CdS shell synthesis, where directly after addition alloying has taken place.

4.3.3. Precursor reactivity and synthesis temperature

A. Zinc stearate and DDT

Reaction with zinc stearate and DDT as zinc and sulfur precursor respectively results in blue shifted

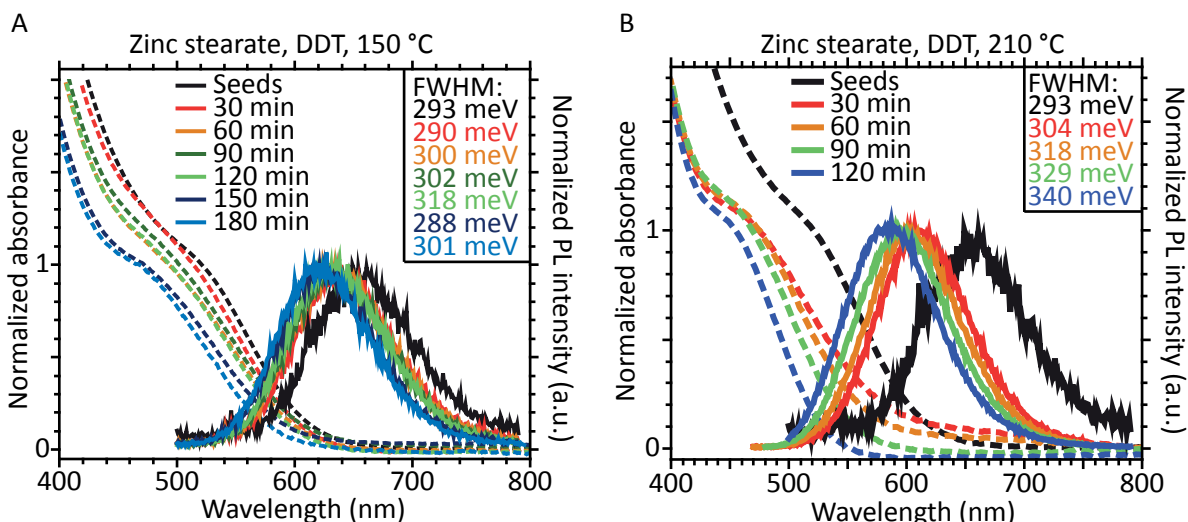


Figure 4.2. A: Absorption (dashed lines) and emission (solid lines) of the CIS seeds and the resulting NCs after reaction with zinc stearate and DDT at 150 °C. The absorption and emission spectra of the resulting sample are shifted to the blue, indicating alloying. B: Absorption (dashed lines) and emission (solid lines) of the CIS seeds and the resulting NCs after reaction with zinc stearate and DDT at 210 °C. The absorption and emission spectra of the resulting sample are shifted to the blue, indicating alloying.

emission and absorption spectra with respect to the spectra of the CIS seeds. After 180 min reaction at low temperature (150 °C) the final sample was shifted 100 meV to the blue (Figure 4.2A), after 120 min reaction at high temperature (210 °C) this blue shift was already 229 meV (Figure 4.2B). These large blue shifts are a strong indication that alloying takes place and the increased shift at high temperature shows that the process goes faster at high temperature. The latter observation indicates that the formation of monomers is the rate limiting step in this reaction, which results in a too low availability of building blocks at the NC surface to form a shell. The signal-to-noise ratio of the alloyed NCs is improved with regard to the parent NCs, which is an indication that the luminescent quantum efficiency improved upon alloying.

In Figure 4.3 the stability under air of an alloyed sample is shown. After two hours under air a decrease

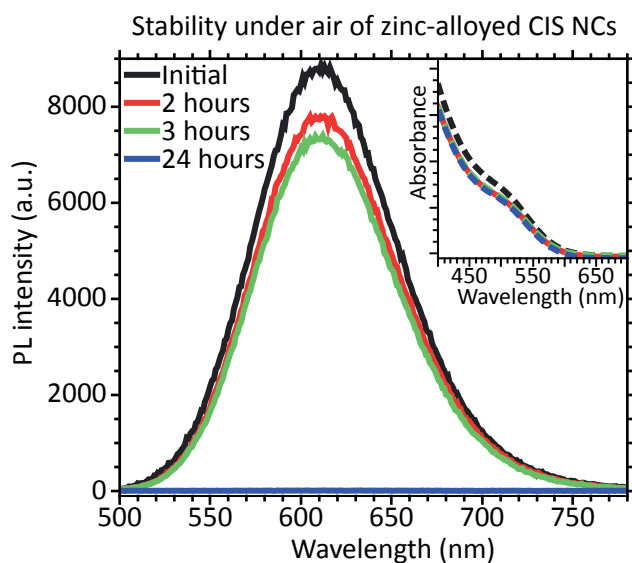


Figure 4.3. Stability of the photoluminescence of zinc-alloyed CIS NCs when exposed to air. After 24 hours under air the emission is completely quenched

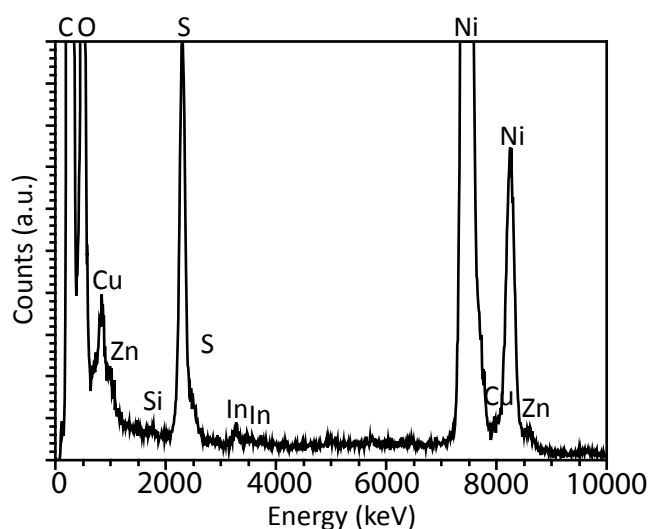


Figure 4.4. EDS spectrum of resulting (alloyed) sample after 120 min reaction with zinc stearate and DDT at 210 °C.

Table 4.1. Elemental ratio in NCs after 120 in reaction with zinc stearate and DDT at 210 °C. Two measurements at different locations on the TEM grid were performed.

	_01	_02
	Atomic%	Atomic%
S	87.006	86.257
Cu	7.819	6.715
Zn	3.178	3.632
In	1.995	3.394
S:Cu	11.1	12.8
Cu	1	1
Zn:Cu	0.41	0.54
In:Cu	0.26	0.51
	$\text{Cu}_1\text{Zn}_{0.4}\text{In}_{0.3}$	$\text{Cu}_1\text{Zn}_{0.5}\text{In}_{0.5}$

of 12% is observed, after 3 hours a decrease of 17% relative to the initial emission intensity. After 24 hours the emission is completely quenched, which is no improvement with regard to the parent CIS NCs (see Figure 3.2B). This observation confirms that the main process in these reactions is alloying and the stability of the luminescence is not improved.

EDS measurements were performed to investigate the stoichiometry of the NCs obtained. The spectrum is shown in Figure 4.4 and the atomic ratio deduced is shown in Table 4.1. It is clear that the charges detected are unbalanced, which is probably due to a malfunctioning of the device, as reported in chapter 3. The cause for this is not known and since the device showed artifacts like this before, the values obtained for sulfur are left out the calculations of the atomic ratios. Since no characteristic ZnS absorption or emission is observed,¹⁰ the zinc measured with EDS has to be incorporated in the CIS NCs. The Zn:In ratio is 1:1 and this suggests that the indium is replaced by the zinc. This is remarkable since De Trizio *et al.*⁴ stated an zinc exchange for copper after a reaction with similar conditions. Both observations cannot be explained yet and more measurements and calculations should be performed to be conclusive on this matter.

B. Zinc sulfide shell formation with zinc chloride and DDT

The results from the section above suggested that the precursors used were not reactive enough, which resulted in a too low availability of the monomers and alloying instead of shell growth as a consequence. A more reactive zinc precursor is zinc chloride, which was used in a synthesis at low temperature (150 °C) and at high temperature (210 °C) with DDT as sulfur precursor. At low temperature this again resulted in a large blue shift in absorption and emission (225 meV) with respect to the parent CIS NCs (see Figure 4.5A) which is again interpret as alloying of CIS with zinc, resulting in copper indium zinc sulfide (CIZS) NCs. After a reaction at high temperature, an initial blue shift in the absorption and emission spectra is observed (183 meV) compared to the parent CIS NCs, after which a small red shift of

41 meV indicates that after the alloying process a shell is formed. This small redshift is explained by the Type 1½ band alignment of CIZS and ZnS, which results in delocalization of (in this case) the electron over the whole NC and thus less overlapping wave functions. The stability of the emission under air was measured and the result is shown in Figure 4.5C. The increase in intensity is caused by the increased concentration of the sample due to evaporation of the solvent. The fact that the intensity does not decrease is a strong confirmation of shell formation. The surface of the luminescent core is now protected against oxidation so no extra defect states within the band gap, that facilitate non-radiative relaxation and ultimately quench all the luminescence, will occur. EDS measurements were performed to investigate the stoichiometry of the presumably CIZS/ZnS HNCs. The EDS spectrum is shown in Figure 4.5D and the corresponding atomic ratios are listed in Table 4.2. Again the amount of anions was not balanced with the amount of cations, so the first were left out of the calculations, resulting in a $\text{Cu}_1\text{Zn}_{2.7}\text{In}_{0.5}$

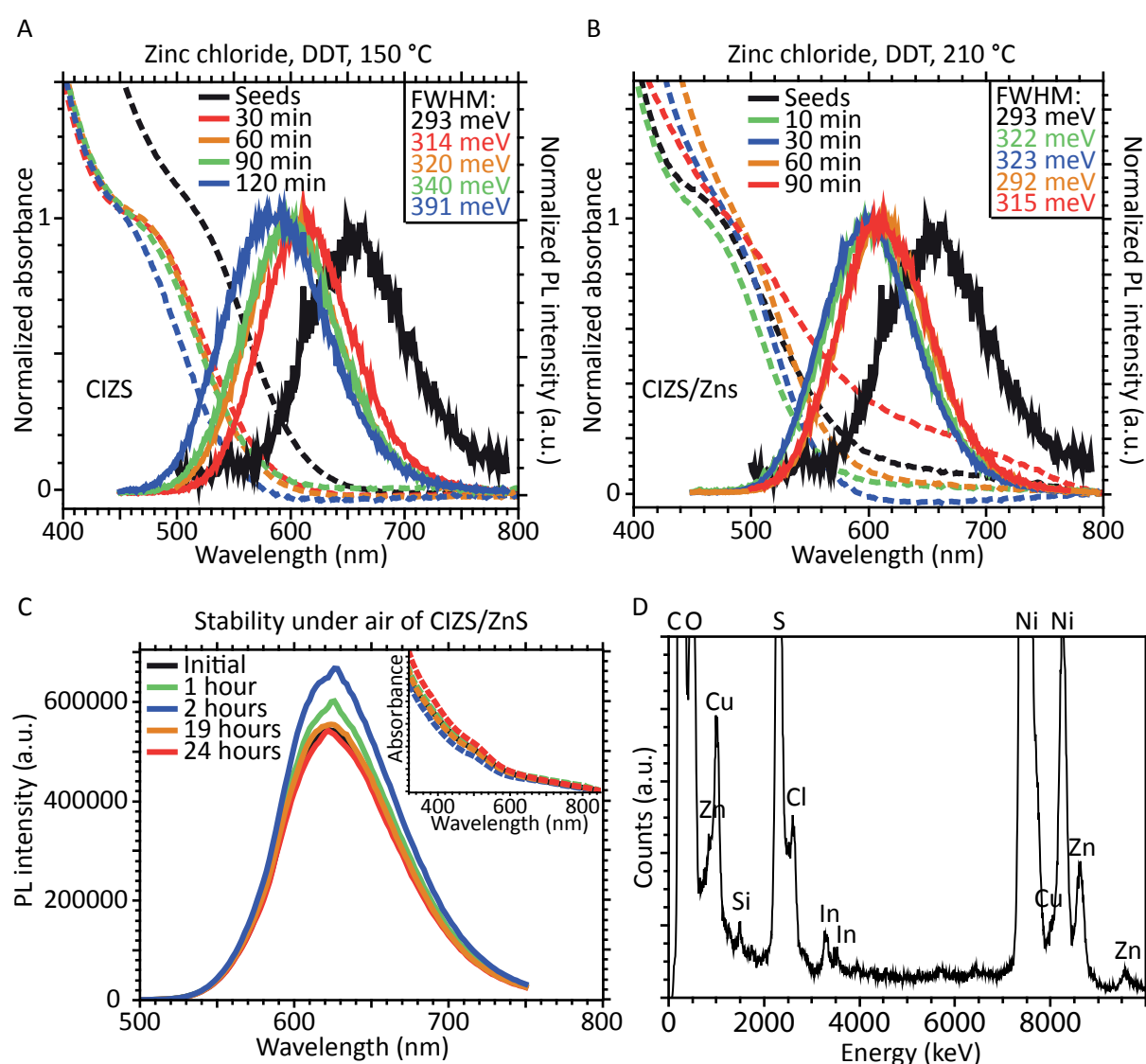


Figure 4.5. A: Absorption (dashed lines) and emission (solid lines) of the CIS seeds and the resulting NCs after reaction with zinc chloride and DDT at 150 °C. The absorption and emission spectra of the resulting sample are shifted to the blue, indicating alloying. B: Absorption (dashed lines) and emission (solid lines) of the CIS seeds and the resulting NCs after reaction with zinc chloride and DDT at 210 °C. The absorption and emission spectra of the resulting sample first shifted to the blue, indicating alloying, after which a small red shift is observed, indicating shell growth. C: Stability of the photoluminescence of CIZS/ZnS HNCs when exposed to air. No quenching of emission is observed. D: EDS spectrum of resulting CIZS/ZnS sample after 90 min reaction with zinc chloride and DDT at 210 °C.

Table 4.2. Elemental ratio of the (CIZS/ZnS) NCs after reaction with zinc chloride and DDT at 210 °C. Two different at different locations in the sample were performed

	_01	_02
	Atomic%	Atomic%
S	83.234	69.404
Cl	7.246	11.175
Cu	2.243	6.051
Zn	6.084	11.63
In	1.191	1.737
S:Cu	37.12	11.47
Cl:Cu	3.23	1.85
Cu	1	1
Zn:Cu	2.71	1.92
In:Cu	0.53	0.29
	$\text{Cu}_1\text{Zn}_{2.7}\text{In}_{0.5}$	$\text{Cu}_1\text{Zn}_{1.9}\text{In}_{0.3}$

ratio at the first location on the grid measured, and a $\text{Cu}_1\text{Zn}_{1.9}\text{In}_{0.3}$ ratio at the second spot. The Cu:In ratio is again smaller than one, indicating an exchange of indium for zinc, since in the parent CIS NCs the Cu:In ratio was at maximum 1:1. Since the initial blue shift is very large and comparable with the blue shift obtained for the zinc stearate at high temperature sample, the assumption is made that the degree of alloying in this zinc chloride sample is comparable as well. When the stoichiometry obtained for the zinc stearate sample (Table 4.1, Zn:In is 1:1) is used for the core NCs in this CIZS/ZnS sample and the sulfur ratio is adapted to the cation ratios, the resulting stoichiometry is $\text{Cu}_1\text{Zn}_{0.5}\text{In}_{0.5}\text{S}_{1.75}/\text{Zn}_{2.2}\text{S}_{2.2}$ for the first spot and $\text{Cu}_1\text{Zn}_{0.3}\text{In}_{0.3}/\text{Zn}_{1.6}\text{S}_{1.6}$ for the second.

C. Zinc chloride and S-ODE

The use of a more reactive zinc precursor led to fast initial alloying, after which a shell grew. This indicates that part of the monomer availability problem was solved, but not completely. As more reactive sulfur precursor S-ODE can be used, instead of DDT. After reaction at 190 °C, the absorption and emission spectra of the obtained NCs were shifted to the red with respect to the parent NCs (Figure 4.6). The red shift indicates formation of HNCs with Type I½ carrier localization regime, where the electron and hole are (partially) spatially separated. This indication of shell formation shows that the precursors zinc chloride and S-ODE at 190 °C are sufficiently reactive to provide enough monomers for shell formation. The signal to noise ratio however is large, indicating a low luminescence efficiency. This is probably caused by a lot of (surface related) defects, since there were no ligands present in the reaction mixture to stabilize the NCs.

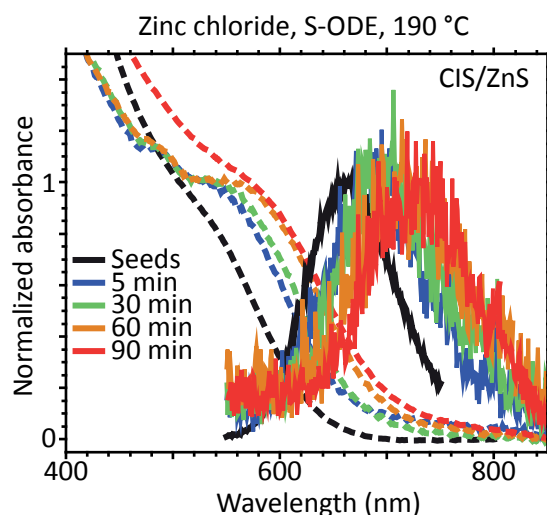


Figure 4.6. Absorption (dashed lines) and emission (solid lines) of the CIS seeds and the resulting NCs after reaction with zinc chloride and S-ODE at 190 °C. The absorption and emission spectra of the resulting sample are shifted to the red, indicating shell growth.

D. Optimization of the zinc sulfide shell synthesis

With the reactive precursors zinc chloride and S-ODE it is possible to synthesize a ZnS shell around CIS NCs, resulting in a red shift in the absorption and emission spectra of the resulting HNCs with respect to the parent CIS NCs. To stabilize these HNCs, ligands should be added to the reaction mixture. Two possibilities are DDT and OLAM, which were both used in a reaction at 210 °C. The NCs obtained with the DDT containing synthesis procedure show an initial blue shift in the absorption and emission spectra (110 meV) with respect to the parent CIS NCs, after which a small redshift of 28 meV is observed (Figure 4.7A). This result is very similar to the above discussed synthesis with zinc chloride and DDT used as zinc and sulfur precursor respectively where an initial blue shift of 183 meV was observed, followed by a red shift of 41 meV (see Figure 4.5B). These observations indicate that the presence of DDT plays

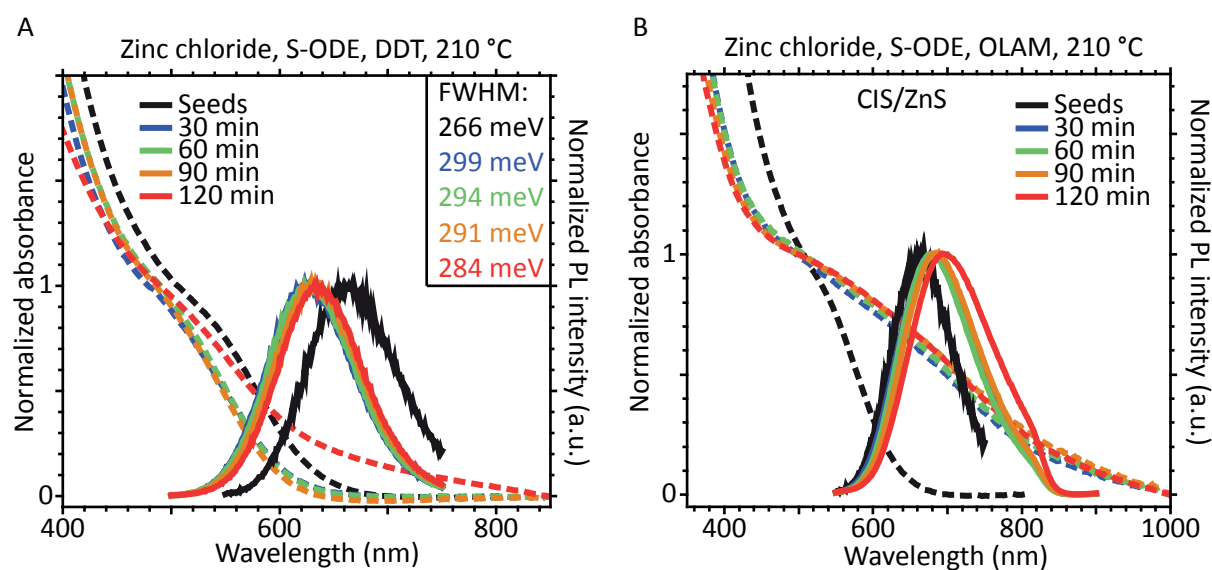


Figure 4.7. A: Absorption (dashed lines) and emission (solid lines) of the CIS seeds and the resulting NCs after reaction with zinc chloride, S-ODE and DDT at 210 °C. The absorption and emission spectra of the resulting sample first shifted to the blue, indicating alloying, after which a small red shift is observed, indicating shell growth. B: Absorption (dashed lines) and emission (solid lines) of the CIS seeds and the resulting NCs after reaction with zinc chloride, S-ODE and OLAM at 210 °C. The absorption and emission spectra of the resulting sample shift to the red, indicating shell growth. The signal-to-noise ratio is much better than for earlier samples (Figure 4.6).

a major role in the availability of monomers, even when more reactive precursors are present. This suggests that DDT can bind to zinc cations, which are thereby hindered to diffuse to the surface. The zinc that is already present on the surface can then diffuse into the CIS NCs, because it is not captured in a solid shell layer. The HNCs obtained with the OLAM containing synthesis show a clear red shift in absorption and emission spectra compared to the parent CIS NCs (see Figure 4.7B). The odd shape of the emission spectra above 750 nm is due to the detector sensitivity at wavelengths longer than 750 nm. The red shift and the better signal to noise ratio are both indications that again a shell was formed and the NCs were sufficiently stabilized by the ligands.

The shape of the absorption band of the obtained HNCs has changed remarkably with respect to the absorption band of the parent CIS NCs. The absorption band offset is at much longer wavelengths for the HNCs (roughly 900 nm compared to 660 nm) and is much broader. The offset at lower energies indicates that the band gap decreased (so NCs became larger) and the broadening is in indication of an increased size dispersion. The width of the emission peak cannot be measured reliably since the detector changes the shape of the spectrum from 750 nm, which is exactly at the position at half of the maximum intensity. Therefore the suggested increase in size dispersion cannot be discussed with regard to the emission peak width. The global Stokes shift which is very large for the parent CIS NCs is decreased in the spectra of the CIS/ZnS NCs, which can be an important observation with regard to the discussion on the nature of the emitting states in both CIS NCs as the CIS/ZnS HNCs.

Analysis of the CIS/ZnS sample with TEM showed, as expected with regard to the broadened absorption band, a very polydisperse sample, where roughly three different types of NCs can be distinguished. The three different types are shown in Figure 4.8B-D and marked with a number that refers to the EDS spectra in Figure 4.8A and the atomic ratios in Table 4.3. The EDS analysis shows that the NCs not only differ in shape and size, but also in composition. The large hexagonal shapes denoted with 03 have a diameter of (143.5 ± 11.9) nm and consist of copper sulfide (Cu_2S). The smallest crystals marked with 05 have a diameter of (8.11 ± 1.1) nm and can according to the EDS measurements either be CIZS alloyed NCs ($\text{Cu}_1\text{Zn}_{0.5}\text{In}_{0.6}\text{S}_{1.8}$) or core/shell NCs ($\text{Cu}_1\text{In}_{0.6}\text{S}_{1.3}/\text{Zn}_{0.5}\text{S}_{0.5}$). The latter is unlikely since then indium would have diffused out of the parent CIS NCs, while for the first the more often observed exchange of indium for zinc is observed, resulting in the Zn:In ratio of 1:1. The EDS results of the intermediate sized hexagonal platelets with diameter (13.7 ± 1.7) nm indicate either a $\text{Cu}_1\text{Zn}_{0.5}\text{In}_1\text{S}_{2.6}$ stoichiometry or a $\text{Cu}_1\text{In}_1\text{S}_2/\text{Zn}_{0.5}\text{S}_{0.6}$ structure. Since a red shift in emission and absorption is observed and this is unlikely to happen for alloyed NCs, these hexagonal structures are expected to be CIS/ZnS core/shell NCs. The stability of the luminescence that is observed for this ensemble was measured as well, and the resulting spectra are shown in Figure 4.9. The intensity of the luminescence decreased but is not quenched completely, which can be explained by the composition of the ensemble proposed above: the luminescence of the CIZS NCs is quenched under air, while the luminescence of the CIS/ZnS core/shell NCs is protected from oxidation.

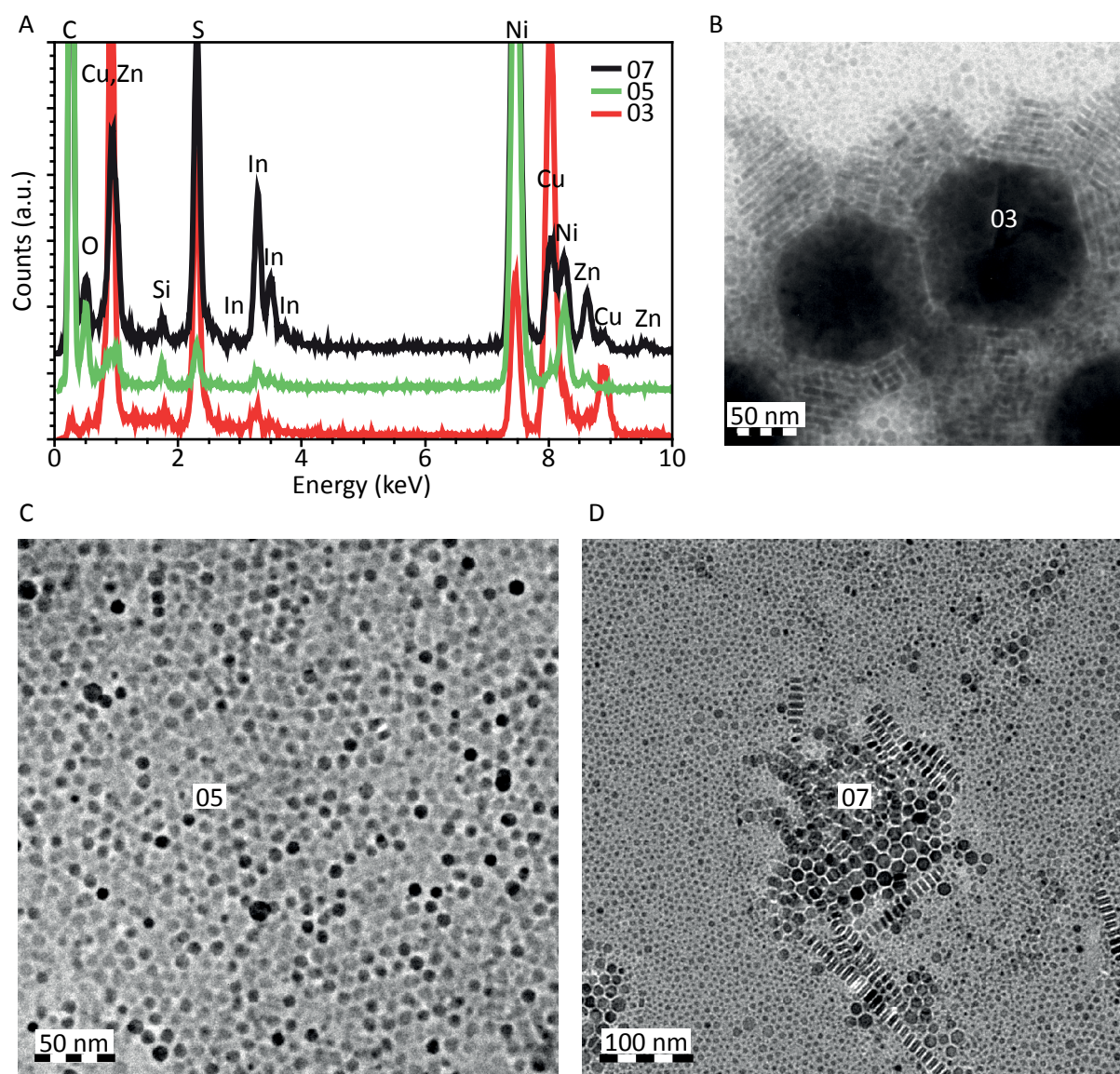


Figure 4.8. EDS spectra of the three different regions shown in B,C and D of the sample obtained after reaction with zinc chloride, S-ODE and OLAM after 120 minutes at 210 °C. B, C and D show TEM images of the three different NCs that could be observed after this reaction.

Table 4.3. Ratio of the elements present in the CIZS and CIZS/ZnS NCs. The values in the first row refer to the numbers in Figure 4.11B, C and E.

	03	05	07
	Atomic%	Atomic%	Atomic%
S	32.546	46.107	51.387
Cu	62.283	29.945	19.747
Zn	2.938	13.386	10.059
In	2.23	14.561	18.805
S:Cu	0.52	1.78	2.6
Cu	1	1	1
Zn:Cu	0.05	0.52	0.51
In:Cu	0.04	0.56	0.95
	$\text{Cu}_1\text{S}_{0.5}$	$\text{Cu}_1\text{Zn}_{0.5}\text{In}_{0.6}\text{S}_{1.8}$	$\text{Cu}_1\text{Zn}_{0.5}\text{In}_{1.2}\text{S}_{2.6}$
		$\text{Cu}_1\text{In}_{0.6}\text{S}_{1.3}/\text{Zn}_{0.5}\text{S}_{0.5}$	$\text{Cu}_1\text{In}_{1.2}\text{S}_{2.6}/\text{Zn}_{0.5}\text{S}_{0.6}$

The large increase in size and the distinct shape of the structures is remarkable, since according to the EDS atomic ratio's, the shell contains much less ions than the core and thus is expected to be thin. However, the crystals have grown severely. At his point there is no explanation for this observation.

Since the emission peak is still shifting to the red after 120 minutes reaction at 210 °C (see Figure 4.7B), a new synthesis was performed with the same conditions but a longer reaction time. The absorption and emission spectra of the resulting sample are shown in Figure 4.10A and the red shift of the emission peak after 3 hours reaction is 126 meV with respect to the parent CIS NCs, comparable with the red shift of 91 meV after 1.5 hours of the first synthesis. The global Stokes shift for this longer reaction is even smaller than for the earlier reaction and the offset of the absorption band is again at much lower energies than for the parent CIS NCs. Analysis with TEM (Figure 4.10B) shows again a polydisperse

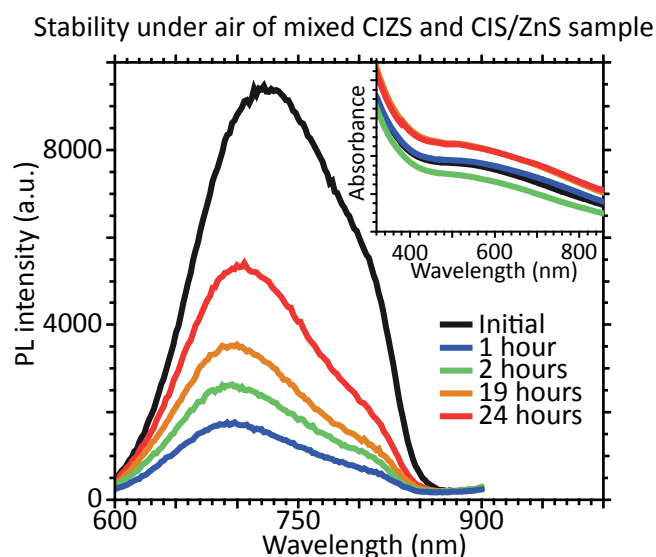


Figure 4.9. Stability of the photoluminescence of the mixed CIZS and CIS/ZnS sample when exposed to air. After 24 hours under air the emission is not completely quenched.

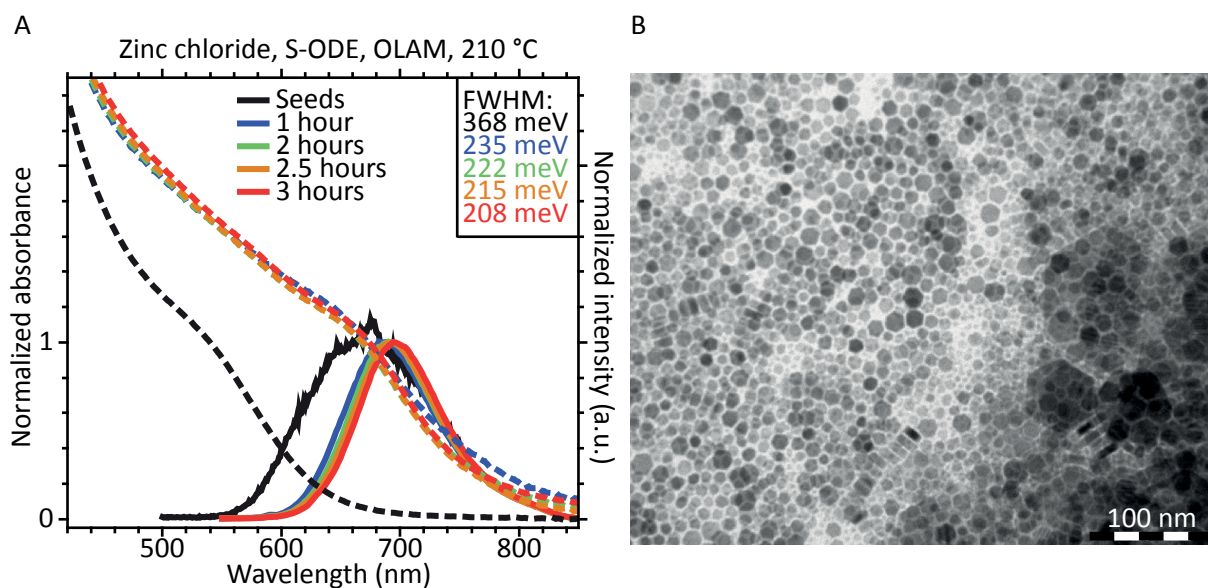


Figure 4.10. A: Absorption (dashed lines) and emission (solid lines) of the CIS seeds and the resulting NCs after reaction with zinc chloride, S-ODE and OLAM at 210 °C. The absorption and emission spectra of the resulting sample shift to the red, indicating shell growth. The FWHM decreases. B: TEM picture of the corresponding NCs.

sample with large hexagonal crystals (diameter (11.5 ± 2.3) nm) but the smallest crystals with a 8 nm diameter are not present. Furthermore, a decrease in the FWHM of the core/shell emission peak with respect to the parent CIS emission peak is observed. This is another key observation concerning the nature of the emitting state of CIS/ZnS NCs and the change herein compared to the parent CIS NCs. Normally, the FWHM is a measure for the size dispersion of the ensemble, which will not become narrower after shell growth. Especially in this sample where the size dispersion is large, the narrowing of the FWHM of the emission peak is an indication that the nature of the emitting state changed upon shell growth.

E. Speculations on the nature of the emitting states

Speculating on an explanation for the observations described above, the large increase in size can be due to clustering of the CIS NCs, followed by growth of a zinc sulfide shell around these clusters. This clustering can be caused by the combination of OLAM and chloride ions present in the solution, which can lead to a structural transformation as is shown for small CdS seeds that change to large hexagonal CdSe platelets by Surayama *et al.*¹¹ When the CIS NCs become larger due to clustering subsequently the band gap will become smaller and thus both the absorption and the emission spectra will shift to the red, with respect to the smaller CIS NCs. Speculating further, when the cores of the CIS/ZnS core/shell NCs are indeed larger and give rise to an absorption band and emission peak at lower energy, the decreased global Stokes shift that is observed for the CIS/ZnS is due to a shift of the emission peak to the blue, closer to the peak in the absorption band. This can only be caused by a change in the nature of the emitting states, since shell growth alone cannot lead to an increase in the band gap (see Figure 2.6A). The change in the nature of the emitting state is then expected to be the change from the trap-assisted or donor-acceptor recombination in the CIS NCs, as proposed for bulk CIS crystals by Ueng *et al.*¹² and Lewerenz *et al.*,¹³ to the band-edge recombination in the CIS/ZnS core/shell NCs. This

reasoning can explain the possible blue shift of the emission peak, the decrease in global Stokes shift and the narrowing of the FWHM of the emission peak. The latter is due to the constant energy levels of the band edges, while the small fluctuations in energy of trap states leads to a broader emission band.

F. Drop wise addition method

To get better control over the growth of the zinc sulfide shell, another synthesis approach was used. In the drop wise addition method, described in detail in the ‘experiment’ section, the zinc precursor was added dropwise and in small portions to the heated CIS NCs. The absorption and emission spectra of the resulting sample show a large red shift (534 meV, Figure 4.11) and not the large decrease in global Stokes shift as described above. The resulting NCs were analyzed with TEM and EDS as well, showing completely different shapes (Figure 4.11C and D) with a length of (11.7 ± 2.3) nm. These shapes suggest that Ostwald ripening took place and since the EDS atomic ratios (Figure 4.11B, Table 4.4) show only very small amounts of zinc present, the large red shift is probably due to the larger size of the CIS NCs and not shell formation. After 1.5 month storage under inert atmosphere, the particles did not show lu-

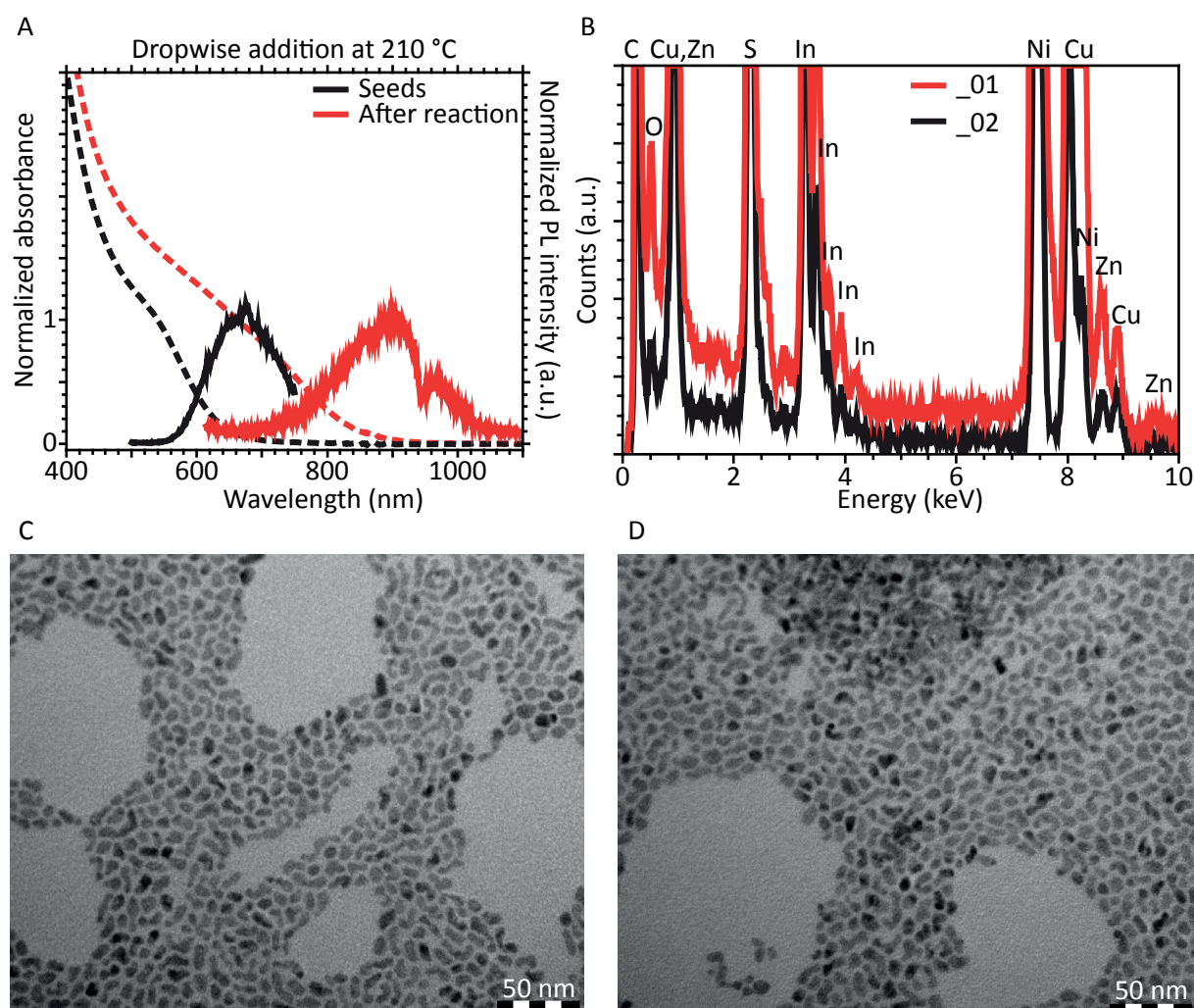


Figure 4.11. A: Absorption (dashed lines) and emission (solid lines) of the CIS seeds and the resulting NCs after dropwise addition of zinc chloride and ODA to a mixture of the NC seeds, S-ODE and OLAM at 210 °C. The absorption and emission spectra of the resulting sample shift to the red. B: EDS spectra of two measurements at different locations on the TEM grid. C and D: TEM pictures of the NCs after the drop wise addition reaction.

Table 4.4. Elemental ratio in the NCs obtained after drop wise addition of zinc chloride at 210 °C. Two measurements at different locations on the TEM grid were performed.

	_01	_02
	Atomic%	Atomic%
S	49.943	50.864
Cu	25.524	24.393
Zn	4.15	2.86
In	20.382	21.881
S:Cu	1.96	2.09
Cu	1	1
Zn:Cu	0.16	0.12
In:Cu	0.78	0.90
	$\text{Cu}_{1.0}\text{In}_{0.8}\text{S}_{1.8}/\text{Zn}_{0.2}\text{S}_{0.2}$	$\text{Cu}_{1.0}\text{In}_{0.9}\text{S}_{2.0}/\text{Zn}_{0.1}\text{S}_{0.1}$

minescence anymore, which is a clear indication of their instability. They might have grown even larger, reconstructions lead to more trap states that facilitate non-radiative recombination. All in all indicate these results no zinc sulfide shell was formed and only clustering took place.

G. Crystal structures

To study the shell formation in more detail, HRTEM and electron diffraction measurements were performed of the sample with large hexagonal structures. The resulting pictures and Fast-Fourier-Transforms are shown in Appendix F. Since the obtained lattice parameters can be compatible with many structures and there is no supporting X-ray diffraction information, there is no unambiguous conclusion on the crystal structure of these NCs and more extensive analysis is required.

4.3.4. Exciton lifetimes

To learn more about the origin of emission of the CIS and CIZS cores and core/shell HNCs, lifetime measurements were performed. The decay curves with bi-exponential fit are shown in Figure 4.12, the resulting lifetimes in Table 4.5 and the results of the more detailed time-resolved emission map measurements on CIZS and CIZS/ZnS are shown in Figure 4.13. The results are reviewed in the context of the in chapter 3 discussed model of Ueng *et al.*¹² that states that the luminescence in CIS originates from donor-acceptor recombination. This also means that w_{trap} has to be faster than w_{rad} .

A. CIS/CdS

When the lifetimes of the CIS/CdS HNCs are compared to the normal CIS cores, a large increase is observed for the fast component as well as the slow component. In the decay curve (Figure 4.12A) the long lifetime is clearly visible, the fastest decay component of several ns is no longer observed and the bi-exponential fits the decay curve very well. These observations supports the earlier statement (in the theory chapter and section 4.3.2 on page 35) that a CIS/CdS HNC has a type II band alignment: the

electron and hole are spatially separated and recombination takes long. This indicates that the large global Stokes shift that is observed for CIS/CdS HNCs has a different origin than the shift observed for the CIS NCs. The first originates from the indirect band gap resulting from the Type II carrier localization regime, the latter from the energy difference between the band edge and the trap energy level and the less overlapping wave functions. The emission observed for the CIS/CdS HNCs is therefore expected to originate from band edge recombination. This however does not mean that the trap states are not present anymore, only that w_{trap} is too slow in comparison with the delocalization rate of the electron through the shell material.

B. CIS and CIZS

When the lifetimes of normal CIS and the most blue shifted CIZS are compared, the lifetimes of CIZS are longer, especially when looking at comparable wavelengths (τ_1 at 615 nm for CIS is 16 ns, τ_2 137 ns, at 630 nm τ_1 is 48 ns for CIZS and τ_2 is 351). This is a different result than reported earlier for CIZS^{4,7}

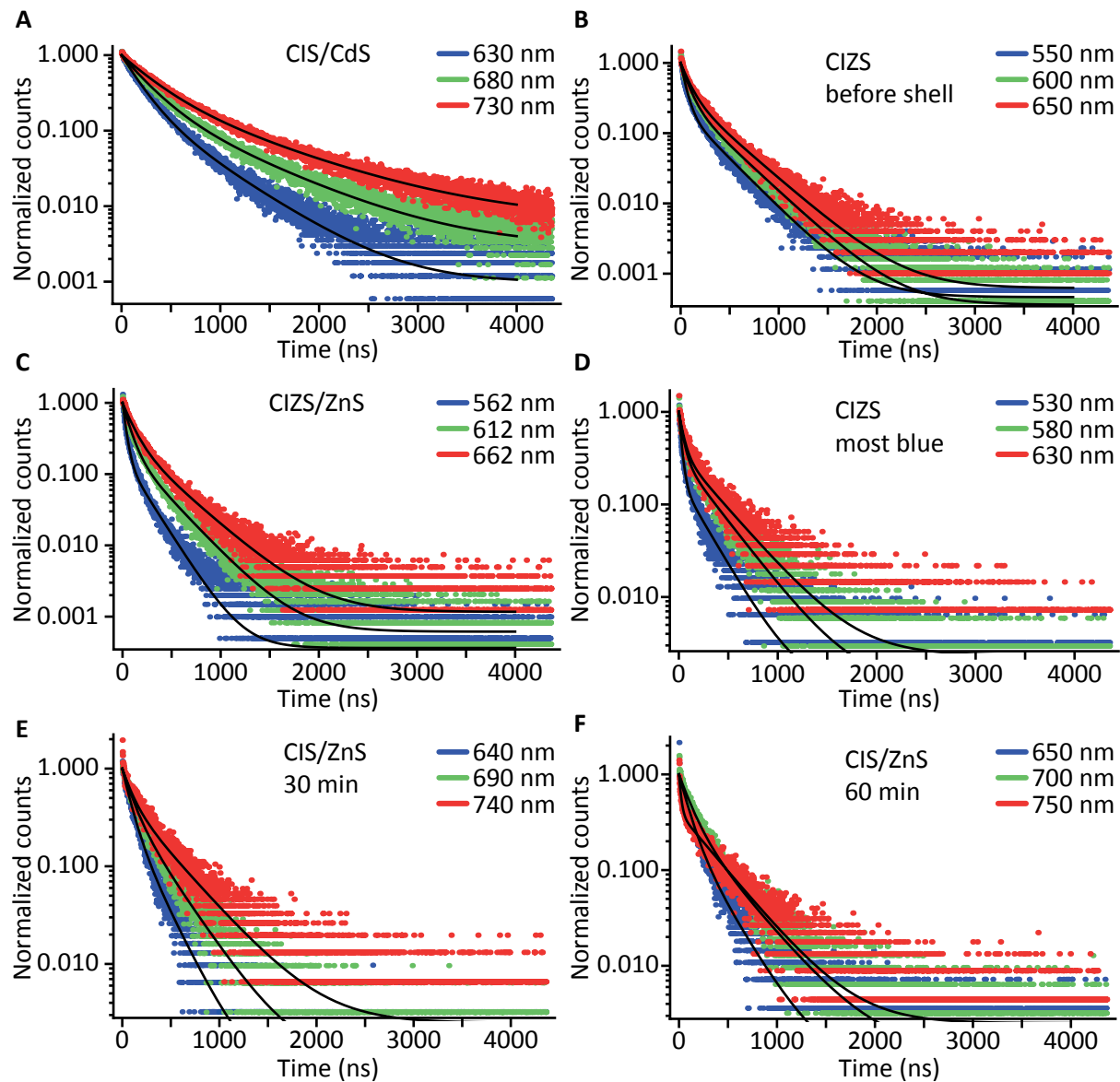


Figure 4.12. Decay curves measured at three positions within the emission peak and fitted bi-exponentially for A: CIS/CdS core/shell HNCs, B: CIZS NCs, C: CIZS/ZnS HNCs, D: most alloyed CIZS NCs, E: CIS/ZnS HNCs, F: CIS/ZnS HNCs.

Table 4.5. Lifetimes obtained from a bi-exponential fit of decay curves of different samples discussed in this chapter

Sample	Wavelength blue side (nm)	Wavelength middle (nm)	Wavelength red side (nm)
Normal CIS	615	675	715
τ_1 (ns)	16	26	34
τ_2 (ns)	137	206	257
CIS/CdS	630	680	730
τ_1 (ns)	175	240	301
τ_2 (ns)	508	735	908
CIZS before shell	550	600	650
τ_1 (ns)	52	79	90
τ_2 (ns)	307	333	357
CIZS/ZnS	562	612	662
τ_1 (ns)	34	73	101
τ_2 (ns)	199	296	356
Most blue CIZS	530	580	630
τ_1 (ns)	27	45	48
τ_2 (ns)	235	311	351
CIS/ZnS 30 min reaction	640	690	740
τ_1 (ns)	81	98	96
τ_2 (ns)	216	296	386
CIS/ZnS 60 min reaction	650	700	750
τ_1 (ns)	93	119	21
τ_2 (ns)	257	360	353

which can be due to differences in stoichiometry that can lead to differences in band edge energy levels and amount of trap states.^{14,15} The increase in lifetime observed here and the increased luminescence efficiency (section 4.3.3 on page 36), suggest a decrease of fast non-radiative decay ($w_{\text{trap-non-rad}}$), implying that alloying with zinc removes (defect related) trap states. Since the large global Stokes Shift is observed for both CIZS NCs and the parent CIS NCs (Figure 4.1) and, according to the shape of the decay curve and the band bi-exponential fit (Figure 4.12B,D and Figure 3.8), the number of decay channels is not changed, there is no reason to assume a change in the origin of the emission.

C. CIZS and CIZS/ZnS

When the lifetimes of the CIZS NCs are compared to CIZS/ZnS HNCs, the values are very similar, although a little bit shorter on the blue side for the CIZS/ZnS HNCs, suggesting that the exciton is more confined in these NCs, resulting in strong wave function overlap and thus fast decay. The shape of the decay curves is very similar, suggesting that the number of decay channels did not change and the large global Stokes shift is observed for both the CIZS NCs and CIZS/ZnS HNCs. These similarities suggest that no large changes in the nature of the emitting states occurred.

D. CIS/ZnS

For the CIS/ZnS HNCs a type I or type 1½ band alignment is expected, regarding the only small offset between the both CB edges (0.55 eV).^{16,17} The increase in lifetimes that is observed, can be explained by the less overlap of the wave functions resulting from a type 1½ band alignment or by a change in the origin of the emission, as discussed above. When the emission after shell growth originates from band edge recombination instead of the trap-assisted radiative recombination, the lifetime will increase as well, since w_{rad} is slower than w_{trap} .

E. A closer look on CIZS and CIZS/ZnS

A more detailed analysis of the decay curves of the most blue shifted CIZS NCs and the CIZS/ZnS HNC is shown in Figure 4.13. The bi-exponential fit of the decay curve again shows not to be ideal, which is clear from the plots in Figure 4.13A and B as well from the misplaced τ_1 and τ_2 lines in the Figure 4.13 C-F. These observations lead to the conclusion that the electronic structure of the CIS is not changed significantly when zinc is added to the crystal. The growth of the ZnS shell also does not influence the linear dependence of the lifetime on the energy (Figure 4.13D and F). This observation does not support the trap-hopping mechanism proposed by Hamanaka *et al.*¹⁸ since the surface related traps are supposed to be disappeared after shell growth.

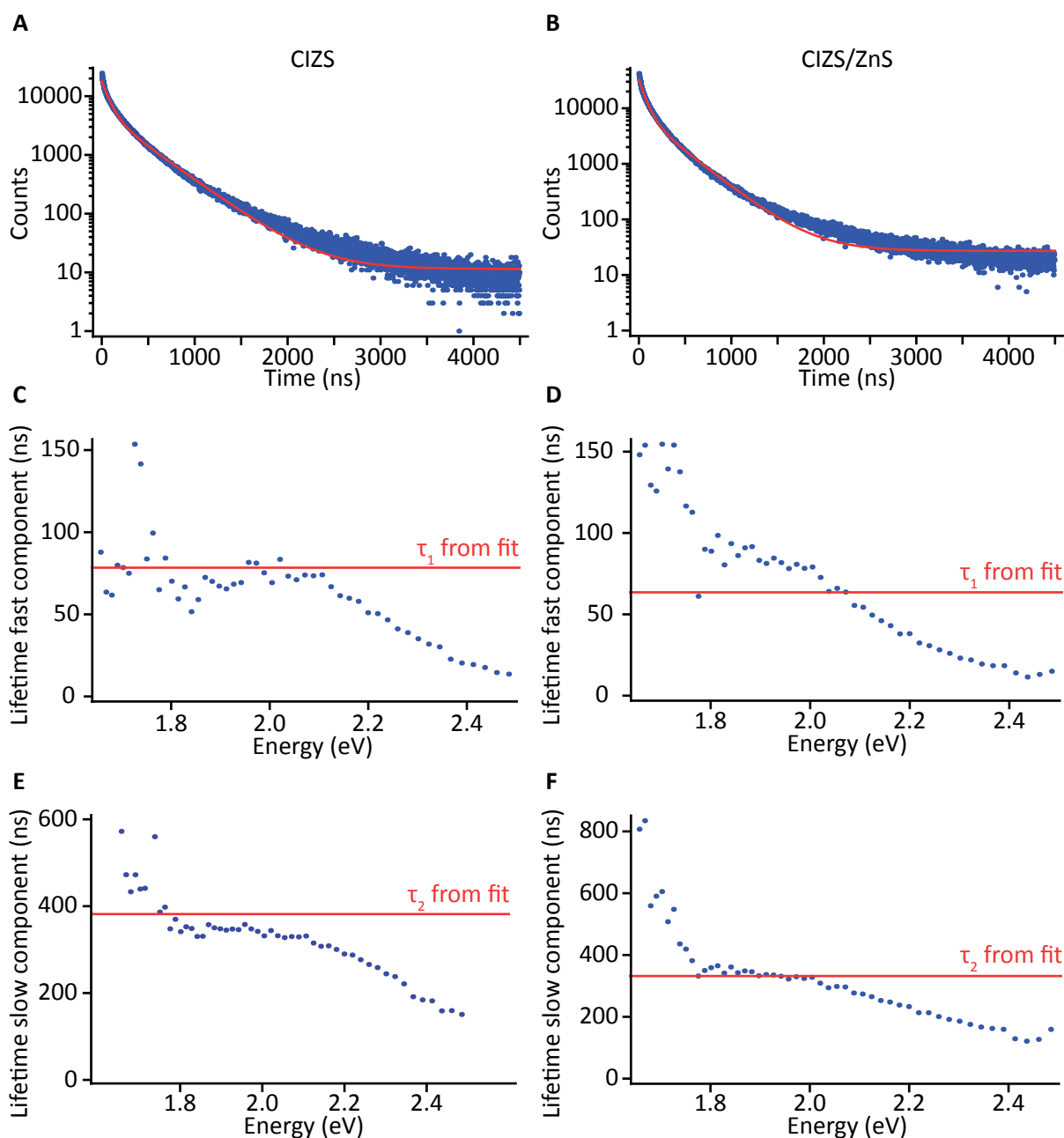


Figure 4.13. Time-resolved emission map measurements of CIZS and CIZS/ZnS NCs. A: Total decay curve of the CIZS NCs with a bi-exponential fit. B: Total decay curve of the CIZS/ZnS HNCs with a bi-exponential fit. C: Plot of the lifetime of the fast component as function of energy in the CIZS NCs. D: Plot of the lifetime of the fast component as function of energy in the CIZS/ZnS HNCs. E: Plot of the lifetime of the slow component as function of energy in the CIZS NCs. F: Plot of the lifetime of the slow component as function of energy in the CIZS-ZnS HNCs.

4.4. Conclusion & outlook

In the attempt to grow a zinc sulfide shell around a CIS core a tough competition between alloying/cation exchange and hetero epitaxial growth of the shell was encountered. Only with very reactive precursors (S-ODE and ZnCl_2) and at a high temperature (210 °C) a shell was grown, but with little control of the size and shape of the resulting NCs, that show a remarkable large sizes and hexagonal shapes. HRTEM and electron energy loss microscopy (EELS) should give more insight into this phenomenon. Less reactive precursors (such as DDT and zinc stearate) yield alloyed CIZS NCs, and a mixture (ZnCl_2 and

DDT) yields CIZS/ZnS. EDS measurements suggest an exchange of indium for zinc and this observation cannot be explained yet. The emission wavelength shifting and the lifetime measurements confirm the theoretical band offsets shown in Figure 2.6B, yielding a type II band alignment for CIS/CdS (red shift, increased (global) Stokes shift, longer lifetimes) and a type I½ band alignment for CIZS/ZnS (red shift, higher efficiency). For CIS/ZnS a type I or type I½ band alignment was expected, but due to the remarkable decrease in global Stokes shift observed for this sample that cannot be convincingly explained yet, we cannot be conclusive on this matter. The strongly decreased Stokes shift and decreasing FWHM for the CIS/ZnS HNCs might be a result of removing surface trap states, leading to band edge emission as origin of the emission in these core/shell NCs.

Although some remarkable and clear results regarding changes in the (global) Stokes shift and FWHM for the CIS/ZnS HNCs and the large increase of the lifetimes for the CIS/CdS crystals, the proposed explanations and remarks made on the origin of the emission are still very speculative and uncertain. More detailed lifetime measurements and analysis, for example at low temperatures, should provide more insight in this matter. With the recent new equipment available, it is possible to measure lifetimes at wavelengths above 750 nm. These measurements certainly have to be performed. Finally, synthesis and analysis of CIZS/CdS HNCs may provide the missing pieces of information to complete the puzzle of the electronic structure and origin of the emission of CIS and its derivatives.

Some more research in the lab is necessary as well, to search the right reaction conditions to obtain only CIS/ZnS HNCs instead of a CIZS-CIS/ZnS mixture. The drop wise addition synthesis so far did not give the desired results, so more variations in temperature and addition order can be made. The hot injection synthesis with better adjusted precursor amounts could also be worth a try. A synthesis with zinc stearate and S-ODE at high temperature was not performed yet but would be nice to complete the picture and maybe give some insight into the role of chloride ions.

4.5. References

1. De Mello Donegá, C. Synthesis and properties of colloidal heteronanocrystals. *Chem. Soc. Rev.* **40**, 1512–46 (2011).
2. Kim, Y.-K., Ahn, S.-H., Chung, K., Cho, Y.-S. & Choi, C.-J. The photoluminescence of CuInS₂ nanocrystals: effect of non-stoichiometry and surface modification. *J. Mater. Chem.* **22**, 1516 (2012).
3. Li, L. et al. Efficient Synthesis of Highly Luminescent Copper Indium Sulfide-Based Core/Shell Nanocrystals with Surprisingly Long-Lived Emission. *J. Am. Chem. Soc.* **133**, 1176–1179 (2011).
4. Trizio, L. De et al. Strongly Fluorescent Quaternary Cu – In – Zn – S Nanocrystals Prepared from Cu_{1-x}In_{2x} Nanocrystals by Partial Cation Exchange. *Chem. Mater.* **24**, 2400–2406 (2012).
5. Feng, J., Sun, M., Yang, F. & Yang, X. A facile approach to synthesize high-quality Zn(x)Cu(y)In-S(1.5+x+0.5y) nanocrystal emitters. *Chem. Commun. (Camb)*. **47**, 6422–6424 (2011).
6. Komarala, V. K., Xie, C., Wang, Y., Xu, J. & Xiao, M. Time-resolved photoluminescence properties of CuInS₂/ZnS nanocrystals: Influence of intrinsic defects and external impurities. *J. Appl. Phys.* **111**, 124314 (2012).
7. Seo, J. et al. Time-resolved and temperature-dependent photoluminescence of ternary and quaternary nanocrystals of CuInS₂ with ZnS capping and cation exchange. *J. Appl. Phys.* **114**, 094310 (2013).
8. Lu, X., Zhuang, Z., Peng, Q. & Li, Y. Controlled synthesis of wurtzite CuInS₂ nanocrystals and their side-by-side nanorod assemblies. *CrystEngComm* **13**, 4039 (2011).
9. Huang, L. et al. Cadmium and Zinc Alloyed Cu-In-S Nanocrystals and Their Optical Properties. *J. Nanopart. Res.* **15**, (2013).
10. Hoa, T. T. Q., Vu, L. Van, Canh, T. D. & Long, N. N. Preparation of ZnS nanoparticles by hydrothermal method. *J. Phys. Conf. Ser.* **187**, 012081 (2009).
11. Saruyama, M., Kanehara, M. & Teranishi, T. Drastic structural transformation of cadmium chalcogenide nanoparticles using chloride ions and surfactants. *J. Am. Chem. Soc.* **132**, 3280–2 (2010).
12. Ueng, H. Y. & Hwang, H. . The defect structure of CuInS₂. Part I: intrinsic defects. *J. Phys. Chem. Solids* **50**, 1297–1305 (1989).
13. Lewerenz, H. J. & Dietz, N. Defect identification in semiconductors by Brewster angle spectroscopy. *J. Appl. Phys.* **73**, 4975–4987 (1993).
14. Uehara, M., Watanabe, K., Tajiri, Y., Nakamura, H. & Maeda, H. Synthesis of CuInS₂ fluorescent nanocrystals and enhancement of fluorescence by controlling crystal defect. *J. Chem. Phys.* **129**, 134709 (2008).
15. Chen, B. et al. Highly Emissive and Color-Tunable CuInS₂-Based Colloidal Semiconductor Nanocrystals: Off-Stoichiometry Effects and Improved Electroluminescence Performance. *Adv. Funct. Mater.* **22**, 2081–2088 (2012).
16. Hunger, R., Pettenkofer, C. & Scheer, R. Dipole formation and band alignment at the Si(111)/CuInS₂ heterojunction. *J. Appl. Phys.* **91**, 6560 (2002).
17. Van de Walle, C. G. & Neugebauer, J. Universal alignment of hydrogen levels in semiconductors, insulators and solutions. *Nature* **423**, 626–8 (2003).

18. Hamanaka, Y. et al. Defect-induced photoluminescence and third-order nonlinear optical response of chemically synthesized chalcopyrite CuInS₂ nanoparticles. *Chem. Phys. Lett.* **466**, 176–180 (2008).

5. Synthesis of CuInS₂ nanocrystals by partial cation exchange in Cu_{2-x}S nanocrystals

5.1. Introduction

Nanocrystals are usually prepared by a direct synthesis method, in which size and shape control is realized by adjusting the synthesis conditions (precursors, reaction time and temperature). For ternary or quaternary NCs this is more difficult, because the different precursor reactivities have to be very similar to obtain pure-phase NCs.¹ In the case of CIS nanocrystals this means that formation of Cu_{2-x}S NCs is usually favored when the reaction conditions are not adjusted well enough.^{2,3} This currently means that luminescent colloidal CIS NCs only exist in quasi-spherical shapes.⁴

In the cation exchange method cations from the seed NC are (partially) replaced by others. Remarkably the anionic sublattice is usually preserved when exchanging the cations.⁵ This makes it potentially possible to obtain morphologies which cannot (yet) be obtained by direct synthesis. Copper sulfide NCs are a suitable starting material for CIS, since the material is non-toxic and a gamut of NC shapes is easy to synthesize.⁶⁻⁸ Furthermore, the crystal structure of Cu_{2-x}S is very similar to the crystal structure of CIS.⁴

In this chapter, a novel method to synthesize colloidal CIS nanocrystals by partial cation exchange in Cu_{2-x}S nanocrystals is described. In order to acquire control over the In³⁺ for Cu⁺ exchange process, the influence of a number of variables (i.e. indium precursor, temperature and parent NC size) was investigated in detail.

5.2. Experimental

5.2.1. Materials

Triocetylphosphine oxide (TOPO, Sigma Aldrich, tech. 90%), Copper (I) acetate (Sigma Aldrich, 97%), Copper (II) acetylacetonate (Sigma Aldrich, 99.99+%), 1-octadecene (ODE, Sigma Aldrich, tech. 90%), 1-dodecanethiol (DDT, Sigma Aldrich, ≥98%), Toluene (Sigma Aldrich, 99.8%), Methanol (Sigma Aldrich, 99.8%), 1-Butanol (Sigma Aldrich, 99.8%), Indium (III) acetate (Sigma Aldrich, 99.99%), Indium (III) chloride (Sigma Aldrich, 99.999%), Indium (III) nitrate hydrate (Sigma Aldrich, 99.99%), Oleic Acid (Oleic acid (OA, Sigma Aldrich, 90%), Oleylamine (OLAM, Sigma Aldrich, tech. 70%), Trioctylphosphine (TOP, Fisher Scientific)

ODE and OLAM were degassed for 2 hours at 150-200 °C before usage.

5.2.2. Synthesis

The copper sulfide seeds were synthesized by dissolving 0.88 mmol copper (I) acetate and 2.2 g TOPO in 50 mL ODE and degassing this mixture for 30 minutes at 100 °C. It was then heated under nitrogen flow to 160 °C and 2 mL DDT was injected. The temperature was then raised to 180 °C and the mixture reacted 3.5 hours at this temperature. Then the mixture was cooled to room temperature and washed with methanol/butanol.

In another protocol of Tang *et al.*⁸ 3 mmol Cu(acac)₂, 5 mL DDT and 25 mL OLAM were mixed and heated to 200 °C for 20 minutes. Then the mixture was cooled to room temperature (RT) and washed with methanol/butanol.

In the cation exchange reactions at elevated temperatures (50-200 °C) an excess of indium precursor (0.35 mmol, In(NO₃)₃, In(Ac)₃ or InCl₃) was dissolved in 2 mL ODE and mixed with the copper sulfide seeds dispersed in toluene. Sometimes extra ligands (0.5-3 mL, OLAM, OA, TOP) were added and the mixture was then stirred for 1-5 hours. Then the NCs were washed with methanol/butanol or acetone and redispersed in toluene.

In the cation exchange reactions at room temperature (RT) an excess of indium precursor (0.1 mmol, In(NO₃)₃, In(Ac)₃ or InCl₃) was dissolved in methanol and mixed with the copper sulfide seeds dispersed in toluene and 100 μL TOP was added. The mixture was then stirred for 5-7 days, after which the reaction was quenched by washing the NCs with methanol/butanol or acetone and redispersed in toluene.

A detailed overview of the exact conditions used is given in Appendix G.

5.2.3. Characterization

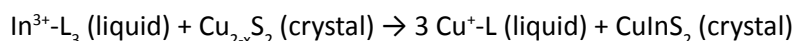
Absorption spectra were recorded with a Perkin Elmer Lambda 950 UV/VIS/NIR spectrophotometer. Fluorescence measurements were performed with an Edinburgh Instruments FLS920 fluorescence spectrophotometer equipped with a 450 W Xe lamp and double excitation monochromator with a grating blazed at 300 nm. Spectra were recorded with a Hamamatsu R928 PMT detector with a grating blazed at 500. For lifetime measurements excitation was carried out with an Edinburgh Instruments EPL445 picosecond pulsed diode laser at 441.1 nm and a pulse width of 80.2 ps and spectra were recorded with a Hamamatsu photosensor module H10720-01. Lifetimes were obtained from a bi-exponential fit of the tail of the decay curve. Transmission electron microscopy (TEM) images were taken with a Philips Tecnai Scripting microscope (FEI company), with an accelerating voltage of 100 or 120 kV. Energy dispersive X-ray spectroscopy (EDS) measurements were performed with a FEI Tecnai-20F microscope equipped with a Field Emission Gun, a Gatan 694 CCD camera and an EDA spectrometer. The microscope was operated at 200 kV. Acquisition time for the EDS measurements was 30 s. From samples with small particles large areas (containing approximately 10⁴-10⁵ NCs) were measured to

obtain reasonable valid data. X-ray diffraction (XRD) measurements were performed with a Philips PW 1729/40 X-ray generator operated at 40 kV and 20 mA. A Philips PW 1820/00 sample chamber was used and a Philips PW 3710/00 detector. The NCs were brought onto a crystalline silicon wafer and dried to air before measuring. The XRD references are taken from the International Centre for Diffraction Data (ICDD). The diffractogram used for the Cu_{2-x}S djurleite crystal structure is number 00-046-1195, for the CIS wurtzite structure this is 04-016-2016.

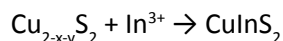
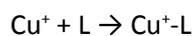
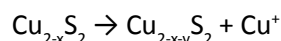
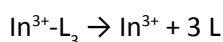
5.3. Results & discussion

When Cu_{2-x}S NCs are converted to CIS, a clear change in the absorption spectra and, depending on their size, emission spectra is observed. Therefore, the In^{3+} for Cu^+ exchange in Cu_{2-x}S NCs was followed mainly by optical spectroscopy. TEM was also used to analyze the final samples but was not conclusive for nanocrystals smaller than 5 nm due to the limited resolution of the instrument used.

The overall partial cation exchange reaction from Cu_{2-x}S to CIS can be described as follows:¹²



where $\text{In}^{3+}\text{-L}_3$ (liquid) is the indium precursor in solution and L is a ligand. This total reaction can be divided into elemental steps:¹²



Important in a cation exchange reaction is the balance between the diffusion out of the crystal (in this case Cu^+) and the diffusion into the crystal (in this case In^{3+}). When these diffusion rates out of the crystal is higher, the crystal will destabilize and dissolve. Many thermodynamic and kinetic factors, such as stability of the reactant and product phases, cation solvation and ligation, and the role of ligands and their binding energy to the different cations, play an important but not yet well understood role herein.^{9,13}

5.3.1. 13-15 nanometer sized nanocrystals at elevated temperatures

A. Temperature

To observe the influence of temperature on the cation exchange, a reaction with increasing temperatures (RT to 100 °C) was performed and samples were taken every hour. Spherical Cu_{2-x}S NCs with a diameter of (13.5 ± 1.4) nm were used as starting material. The development of the absorption spectra is shown in Figure 5.1A and TEM pictures are shown in Figure 5.1B-E. A significant change in absorption is observed. The parent Cu_{2-x}S NCs show a peak at 360 nm, which is ascribed to Cu-DDT complexes that form a viscous gel and were not washed away, and over time a broad band becomes visible around 480 nm. This suggests that partial exchange has occurred. However, CIS NCs with a diameter of 13 nm would give rise to an absorption band at longer wavelengths, which means that stoichiometric CIS was not formed (yet). The diameter of the different resulting samples is comparable with the parent NCs.

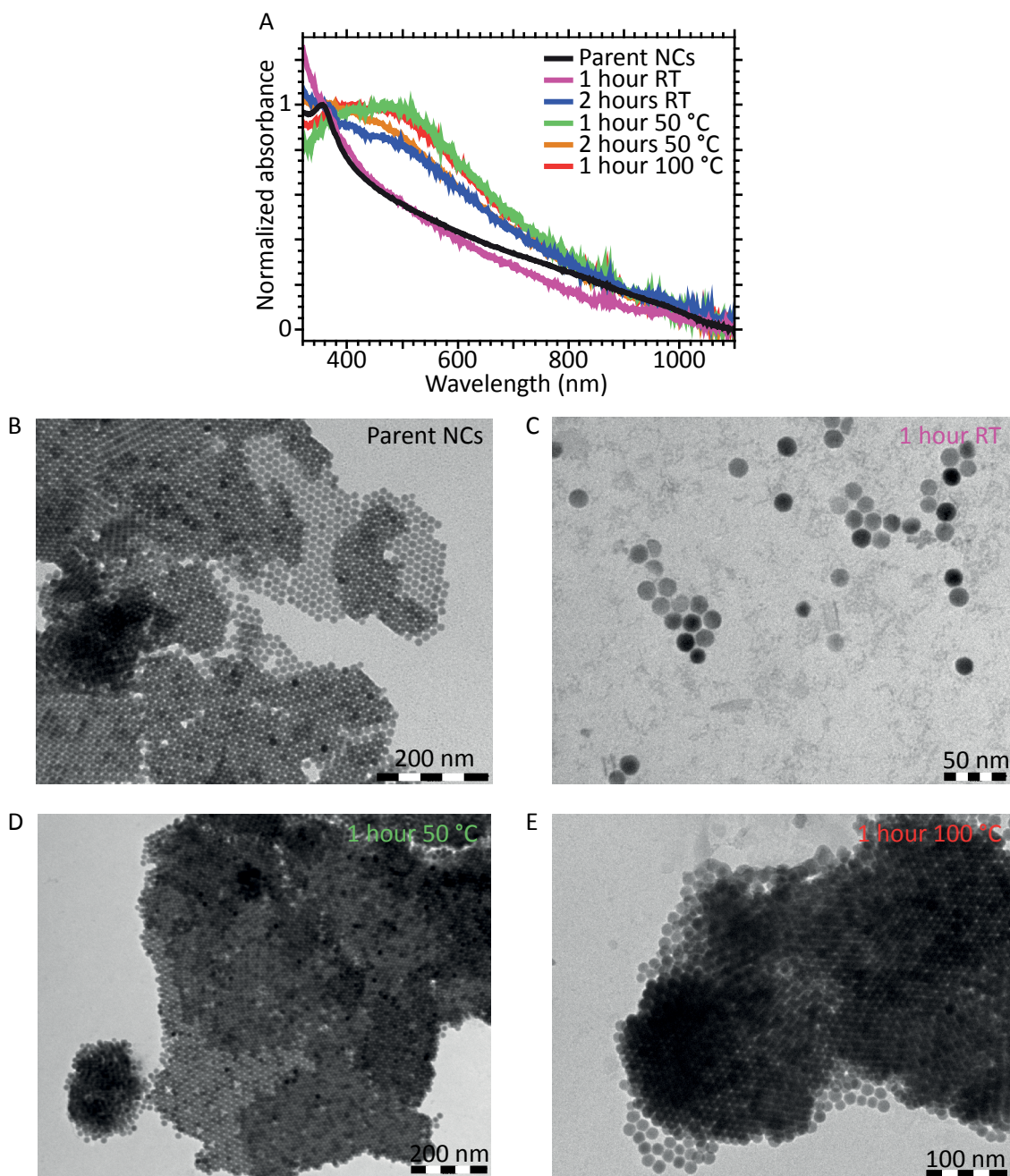


Figure 5.1. A: Absorption spectra of the parent NCs and the samples taken at different times during the reaction. B: TEM picture of parent NCs. C: TEM picture of sample after 1 hour reaction at room temperature. D: TEM picture of sample after 2 hour reaction at room temperature and 1 hour at 50 °C. E: TEM picture of sample after 2 hours reaction at room temperature, 2 hours reaction at 50 °C and 1 hour at 100 °C.

The diameter of the first sample was (14.7 ± 1.2) nm, for the third sample (15.3 ± 1.3) nm was measured and for the last sample (15.3 ± 0.9) nm. This implies that the anionic framework is preserved, and therefore that only minor changes in anionic sublattice parameters took place.^{5,9,13} The self-assembly characteristics of the parent Cu_{2-x}S NCs are preserved, which is remarkable, since the surface must be affected by the difference in composition.

The reaction was performed at higher temperatures (100-200 °C), using the same concentrations of chemicals but slightly larger Cu_{2-x}S NCs (17.1 ± 1.5 nm diameter). Every hour a sample was taken and

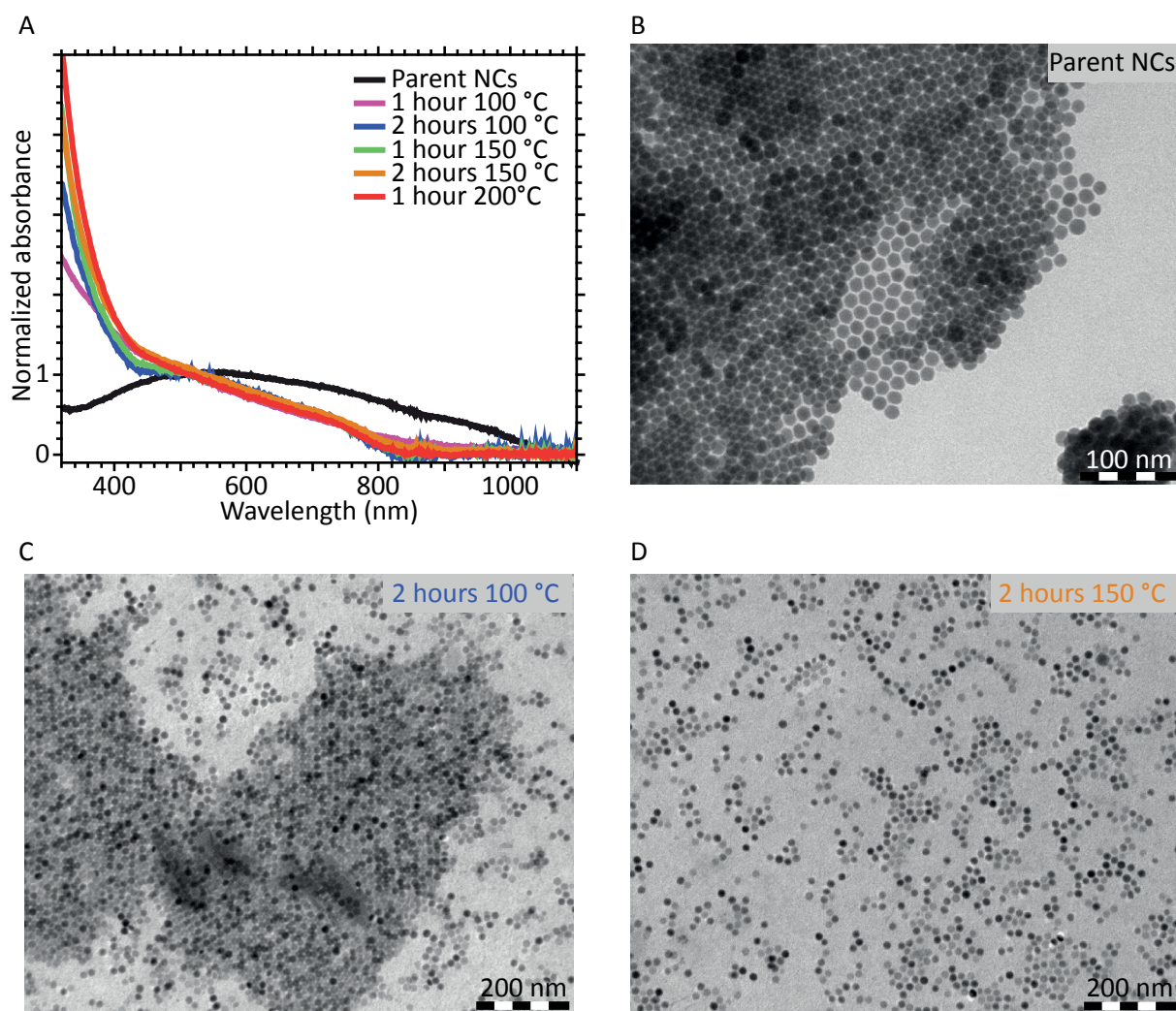


Figure 5.2. A: A: Absorption spectra of the parent NCs and the samples taken at different times during the reaction. B: TEM picture of parent NCs. C: TEM picture of sample after 2 hours reaction at 100 °C. D: TEM picture of sample after 2 hours reaction at 100 °C and 2 hours at 150 °C.

the absorption spectra and TEM pictures of the resulting samples are shown in Figure 5.2. The characteristic CIS absorption band (Figure 5.2A) is observed already after 1 hour reaction at 100 °C and remains at the same position during the rest of the reaction. The TEM pictures (Figure 5.2B-D) show that the size of the NCs did not change (16.5 ± 1.5 nm for the NCs after 2 hours at 150 °C), but the NCs no longer self-assemble. This is probably due to the difference in surface composition

B. Ligands

To stimulate the incorporation of indium, in one synthesis oleic acid was used instead of oleylamine. Cu_{2-x}S NCs with a diameter of (17.1 ± 1.5) nm were used and after 1 hour reaction at 100 °C the NCs were dissolved. The dissolution of the Cu_{2-x}S NCs shows clearly an imbalance between the diffusion of Cu^+ and In^{3+} . Since TOP binds strongly to copper ions, these are extracted from the Cu_{2-x}S NCs. OA apparently binds strongly to the indium atoms, so they are prevented from going in and as a result the NCs dissolve.

5.3.2. 4 nanometer sized nanocrystals at elevated temperatures

Because small CIS NCs (within the quantum confinement regime) have interesting luminescent properties, the cation exchange reaction was also performed with smaller (4 nm diameter) Cu_{2-x}S NCs. Since small Cu_{2-x}S NCs are used that are less stable than NCs with diameters of more than 10 nm, TOP was no longer used as ligand, to prevent a too fast copper extraction while the indium incorporation is slow, resulting in dissolved NCs.

A. Indium precursor

The reactivity of different indium precursors in the exchange reaction was investigated using 6 nm diameter Cu_{2-x}S NCs, and a reaction temperature of 55-100 °C. The absorption spectra of the samples taken every hour using $\text{In}(\text{NO}_3)_3$ as precursor are shown in Figure 5.3A. No significant change in the absorption spectra nor luminescence was observed, suggesting that no reaction took place. The same reaction was carried out using $\text{In}(\text{Ac})_3$ as precursor and the absorption spectrum of the resulting sample is shown in Figure 5.3B. Virtually no peak is observed, suggesting the NCs dissolved. This is probably due to a too fast diffusion of copper out of the crystal and a too slow diffusion of indium in, resulting in a collapsing NC. As third indium precursor InCl_3 was used, which yielded a tough gel at temperatures below 150 °C. InCl_3 is a catalyst for many organic reactions,¹⁴ which in this case may have led to a reaction between the double bond and the amine group of oleylamine molecule, yielding a polymer that made further processing impracticable.

5.3.3. 3 nanometer sized nanocrystals at room temperature

Since the exchange reactions with small NCs at elevated temperatures did not yield CIS NCs and instead often resulted in dissolved NCs, a milder method at room temperature was developed. At room temperature the diffusion rate of copper is expected to be slower, thereby preventing collapsing of the NCs

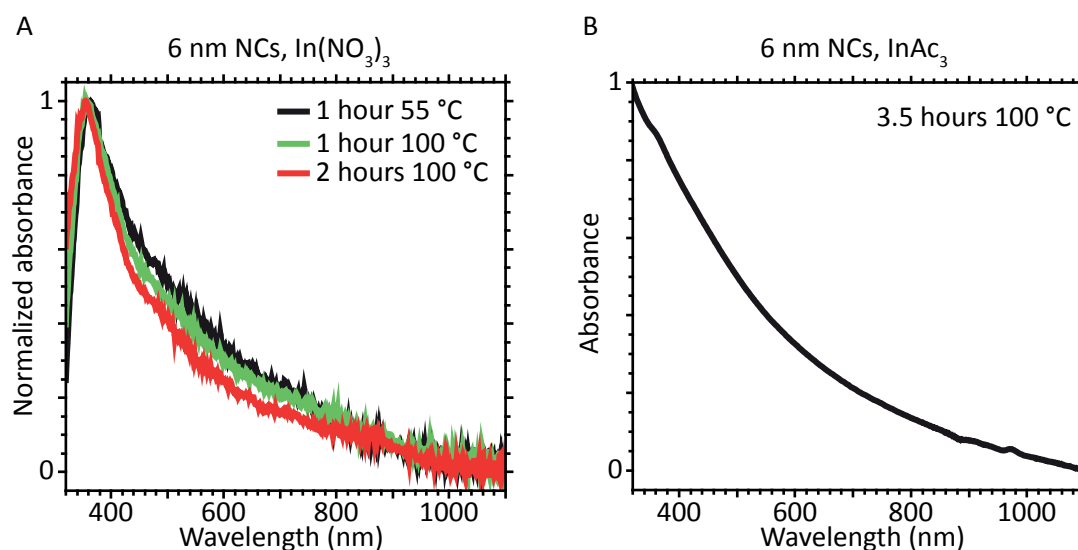


Figure 5.3. A: Absorption spectra of samples taken during a reaction with 6 nm Cu_{2-x}S NCs and indium nitrate as indium precursor. B: Absorption spectrum of material that remained after reaction with 6 nm Cu_{2-x}S NCs and indium acetate as indium precursor.

due to an exodus of Cu^+ ions.

A. Indium precursor

Indium nitrate as well as indium chloride were used as indium precursors. The absorption and emission spectra of the resulting samples are shown in Figure 5.4A and B for indium nitrate and C and D for indium chloride. In Figure 5.4A a clear emission peak is observed at 610 nm, in good agreement with the emission wavelength of 3 nm sized CIS NCs. In Figure 5.4C a small emission peak at 650 nm can be seen as well (indicated with the dashed line). In the absorption spectra no distinct peaks are observed. The emission peak at 820 nm which is cut-off by the detector limit, is observed in both emission spectra and is tentatively assigned to trap related emission, since it is at much lower energies than the peaks at 610 and 650 nm.

The luminescent CIS NCs obtained by cation exchange were also analyzed by TEM and EDS. Moreover,

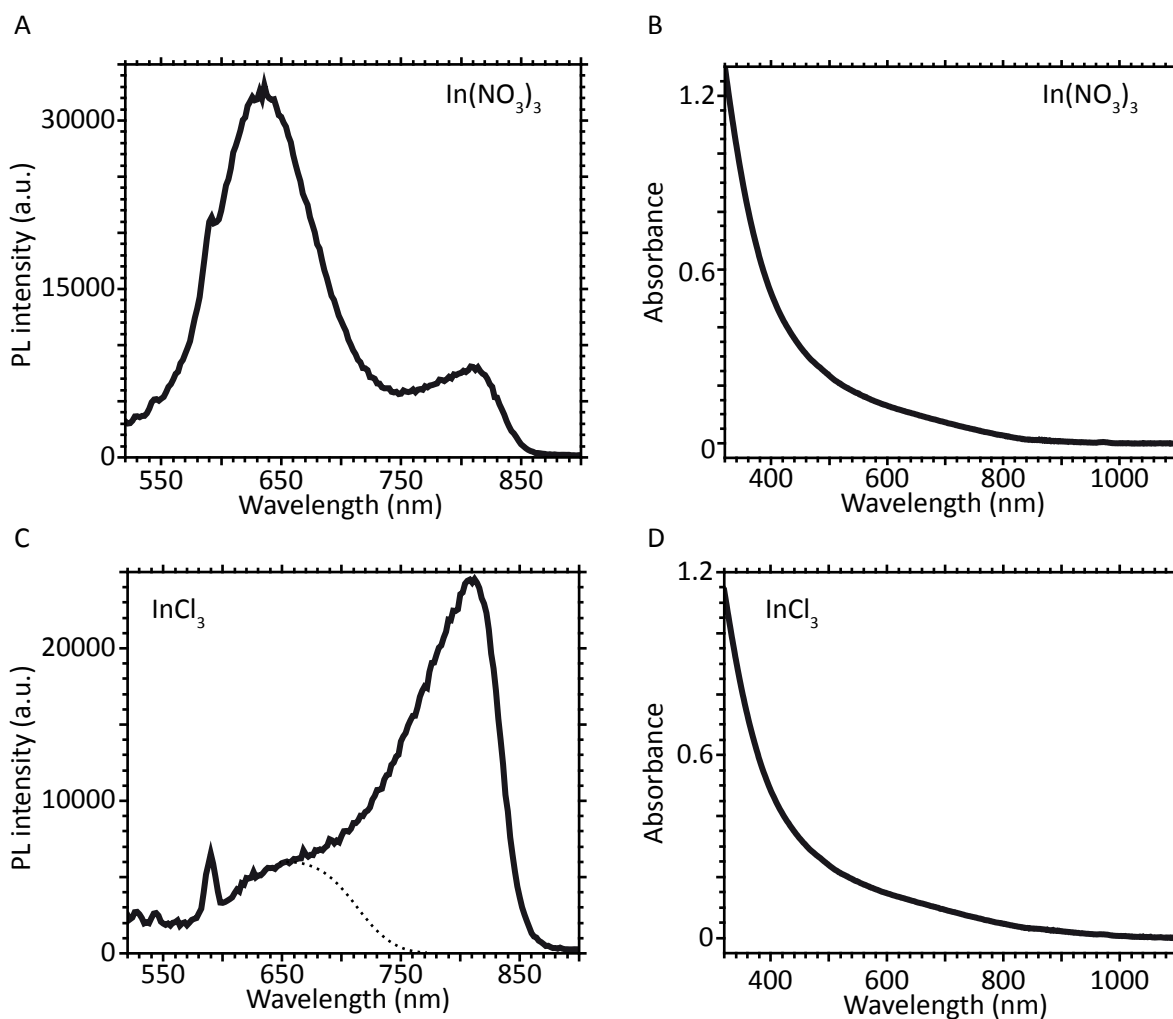


Figure 5.4. A: Emission spectrum of NCs obtained after a room temperature reaction for 7 days with 3 nm sized Cu_{2-x}S NCs and indium nitrate as indium precursor. B: Absorption spectrum of NCs obtained after a room temperature reaction for 7 days with 3 nm sized Cu_{2-x}S NCs and indium nitrate as indium precursor. C: Emission spectrum of NCs obtained after a room temperature reaction for 7 days with 3 nm sized Cu_{2-x}S NCs and indium chloride as indium precursor. D: Absorption spectrum of NCs obtained after a room temperature reaction for 7 days with 3 nm sized Cu_{2-x}S NCs and indium chloride as indium precursor.

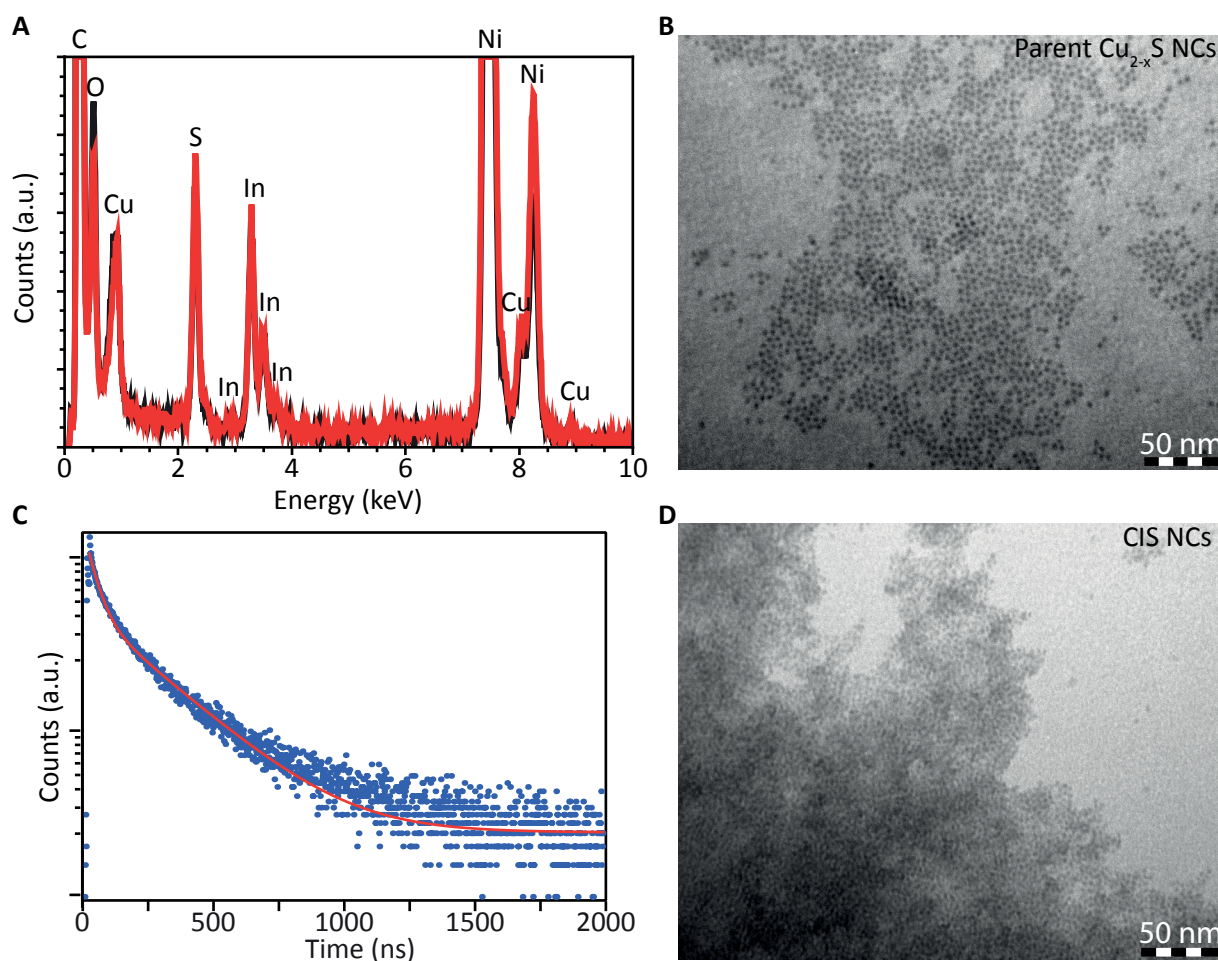


Figure 5.5. A: EDS spectra of luminescent NCs, obtained after 7 days reaction at room temperature with 3 nm sized Cu_{2-x}S NCs and indium nitrate as indium precursor. EDS measurement were performed at two different locations at the TEM grid. B: TEM picture of parent Cu_{2-x}S NCs. C: Exciton decay curve and bi-exponential fit of the luminescent CIS NCs. D: TEM picture of the product CIS NCs.

photoluminescence decay measurements were performed. The TEM image of the parent Cu_{2-x}S NCs is shown in Figure 5.5B and the image of the resulting CIS NCs is shown in Figure 5.5D. The CIS NCs are clustered which makes measurement of their size difficult. The atomic ratios obtained with EDS measurements are shown in Table 5.1. From these ratios it is clear that indium is incorporated and the Cu:In

Table 5.1. Elemental ratios in the luminescent NCs, obtained after 7 days reaction at room temperature with 3 nm sized Cu_{2-x}S NCs and indium nitrate as indium precursor. EDS measurement were performed at two different locations at the TEM grid.

	1	2
	Atomic%	Atomic%
S	45.723	50.966
Cu	21.258	21.276
In	33.017	27.757
S:Cu	2.15	2.40
Cu	1	1
In:Cu	1.55	1.30
	$\text{Cu}_1\text{In}_{1.6}\text{S}_{2.2}$	$\text{Cu}_1\text{In}_{1.3}\text{S}_{2.4}$

ratio is slightly lower than 1. The lifetimes measured (Figure 5.5C, τ_1 36 ns, τ_2 206 ns) are comparable to those observed for directly synthesized CIS NCs. This provides strong support for the conclusion that the cation exchange resulted in luminescent CIS NCs and that at RT the cation diffusion in and out the crystal are perfectly balanced.

5.3.4. 4 and 15 nanometer sized nanocrystals at room temperature

The same room temperature method was used in exchange reactions with larger (4.0 ± 0.7 and 15 ± 1 nm sized) NCs. TEM analysis of the 4 nm sized sample after reaction, shows that the resulting particles are less visible (as we have seen earlier for CIS NCs) and that the self-organizing properties are only partly preserved (Figure 5.6A and B). The absorption spectrum does not change much, as can be seen in Figure 5.6C, which is similar to what was observed for the NCs with 3 nm diameter. The emission spectrum shows a band at 860 nm, which is reasonable for CIS NCs with a size around 4 nm. The exciton lifetimes obtained with a bi-exponential fit of the decay curve are 68 ns for the slow component and

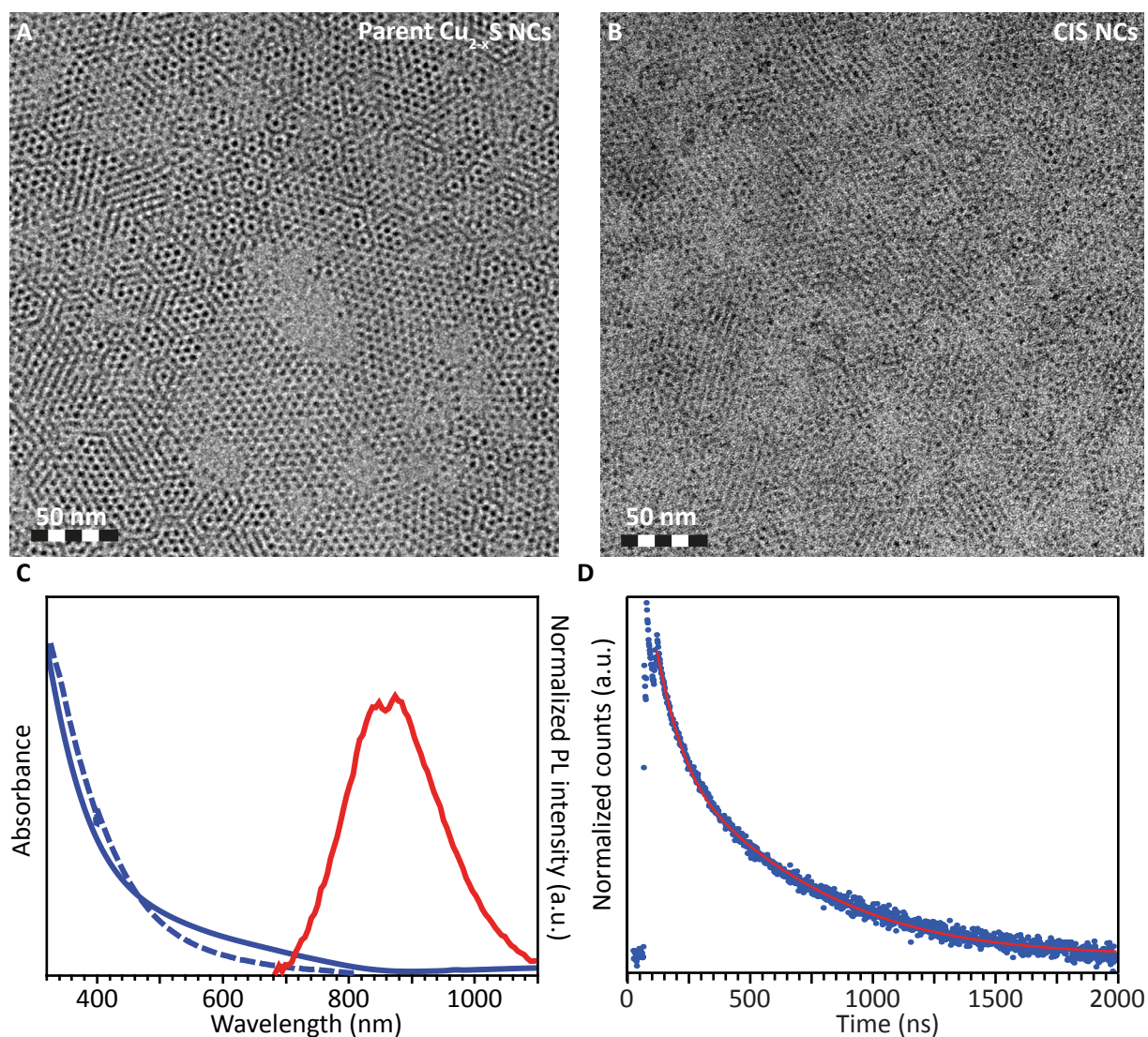


Figure 5.6. A: TEM picture of parent 4 nm Cu_{2-x}S NCs. B: TEM picture of product CIS NCs. C: Absorption spectra of parent Cu_{2-x}S NCs (dashed blue) and the product CIS NCs (solid blue) and emission spectrum of the product CIS NCs (solid red). D: Exciton decay curve and bi-exponential fit of the product CIS NCs.

408 ns for the long component (Figure 5.6D). These lifetimes are longer than for the 3 nm sized NCs, which is as expected for larger NCs: less overlap of the wave functions results in a slower decay rate.

Larger sized Cu_{2-x}S NCs (15 ± 1 nm) with amazing self-organizing properties (inset of Figure 5.7A shows long range atomic order) show after 5 days reaction at room temperature a remarkably increased polydispersity and a decreased average size (9.6 ± 2.5 nm). The absorption spectrum in Figure 5.7C shows that the plasmon resonance band of the parent Cu_{2-x}S NCs has disappeared, indicating a drastic reduction in the concentration of Cu vacancies, while the characteristic CIS absorption band at 800 nm becomes evident. The X-ray diffractogram of the product NCs is shown in Figure 5.7D and reveals next to peaks due to the Si sample holder, a number of peaks that can be ascribed to wurtzite CIS, although the peaks are shifted with respect to the reference. This shift may be ascribed to lattice strain, since the Cu_{2-x}S anion sublattice is expected to be preserved³ and the resulting crystal structure is therefore not exactly the same as that of wurtzite CIS. It should be noted that the thermodynamically favored struc-

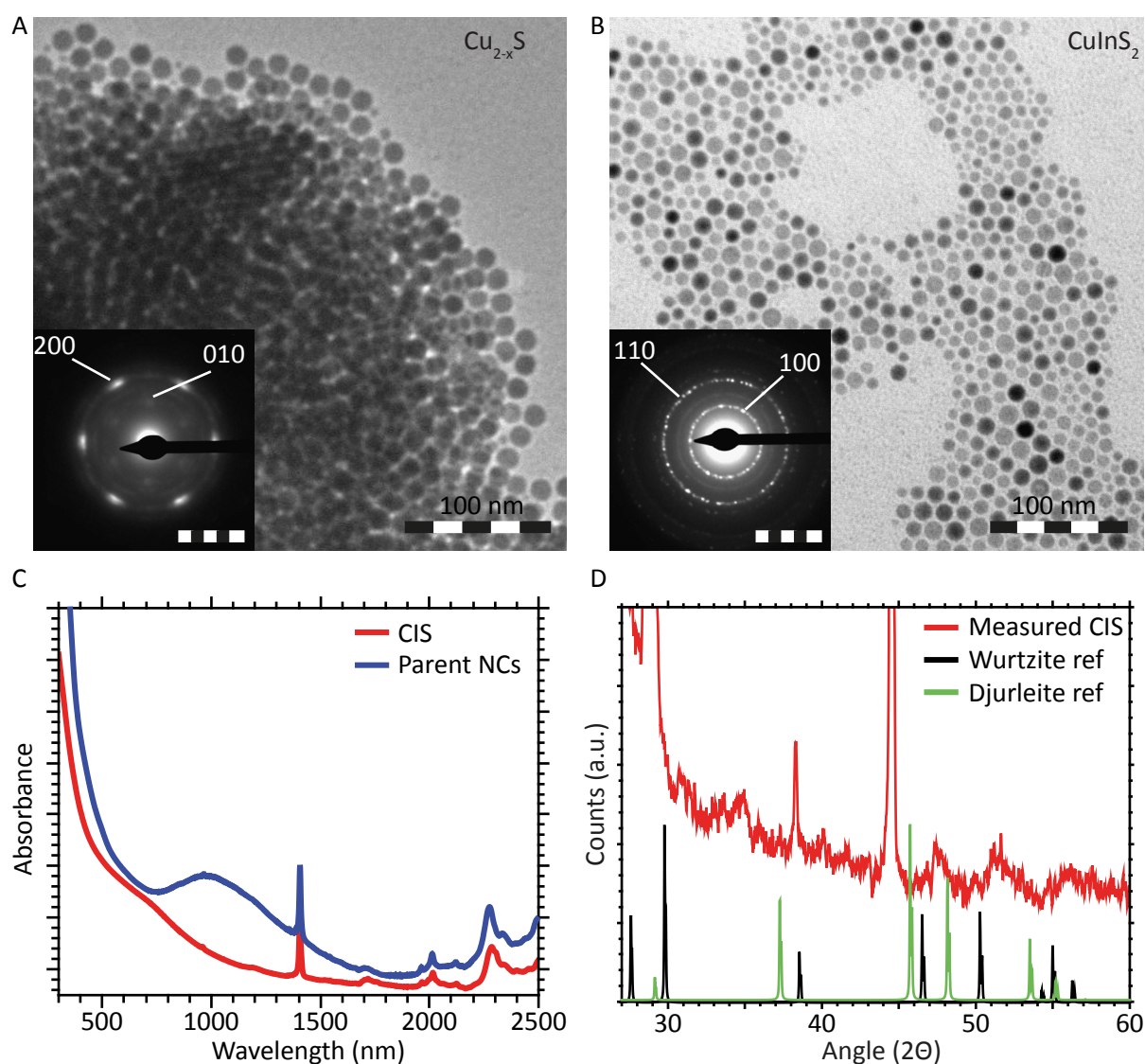


Figure 5.7. A: TEM picture of the parent Cu_{2-x}S NCs. The inset is the electron diffractogram of a large assembly, showing atomic order. B: TEM image of NCs after exchange and an electron diffractogram of a large area, showing randomly oriented NCs. C: Absorption spectra of parent Cu_{2-x}S NCs (blue) and product NCs (red). D: X-ray diffractogram of product NCs, with wurtzite CIS (ICDD 04-016-2016) and djurleite Cu_{2-x}S (ICDD 00-046-1195) reference.

ture of bulk CIS is roquesite, which is a derivative of the cubic zinc blende structure. This crystal structure is also usually adopted by directly synthesized CIS NCs. However, the parent Cu_{2-x}S NCs have the hexagonal chalcocite structure and therefore the product CIS NCs obtained by cation exchange from Cu_{2-x}S are expected to adopt the hexagonal wurtzite structure, since the roquesite structure would require a substantial reorganization of the anion sublattice, which is energetically unfavorable for the cation exchange. The structural transformation from chalcocite Cu_{2-x}S to wurtzite CIS will be discussed in more detail below.

The observations discussed above provide strong indications that 15 nm sized Cu_{2-x}S can be converted into CIS NCs by cation exchange within hours at temperatures of 100 °C or higher and within days at room temperature. However, at low temperatures the size dispersion of the NCs increases during the cation exchange process. This can be ascribed to an imbalance between the rates of Cu^+ extraction and In^{3+} incorporation, which leads to partial dissolution and ripening of the Cu_{2-x}S NCs, either prior to or in parallel to In^{3+} incorporation. In contrast, small Cu_{2-x}S NCs can be successfully converted into CIS NCs at room temperature, but completely dissolve at higher temperatures. This observation can also be ascribed to an imbalance between the Cu^+ extraction and In^{3+} incorporation rates, which in the case of small NCs results in total collapse of the anionic framework and dissolution of the NC. It is thus clear that the In^{3+} incorporation is the rate limiting step in all cases, regardless of the size of parent NC and reaction temperature. However, in the case of small NCs and low temperatures the In^{3+} incorporation rate appears to be sufficiently fast to preserve the structural integrity of the NC.

5.3.5. Lattice and crystal structure

As demonstrated by Jain *et al.*⁵ the anionic framework of the parent nanocrystal is usually preserved when the cations are exchanged. An important difference between the present work and previous works on cation exchange in nanocrystals^{8,10,11} is that only partial cation exchange is observed, despite the large excess of In^{3+} . This implies that the Cu^+ for In^{3+} cation exchange reaction in Cu_{2-x}S NCs is self-limited, and therefore does not reach completion even at very long reaction times. This can be understood by considering the crystal structure of chalcocite Cu_{2-x}S , wurtzite CIS and In_2S_3 .

In Figure 5.8A the crystal structure of copper sulfide is depicted and in Figure 5.8B the crystal structure of CIS. These figures make very clear that the anionic sublattice is almost the same in both materials, since a very small anion reorganization is needed (*viz.* a translation of 1.6% is needed in the lateral dimensions and of 4% in the vertical direction).¹⁵ Figure 5.8D shows the crystal structure of indium sulfide (In_2S_3 , red spheres represent the anions in the CIS lattice, purple spheres the anions of the In_2S_3 lattice). The large difference in the upper plane where the anions have to translate 58%¹⁵ makes it particularly clear that total exchange from Cu_{2-x}S to In_2S_3 would cost a substantial amount of energy, and therefore cannot happen under the mild conditions used in the present work. Higher temperatures are also unlikely to lead to total exchange because the large anion reorganization would result in the collapse of

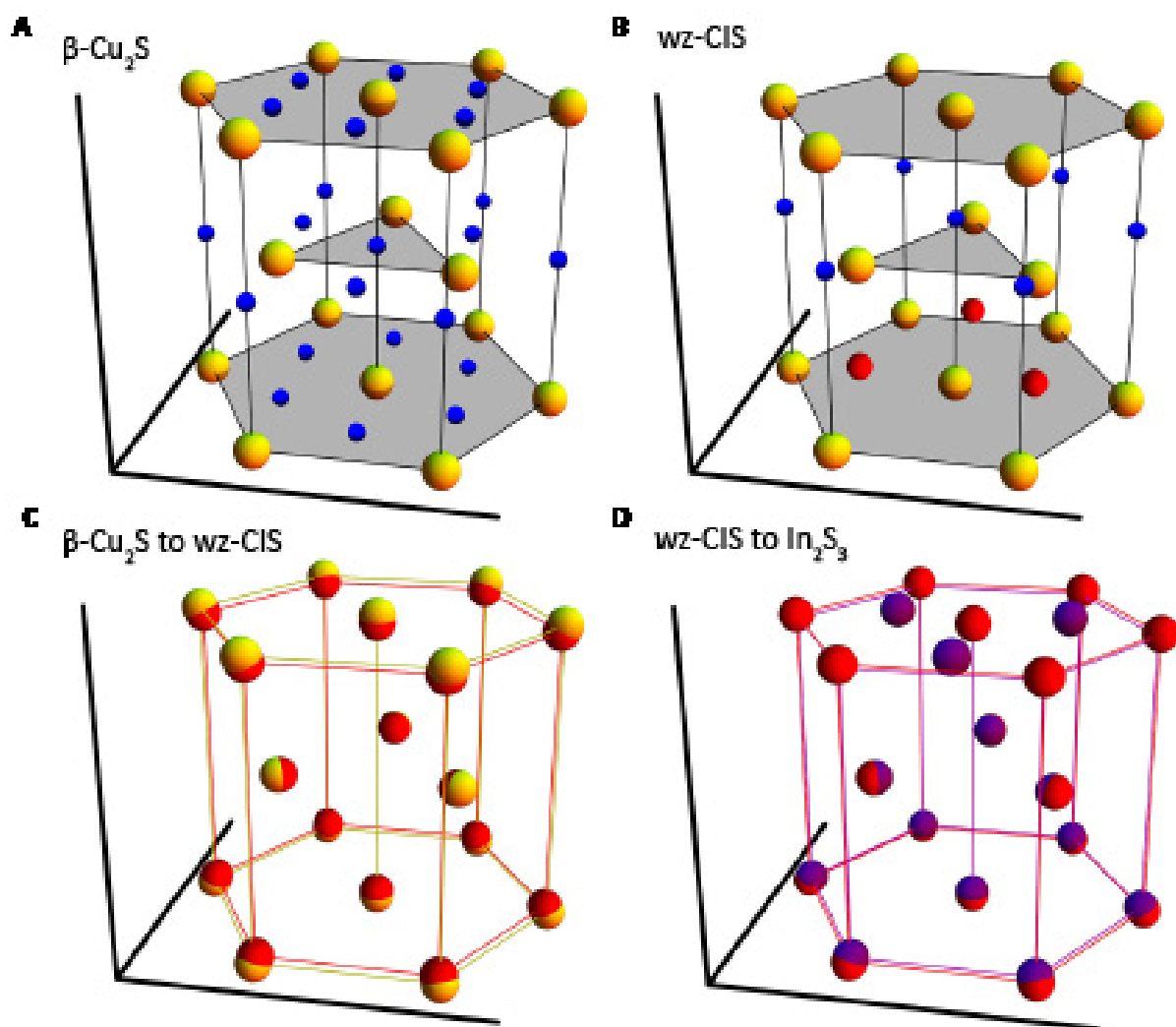


Figure 5.8. A: Crystal structure of Cu_{2-x}S . Blue spheres represent Cu^+ , yellow spheres represent the S^{2-} anions. B: Crystal structure of CIS, where red spheres represent the In^{3+} cations. The total amount of cations is reduced since monovalent copper is replaced by trivalent indium. C: Both anionic frameworks compared: yellow spheres are the S^{2-} ions in the copper sulfide lattice, the red spheres are the S^{2-} ions in the CIS lattice. D: The anionic lattice in In_2S_3 , where the red spheres indicate the positions of the anions in the CIS lattice and the purple spheres indicate the positions of the anions in the indium sulfide lattice. Reproduced from ref. [15]

the NC.

5.4. Conclusion & Outlook

With the right, mild, reaction conditions it is possible to exchange copper ions from small Cu_{2-x}S NCs for indium ions, to make luminescent CIS NCs. These mild reaction conditions are important, because at temperatures higher than room temperature the NCs are destroyed. The best indium precursor for this reaction is indium nitrate, when other precursors are used no indium is incorporated, possibly because their precursor salts are too stable in solution. For larger NCs changes are observed in the absorption spectrum after reaction at high temperatures, but it is not clear if and how much indium is incorporated. More analysis (XRD, EDS) should provide more insight in this matter.

More analysis would also allow comparison between the high temperature and low temperature re-

sults for the large NCs, which possibly gives valuable information about the exchange mechanism and the thermodynamic and kinetic factors playing a role. For the small particles it is interesting as well to study the mechanism in more detail. With EELS and HRTEM it may be possible to observe the reaction zone in which the actual exchange takes place and to measure the lattice parameters, to observe (small) anion reorganization or strained wurtzite CIS and thereby verify the mechanism proposed by Van der Stam *et al.*¹⁵ Possible future extensions of this successful exchange reaction are with different Cu_{2-x}S seeds, to fully exploit the variety of the possible morphologies of this material.

5.5. References

1. Tan, J. M. R. et al. Understanding the synthetic pathway of a single-phase quarternary semiconductor using surface-enhanced Raman scattering: a case of wurtzite $\text{Cu}_2\text{ZnSnS}_4$ nanoparticles. *J. Am. Chem. Soc.* **136**, 6684–92 (2014).
2. Kruszynska, M., Borchert, H., Parisi, J. & Kolny-Olesiak, J. Investigations of solvents and various sulfur sources influence on the shape-controlled synthesis of CuInS_2 nanocrystals. *J. Nanoparticle Res.* **13**, 5815–5824 (2011).
3. Kruszynska, M., Borchert, H. & Kolny-olesiak, J. Synthesis and Shape Control of CuInS_2 Nanoparticles. *J. Am. Chem. Soc.* **132**, 15976–15986 (2010).
4. Kolny-Olesiak, J. & Weller, H. Synthesis and application of colloidal CuInS_2 semiconductor nanocrystals. *ACS Appl. Mater. Interfaces* **5**, 12221–37 (2013).
5. Jain, P. K., Amirav, L., Aloni, S. & Alivisatos, A. P. Nanoheterostructure cation exchange: anionic framework conservation. *J. Am. Chem. Soc.* **132**, 9997–9999 (2010).
6. Van der Stam, W. et al. Self-assembly of colloidal hexagonal bipyramid- and bipyramid-shaped ZnS nanocrystals into two-dimensional superstructures. *Nano Lett.* **14**, 1032–7 (2014).
7. Li, W. et al. Morphology evolution of Cu_{2-x}S nanoparticles: from spheres to dodecahedrons. *Chem. Commun. (Camb)*. **47**, 10332–4 (2011).
8. Tang, A. et al. One-pot synthesis and self-assembly of colloidal copper(I) sulfide nanocrystals. *Nanotechnology* **21**, 285602 (2010).
9. Beberwyck, B. J., Surendranath, Y. & Alivisatos, a. P. Cation Exchange: A Versatile Tool for Nanomaterials Synthesis. *J. Phys. Chem. C* **117**, 19759–19770 (2013).
10. Son, D. H., Hughes, S. M., Yin, Y. & Paul Alivisatos, a. Cation exchange reactions in ionic nanocrystals. *Science* **306**, 1009–12 (2004).
11. Li, H. et al. Synthesis of uniform disk-shaped copper telluride nanocrystals and cation exchange to cadmium telluride quantum disks with stable red emission. *J. Am. Chem. Soc.* **135**, 12270–8 (2013).
12. Rivest, J. B. & Jain, P. K. Cation exchange on the nanoscale: an emerging technique for new material synthesis, device fabrication, and chemical sensing. *Chem. Soc. Rev.* **42**, 89–96 (2013).
13. Li, H. et al. Sequential cation exchange in nanocrystals: preservation of crystal phase and formation of metastable phases. *Nano Lett.* **11**, 4964–70 (2011).
14. Augé, J., Lubin-Germain, N. & Uziel, J. Recent Advances in Indium-Promoted Organic Reactions. *Synthesis (Stuttg)*. **2007**, 1739–1764 (2007).
15. Van der Stam, W., Berends, A. C., Rabouw, F. T., Meeldijk, J. D. & de Mello Donega, C. Luminescent CuInS_2 quantum dots by partial cation exchange in Cu_{2-x}S nanocrystals. *Submitted*

6. Colloidal Cu_{2-x}S -CIS heteronanorods

6.1. Introduction

As stated before in chapter 2, the working principle of solar cells is based on the separation of charge carriers. This can be achieved by an asymmetry in the material, for example a p-n junction. The development of quantum dot containing solar cells went from the simple Schottky-junction solar cell via the depleted heterojunction cell to the most state-of-the-art bulk nano-heterojunction cell.¹⁻⁴ A nanoscale phase separation gives rise to extended carrier lifetimes, as shown for the bulk nano-heterojunction cell, which has a threefold increased performance.^{3,4} When the phase separation can take place within one NC, the carrier lifetimes and thereby cell performance might increase even more.

A p-n junction on the nanoscale can be in principle achieved by making a heteronanocrystal in which Cu_{2-x}S (p-type semiconductor)⁵ and CIS (n-type semiconductor) are joined by an interface. In Figure 6.1 the band alignment of CIS and Cu_{2-x}S is shown, and the possible charge carrier separation when the NCs are excited. Although the band offsets are not very large (CB of Cu_{2-x}S lies 0.45 eV higher than for CIS and the VB of CIS lies 0.75 eV lower than for Cu_{2-x}S)⁶⁻⁸ this is still large enough to prevent back-recombination through thermal excitation at room temperature ($k_B T \approx 0.026$ eV). Because the crystal lattices of Cu_{2-x}S and CIS are very similar⁹ the hetero-interfacial recombination is expected to be small. These characteristics suggest that a heterostructure of these two materials is promising for solar cell applications. Several of the very first heterojunction solar cells already contained Cu_{2-x}S as p-type material,^{10,11} showing that this is a very suitable material for these photovoltaic applications. CIS is known for its interesting properties and potential for photovoltaics as well for quite some time¹² and is also already studied in its nanoscale form for use in these devices.¹³

In this chapter the synthesis of colloidal Cu_{2-x}S -CIS heteronanorods is studied, based on the work of Lu *et al.*¹⁰ The influence of various synthesis conditions (Cu:In ratio, reaction atmosphere, time and

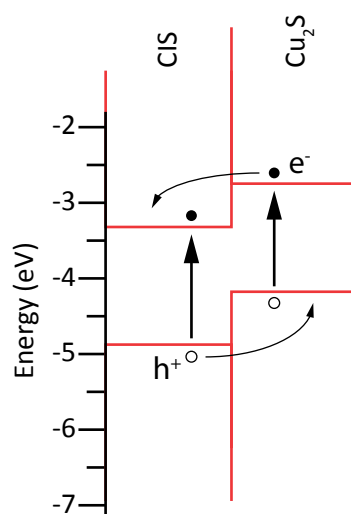


Figure 6.1. Band alignment of CIS and Cu_2S . When an exciton is created the hole will move to the highest level of the VB in Cu_2S and the electron will move to the lowest level in the CB in CIS.

temperature) on size and shape of the resulting particles was investigated. Anisotropic shapes (such as rods) are preferred to provide more control over assembly of the NCs into larger structures and electronic directionality.^{10,14}

6.2. Experimental

6.2.1. Materials

Copper (II) sulphate.pentahydrate (Sigma Aldrich, 99.995%), Indium (III) nitrate hydrate (Sigma Aldrich, 99.99%), 1-dodecanethiol (DDT, Sigma Aldrich, ≥98%), Oleic acid (OA, Sigma Aldrich, 90%), Ethanol (Sigma Aldrich, ≥99.8%), Ethanol (Sigma Aldrich, 99.8%), 1-Butanol (Sigma Aldrich, 99.8%), Oleylamine (OLAM, Sigma Aldrich, tech. 70%), Copper (II) acetylacetonate (Sigma Aldrich, 99.99+%), Toluene (Sigma Aldrich, 99.8%). OLAM was degassed for 2 hours at 150-200 °C before usage.

6.2.2. Synthesis

The protocol of Lu *et al.*¹⁰ was followed to prepare colloidal Cu_{2-x}S-CIS heteronanorods. 0.40 mmol CuSO₄·5H₂O and 0.20 mmol In(NO₃)₃·xH₂O were mixed with 5 mL DDT and 4 mL OA, after which the reaction was carried out under air, at 240 °C for 30 minutes. Then the NCs were cooled to RT, washed with ethanol and dispersed in toluene. Variations were made in reaction atmosphere (N₂), Cu:In precursor ratio (0.2:0.2 mmol, 0.54:0.2 mmol or 0:0.2 mmol), reaction time (10–30 min) and reaction temperature (200 °C for 30 min to 3 days). An overview of all the reaction conditions used can be found in Appendix H.

For the seeded injection first Cu_{2-x}S particles were synthesized following the protocol of Tang *et al.*,⁵ mixing 3 mmol Cu(acac)₂, 10 mL DDT and 20 mL OLAM. This mixture was heated to 250 °C and reacted 10 minutes at this temperature. A few mL of this original dispersion was redispersed in 5 mL DDT. 0.20 mmol In(NO₃)₃ and 4 mL OA were mixed and heated to 240 °C, then the Cu_{2-x}S NCs were injected and reacted 30 min.

6.2.3. Characterization

Absorption spectra were recorded with a Perkin Elmer Lambda 950 UV/VIS/NIR spectrophotometer. Transmission electron microscopy (TEM) images were taken with a Philips Tecnai Scripting microscope (FEI company), with an accelerating voltage of 100 or 120 kV. Energy dispersive X-ray spectroscopy (EDS) measurements were performed with a FEI Tecnai-20F microscope equipped with a Field Emission Gun, a Gatan 694 CCD camera and an EDA spectrometer. The microscope was operated at 200 kV. Acquisition time for the EDS measurements was 45 s. X-ray diffraction (XRD) measurements were performed with a Philips PW 1729/40 X-ray generator operated at 40 kV and 20 mA. A Philips PW 1820/00 sample chamber was used and a Philips PW 3710/00 detector. The NCs were brought onto a crystalline

silicon wafer and dried to air before measuring. The XRD references are taken from the International Centre for Diffraction Data (ICDD). The diffractogram used for the Cu_{2-x}S djurleite crystal structure is number 00-046-1195, for the CIS wurtzite structure this is 04-016-2016.

6.3. Results & discussion

6.3.1. Reaction steps and synthesis variables

Colloidal heteronanorods were prepared following the protocol of Lu *et al.*¹⁰ The resulting NCs with a head-rod appearance are shown in Figure 6.2A and B and have a rod length of (26.7 ± 1.3) nm, a rod width of (12.6 ± 1.2) nm and the heads have a thickness of (11.0 ± 1.4) nm (this is in the direction perpendicular to the rod). The absorption spectrum (Figure 6.2C) shows a broad band from 500 to 800 nm, which is much broader than earlier reported for Cu_{2-x}S -CIS.^{15,16} The X-ray diffractogram (Figure 6.2D) is consistent with the wurtzite crystal structure. This is in agreement with literature.^{10,15} The peaks are a few degrees shifted compared to the reference, which may be due to small stoichiometric changes.

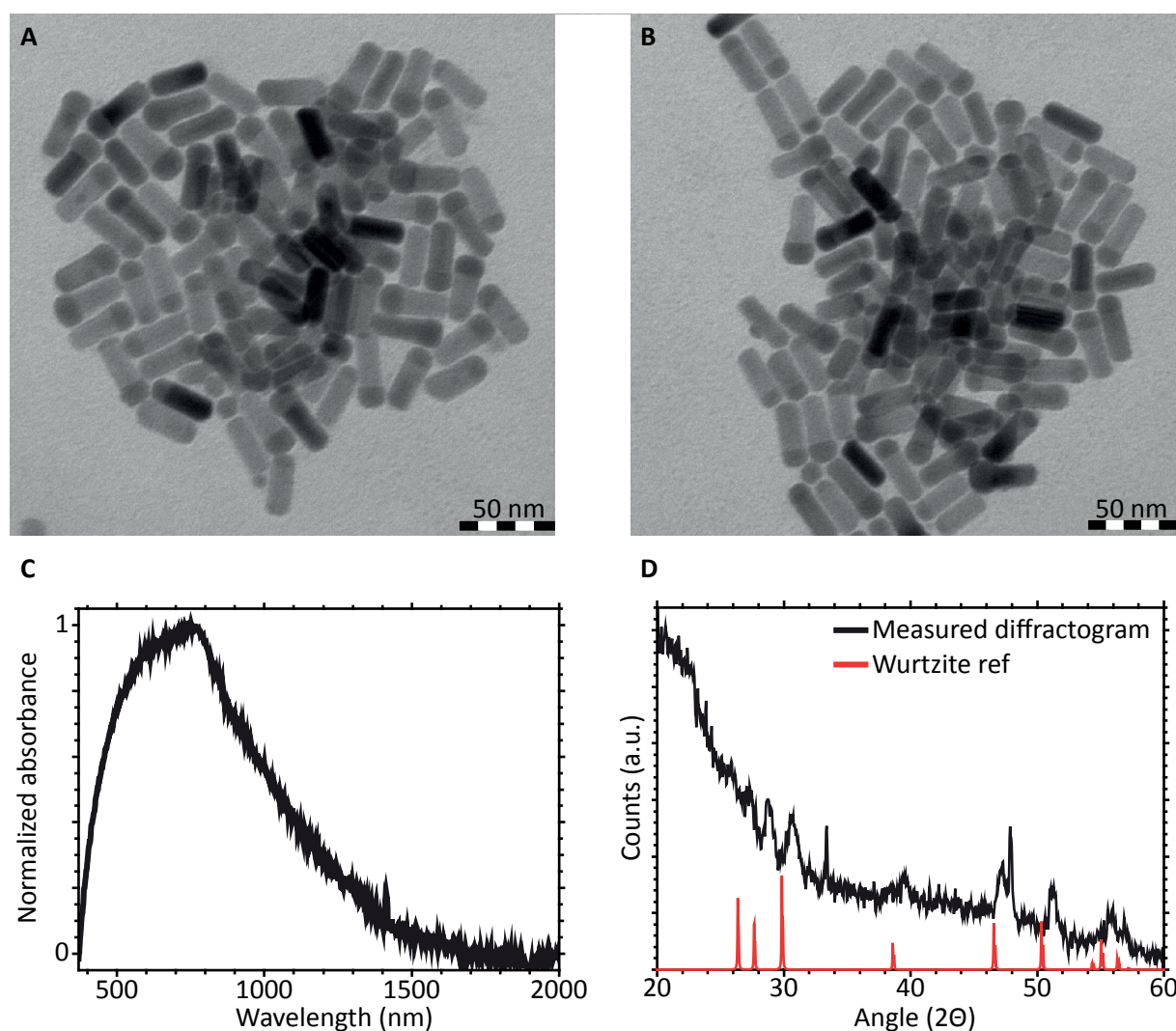


Figure 6.2. A and B: TEM pictures of the heteronanorods obtained following the standard protocol of Lu *et al.*¹⁰ C: Absorption spectrum of the heteronanorods. D: X-ray diffractogram of the NCs (black) and reference peaks of a CIS wurtzite structure (red) from ICDD 04-016-2016..

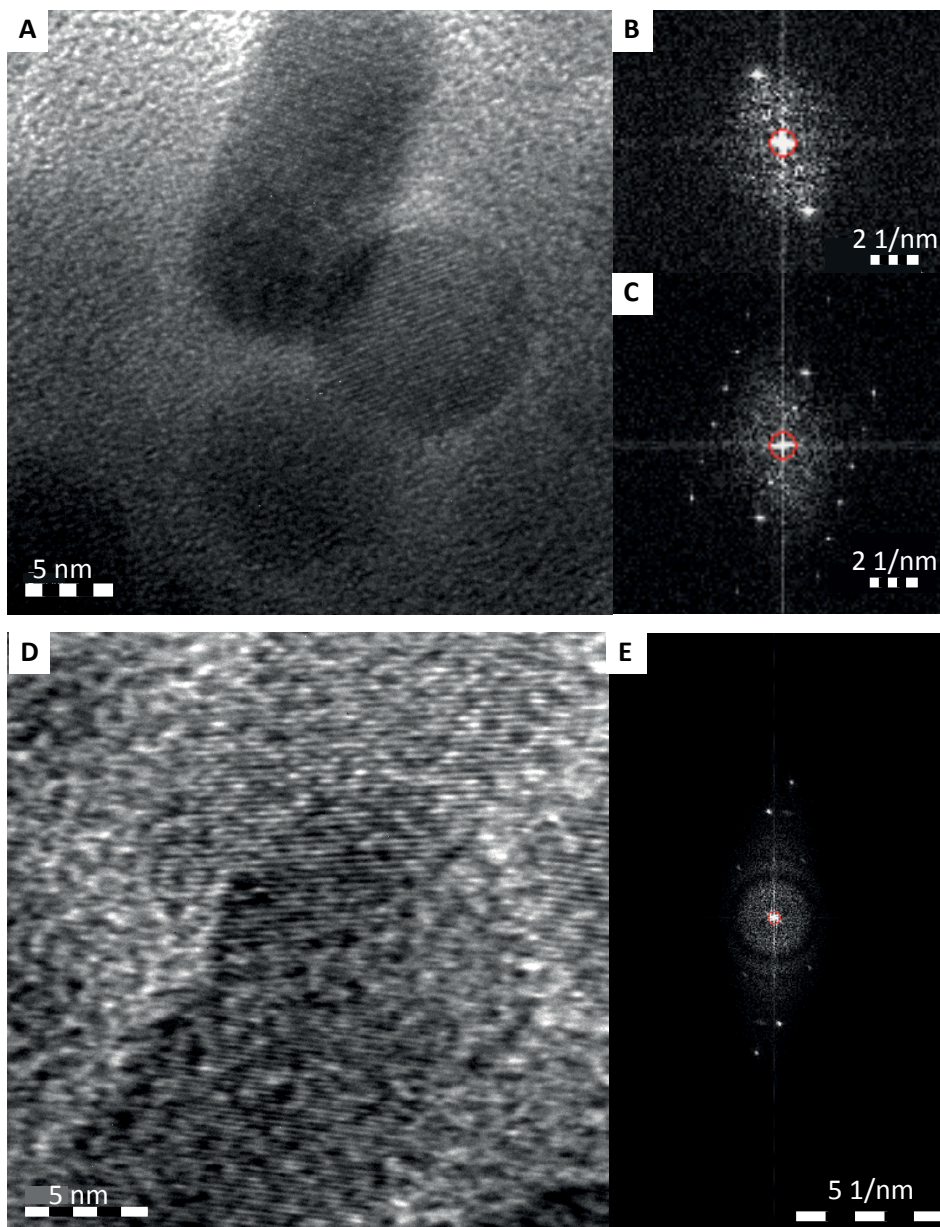


Figure 6.3. A: HRTEM image of a rod and head, lattice fringes are visible. B: FFT of the head. C: FFT of the rod. D: HRTEM image with visible lattice fringes. E: FFT of image D.

The broadening is due to the small size of the particles, compared with the bulk reference. The lattice spacings obtained from the FFT of some HRTEM pictures (Figure 6.3A-C) are 0.15, 0.22, 0.29 and 0.32 nm for the rod and 0.32 nm for the heads. The FFT of the less clear picture (Figure 6.3D and E) gives similar same values. These values are consistent with the wurtzite structure as well.¹⁰ The reaction parameters and resulting NC characteristics discussed here will be taken as standard throughout the rest of this chapter.

To investigate the composition of both parts of the NC, two STEM line scans were performed. The pictures of the corresponding heteronanorods are shown in Figure 6.4A and B and the corresponding atomic ratios are shown below (Figure 6.4C and D). Since the samples were drifting somewhat during the measurements, it is not possible to be conclusive, but the lines indicate a decrease in copper and

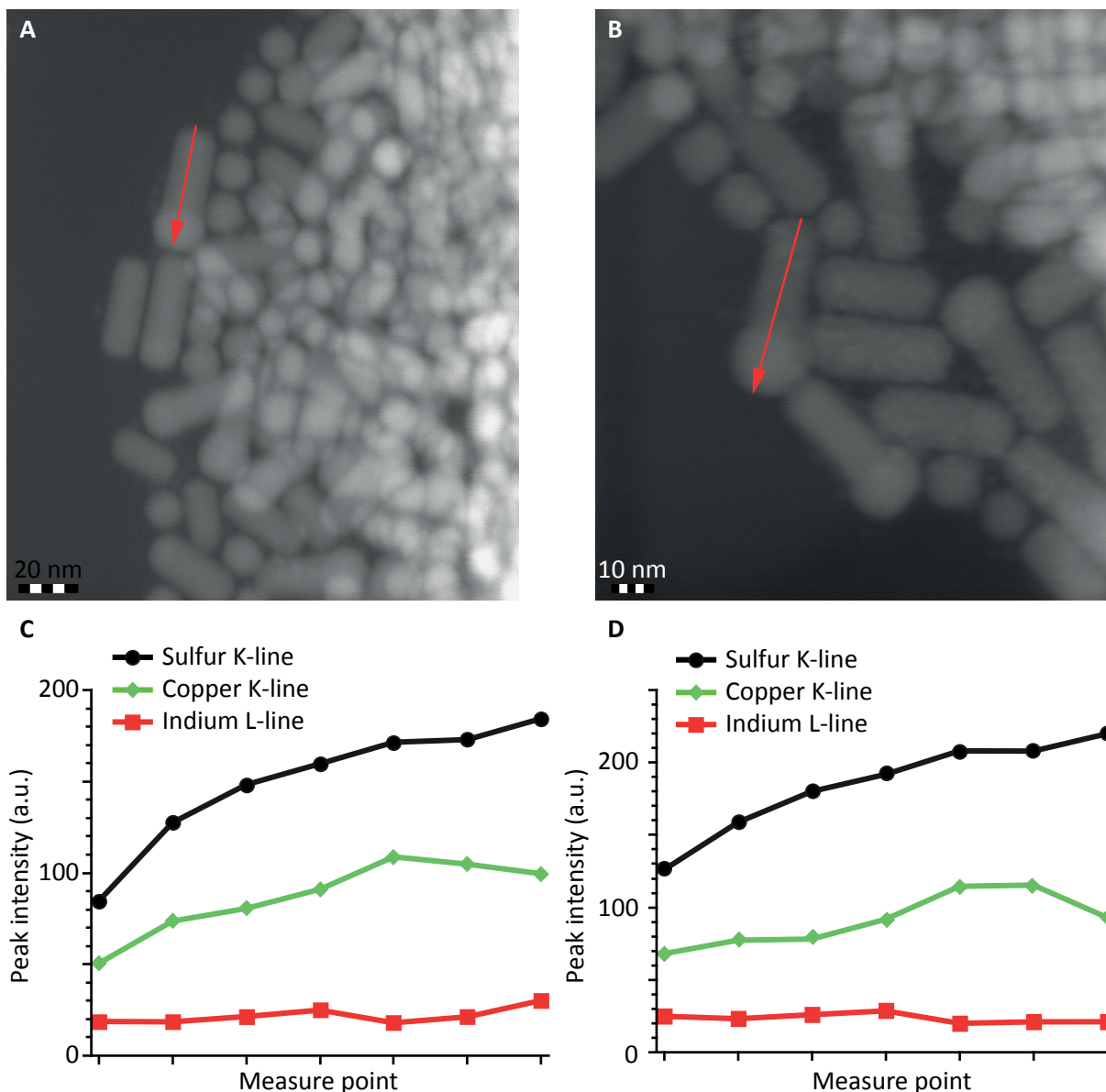


Figure 6.4. A, B: STEM pictures of the heteronanorod sample with the red arrow indicating the direction of the line scan. C, D: Resulting atomic ratios.

increase in indium when moving from the rod to the head. This suggests that the rods are CIS and the heads Cu_{2-x}S , but intermixing cannot be excluded. To follow the formation of these NCs and get insight into the reaction mechanism, a number of syntheses was performed with samples taken over time.

A. Reaction time and temperature

To study the influence of reaction time and temperature on the formation of the heteronanorods, NCs synthesized at 250 °C for 15 minutes were compared to the NCs synthesized at 240 °C for 30 min. The TEM pictures of the 250 °C sample are shown in Figure 6.5A and B. The rods have dimensions of (25.6 ± 2.4) by (10.6 ± 1) nm and the heads have a thickness of (9.9 ± 1.4) nm. This is slightly smaller than the NCs synthesized at 240 °C, which is in agreement with classical nucleation theory, that states that more nuclei can form at a higher temperature, thus resulting in a larger number of smaller NCs. The absorption spectra (Figure 6.5C) show a similar large band between 500 and 800 nm, indicating that

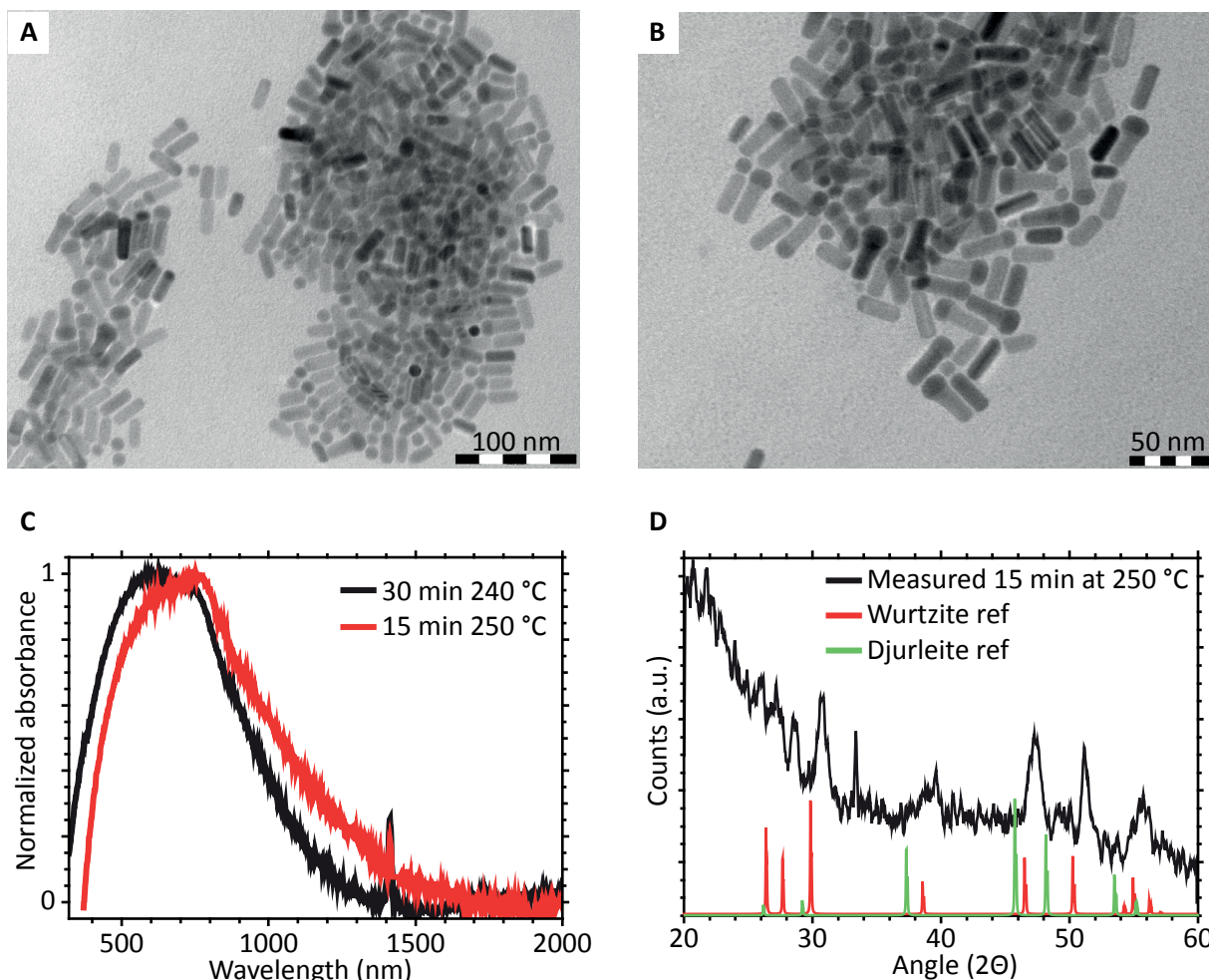


Figure 6.5. A,B: TEM pictures of NCs synthesized at 250 °C for 15 minutes. C: Absorption spectra of the NCs synthesized at 250 °C compared to the heteronanorods described above. D: X-ray diffractogram of the NCs compared with references, ICDD 00-046-1195 for the djurleite structure, ICDD 04-016-2016 for wurtzite.

the samples are very similar regarding their composition. The X-ray diffractogram (Figure 6.5D) shows peaks at the same positions as for the 30 min at 240 °C sample, indicating a wurtzite crystal structure, but also an additional peak at 49°, indicating that the djurleite crystal structure is present as well. The TEM images suggest that the attachment between heads and rods in the high temperature sample is weaker, since many individual rods are observed. Independent spherical NCs (i.e. heads) are not as clearly observed.

To find out more about the temperature required for nucleation and growth, several syntheses under N_2 atmosphere were performed, with a Cu:In precursor ratio of 0.54:0.2 mmol and different reaction temperatures and durations. A synthesis at 240 °C for 30 minutes yielded a very polydisperse sample (TEM pictures Figure 6.6A and B). The absorption spectrum is different from that observed above (see Figure 6.6C) and the X-ray diffractogram (Figure 6.6D) shows next to the characteristic CIS wurtzite peaks, also djurleite $Cu_{2-x}S$ peaks.

With the same Cu:In precursor ratio a synthesis was performed with a reaction mixture that was first heated to 240 °C, then directly cooled to 200 °C and reacted for 30 minutes at his temperature. The

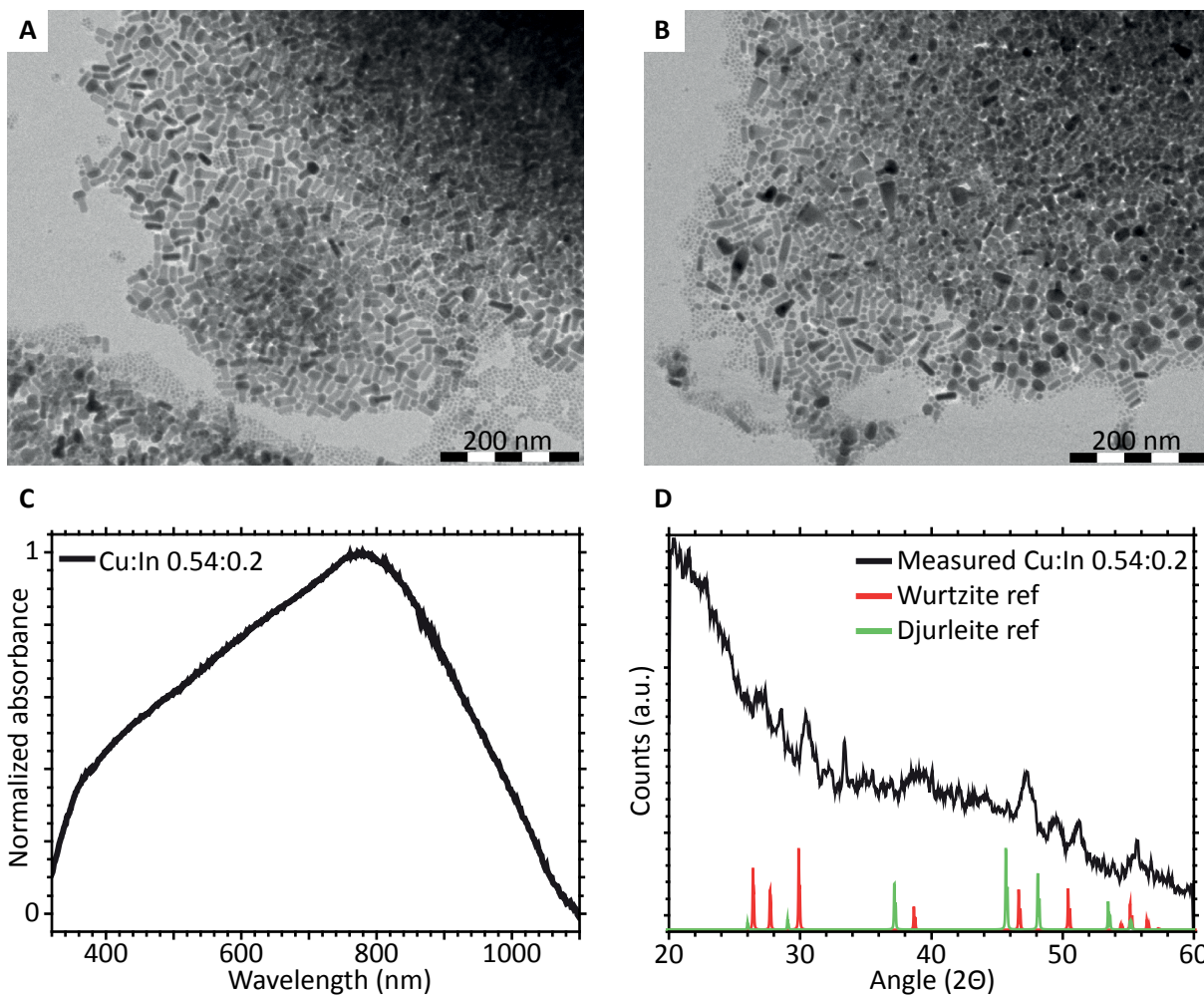


Figure 6.6. A,B: TEM pictures of NCs synthesized under N_2 with different precursor ratio: excess copper compared to the heteronanorods of the beginning of this section. C: Absorption spectrum of the product NCs. D: X-ray diffractogram of the NCs compared with references ICDD 00-046-1195 for djurleite, 04-016-2016 for wurtzite.

TEM picture (Figure 6.7A) shows that some nucleation has taken place but no well-defined crystalline material was formed. The absorption spectrum (Figure 6.7B) shows the characteristic copper-DDT complex peak,¹⁷ indicating that only this copper sulfide precursor complex was formed in the reaction. Performing the nucleation at a constant temperature of 200 °C, without prior heating to 240 °C, results in

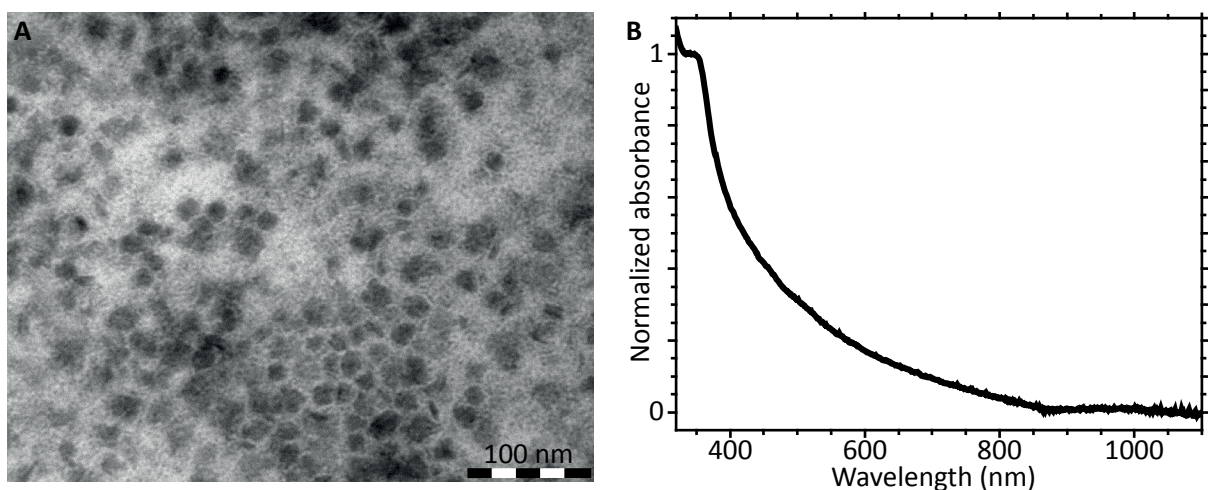


Figure 6.7. A: TEM picture of product material after heating up to 240 °C and 30 min reaction at 200 °C with Cu:In precursor ratio of 0.54:0.2 mmol and under N_2 atmosphere. B: Absorption spectrum of the product material.

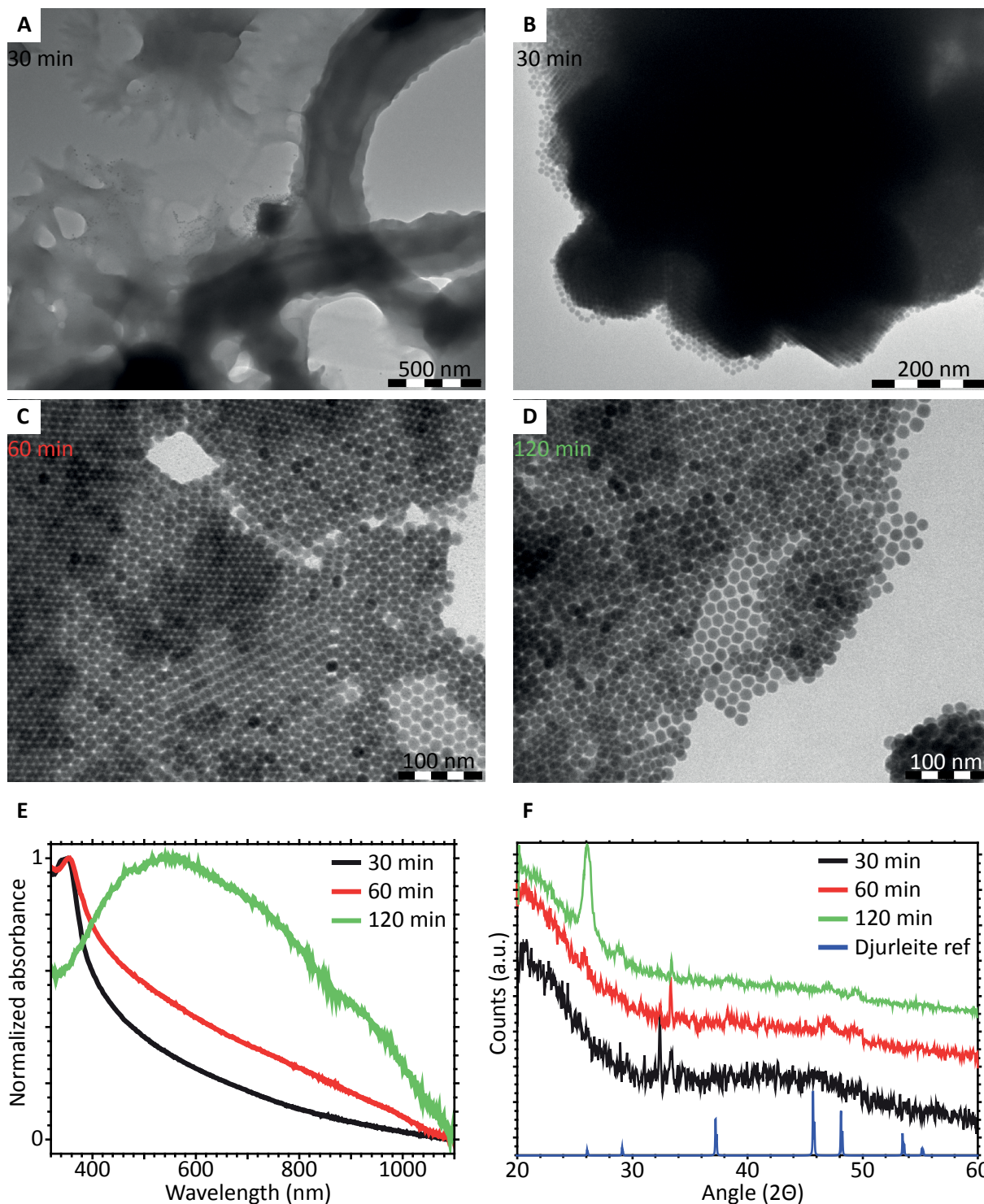


Figure 6.8. A,B: TEM picture of Cu-SDT precursor gel and a few NCs after 30 minutes reaction at 200 °C with Cu:In precursor ratio of 0.54:0.2 mmol and under N₂ atmosphere. C: TEM picture of NCs after 60 minutes reaction at 200 °C. D TEM picture of NCs after 120 min reaction at 200 °C. E: Absorption spectra of the three samples, showing the transition from gel to NCs. F: X-ray diffractograms of the three samples and Cu_{2-x}S djurleite reference ICDD 00-046-1195.

spherical Cu_{2-x}S NCs that form large self-assembled super lattices (Figure 6.8B-D). The diameter of the spherical NCs increases from (8.7 ± 0.7) nm after 30 minutes (Figure 6.8A and B), to (13.7 ± 1) nm after 60 minutes (Figure 6.8C) and (16.6 ± 1.7) nm after 120 minutes (Figure 6.8D). After 30 minutes a lot of the copper-SDT precursor complexes are still present, according to the TEM picture in Figure 6.8A and the absorption spectrum (Figure 6.8E) that shows mainly the Cu-SDT precursor peak at 350 nm. Due

to this gel the X-ray diffractogram (Figure 6.8F) does not show clear peaks. After 60 minutes less gel is observed with TEM (Figure 6.8C) and djurleite peaks are observed in the X-ray diffractogram (Figure 6.8F). The absorption spectrum however still shows a distinct peak at 350 nm (Figure 6.8E) indicating the presence of copper-DDT complexes. After 120 minutes a clear Cu_{2-x}S absorption band is visible (Figure 6.8E) and the X-ray diffractogram shows clear djurleite peaks. The peak at 26° is ascribed to an undefined impurity at the sample holder or substrate. These experiments clearly show that copper indium sulfide is not formed at 200°C within a time frame of hours. To verify if CIS can be formed at all at this temperature, a reaction was carried out over 2 days. TEM analysis (Figure 6.9A) shows the formation of heterostructures, of which one part is expected to be CIS. Figure 6.9C shows the absorption spectrum of the NCs obtained after 2 days reaction at 200°C , that overlaps with both the absorption spectrum of the Cu_{2-x}S NCs obtained after 2 hours reaction at 200°C and the Cu_{2-x}S -CIS heteronanorods with large CIS rods from the beginning of this chapter. The X-ray diffractogram in Figure 6.9D, showing both wurtzite and djurleite peaks again confirms the presence of both the heterostructures and Cu_{2-x}S NCs. These observations not only show that CIS can be formed at low temperatures, but that more time is needed, but also suggest that the formation of the heteronanorods is a three-step process. First copper-DDT complexes are formed, from which Cu_{2-x}S NCs nucleate and grow. Finally CIS heterogeneously

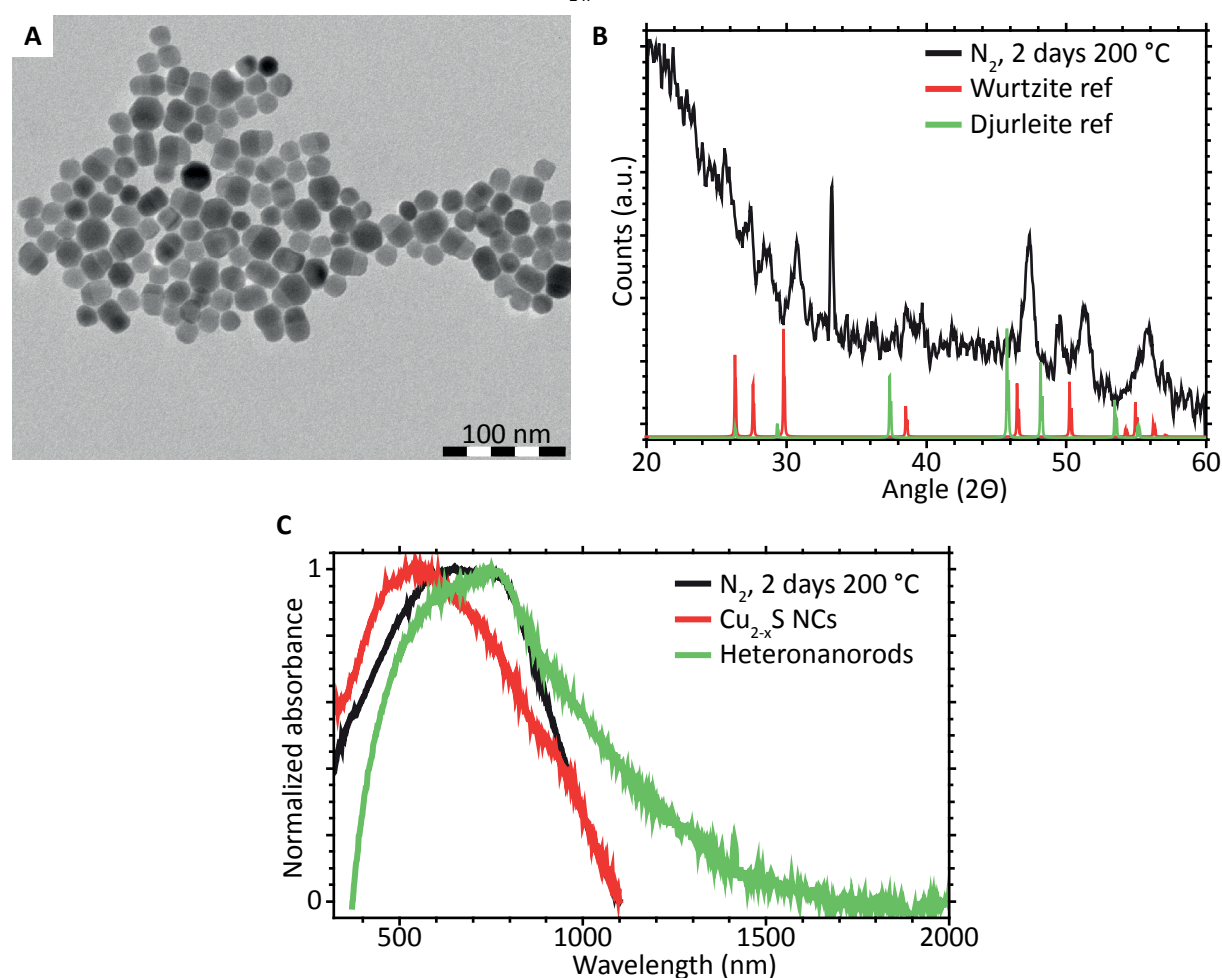


Figure 6.9. A: TEM image of NCs obtained after 2 days reaction at 200°C under N_2 atmosphere and with Cu:In precursor ratio of 0.54:0.2 mmol. B: X-ray diffractogram of the NCs and references ICDD 00-046-1195 (green) and 04-016-2016 (red). C: Absorption spectrum of NCs obtained after 2 days reaction at 200°C under N_2 atmosphere and with Cu:In precursor ratio of 0.54:0.2 mmol, the large and monodisperse heteronanorods described in the beginning of this section, and the Cu_{2-x}S NCs that were formed after 120 min reaction at 200°C under N_2 atmosphere and with Cu:In precursor ratio of 0.54:0.2 mmol.

nucleates and grows on the Cu_{2-x}S NCs.

To study the formation of the heteronanorods in more detail, the standard synthesis ($\text{Cu}:\text{In}$ 0.4:0.2, under air, 30 min at 240°C) was performed again and during warming up and reaction, samples were taken. The absorption spectra of the different samples (Figure 6.10E) confirm the above proposed

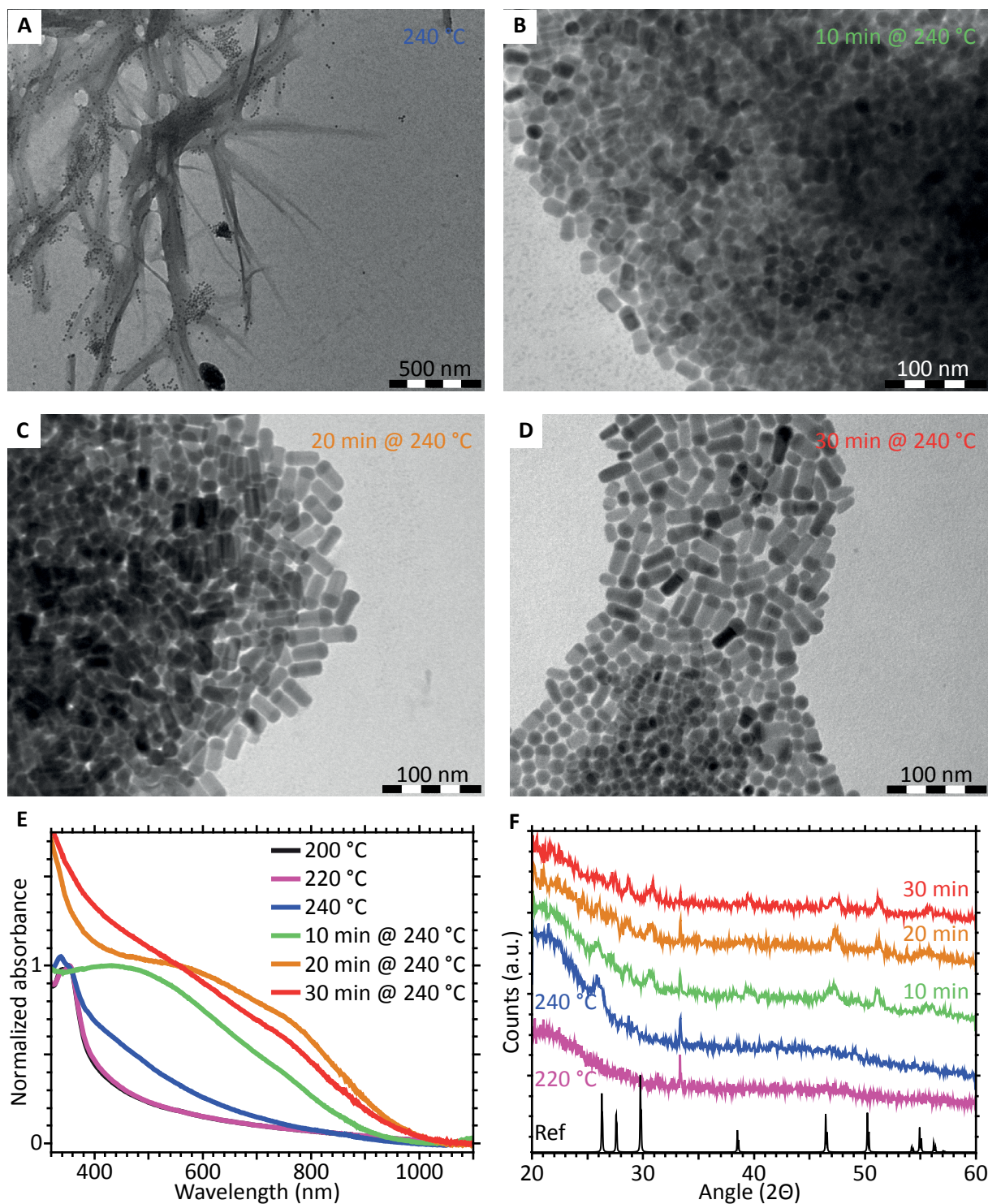


Figure 6.10. AD: TEM pictures of samples taken during the warming up and reaction of the heteronanorod synthesis at 240°C during 30 minutes, under air, with $\text{Cu}:\text{In}$ precursor ratio of 0.4:0.2 mmol. E: The absorption spectra of the samples taken during the synthesis, showing the formation of the Cu -DDT precursor complex, the Cu_{2-x}S NCs and the growth of the heteronanorods. F: X-ray diffractograms of the same samples and CIS wurtzite reference (ICDD 04-016-2016).

growth mechanism. The first three samples show the characteristic absorption peak at 350 nm indicating the presence of copper-DDT precursor. Then a broad band develops around 500 nm, indicating the formation of Cu_{2-x}S NCs. At later stages an even broader absorption band appears, indicating the formation of the heteronanocrystals. The same evolution is seen when the samples are analyzed with TEM. Figure 6.10A shows the first sample taken at a temperature of 240 °C and indeed some Cu_{2-x}S NCs with a diameter of (10.9 ± 1) nm are present in the gel. In the pictures B, C and D the CIS rods grow on Cu_{2-x}S NCs, from a size of (15.8 ± 1.9) by (13.8 ± 1.3) nm to (25.2 ± 4.5) by (13.4 ± 1.5) nm and finally (26.2 ± 5.4) by (12.9 ± 2.1) nm. The nanocrystal heads keep roughly the same diameter of (9.4 ± 1.3) nm in the sample after 10 minutes at 240 °C, (11.1 ± 2) nm in the sample after 20 minutes and (10.6 ± 2.6) after 30 minutes. This observation indicates that the copper used for the formation of the CIS rods is still available in solution and is not coming from the dissolution of the Cu_{2-x}S NC heads. The smaller uniformity in size and shape compared to the standard synthesis described at the beginning of this section, is probably due to the disturbance of the system every time a sample was taken. The formation of the heterostructures via Cu_{2-x}S NCs is less clear in the X-ray diffractograms (Figure 6.10F) but the appearance of the wurtzite peaks is quite clear.

B. Reaction atmosphere

To investigate the influence of the reaction atmosphere (inert (N_2) or air), the same Cu:In precursor ratio (0.4:0.2 mmol), reaction temperature and time (240 °C, 30 minutes) were used for a reaction under N_2 atmosphere. The TEM pictures of the resulting NCs are shown in Figure 6.11A and B, displaying a very large size and shape distribution. The absorption spectrum (Figure 6.11C) shows a very broad band, where multiple bands, originating from different particles with different compositions might overlap. The X-ray diffractogram (Figure 6.11D) shows peaks at positions consistent with a wurtzite crystal structure. The very large difference in resulting particle size and shape distribution indicates that the reaction atmosphere has a very large influence on the nucleation and growth rate. During the reaction Cu^{2+} is reduced to Cu^+ , which goes slower in an oxidizing environment, which is the case when oxygen is present. When the reaction takes place in nitrogen atmosphere, this reduction reaction is too fast and less controlled, thereby leading to a large variety of sizes and shapes of the resulting particles.

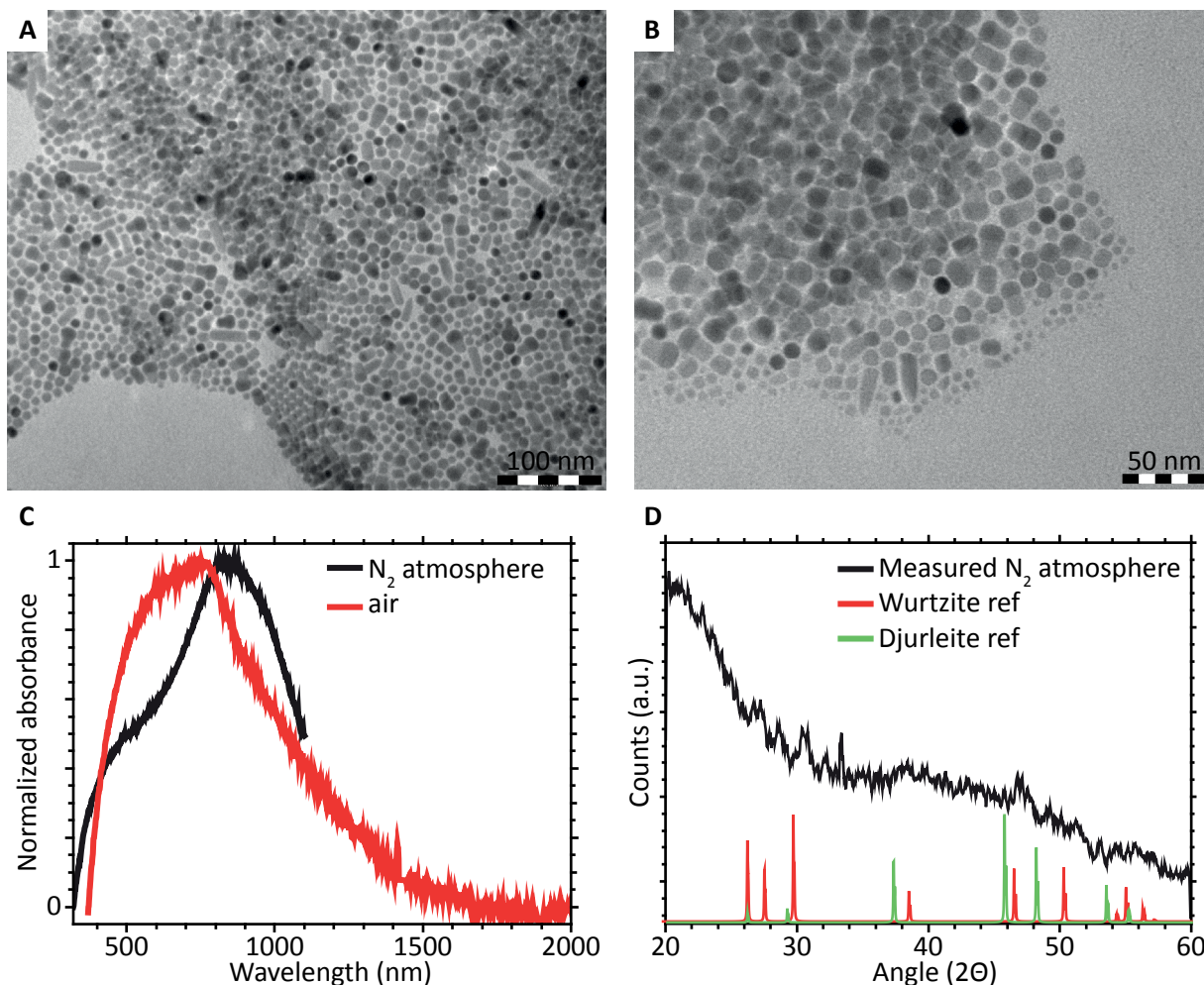


Figure 6.11. A,B: TEM images of NCs synthesized under N_2 for 30 minutes at 240 °C. C: Absorption spectra of the NCs synthesized under N_2 compared to the under air synthesized NCs. D: X-ray diffractogram of the NCs synthesized under N_2 and the reference spectra of $Cu_{2-x}S$ djurleite (ICDD 00-046-1195) and CIS wurtzite (ICDD 04-016-2016) structure.

C. Copper-indium precursor ratio

To investigate the role of the copper excess, a synthesis was performed with a Cu:In precursor ratio of 0.2:0.2 mmol (instead of the 0.4:0.2 or 0.54:0.2 ratio used in syntheses described above). The question is whether this influences the size and shape of the $Cu_{2-x}S$ NC intermediate, the size and shape of the CIS nanorods, or both. TEM analysis (Figure 6.12A) of the resulting NCs shows that the Cu:In ratio influences both components of the heterostructure. The CIS part is not a normal rod but is tapered and much longer (length of (44.7 ± 9.1) nm) than the NCs described above. The width at the heterointerface is (31.5 ± 7.5) nm. The $Cu_{2-x}S$ heads have a diameter of (9.7 ± 3) nm, which is comparable with earlier samples. In contrast, their shape is no longer spherical, but appears to be flattened. The absorption spectrum (Figure 6.12C) and X-ray diffractogram (Figure 6.12B) do not show any surprises but the broad peak between 500 and 800 nm and peaks at the wurtzite positions respectively.

The importance of the $Cu_{2-x}S$ NCs for the nucleation of CIS becomes even clearer if the synthesis is performed in the absence of copper precursor, at 240 °C for 1.5 hour and under air. In this case thin wires were formed (only 1-2 nm in diameter, Figure 6.13A), which are expected to be indium sulfide since only indium and sulfide precursors were present in the reaction mixture and these wire structures are

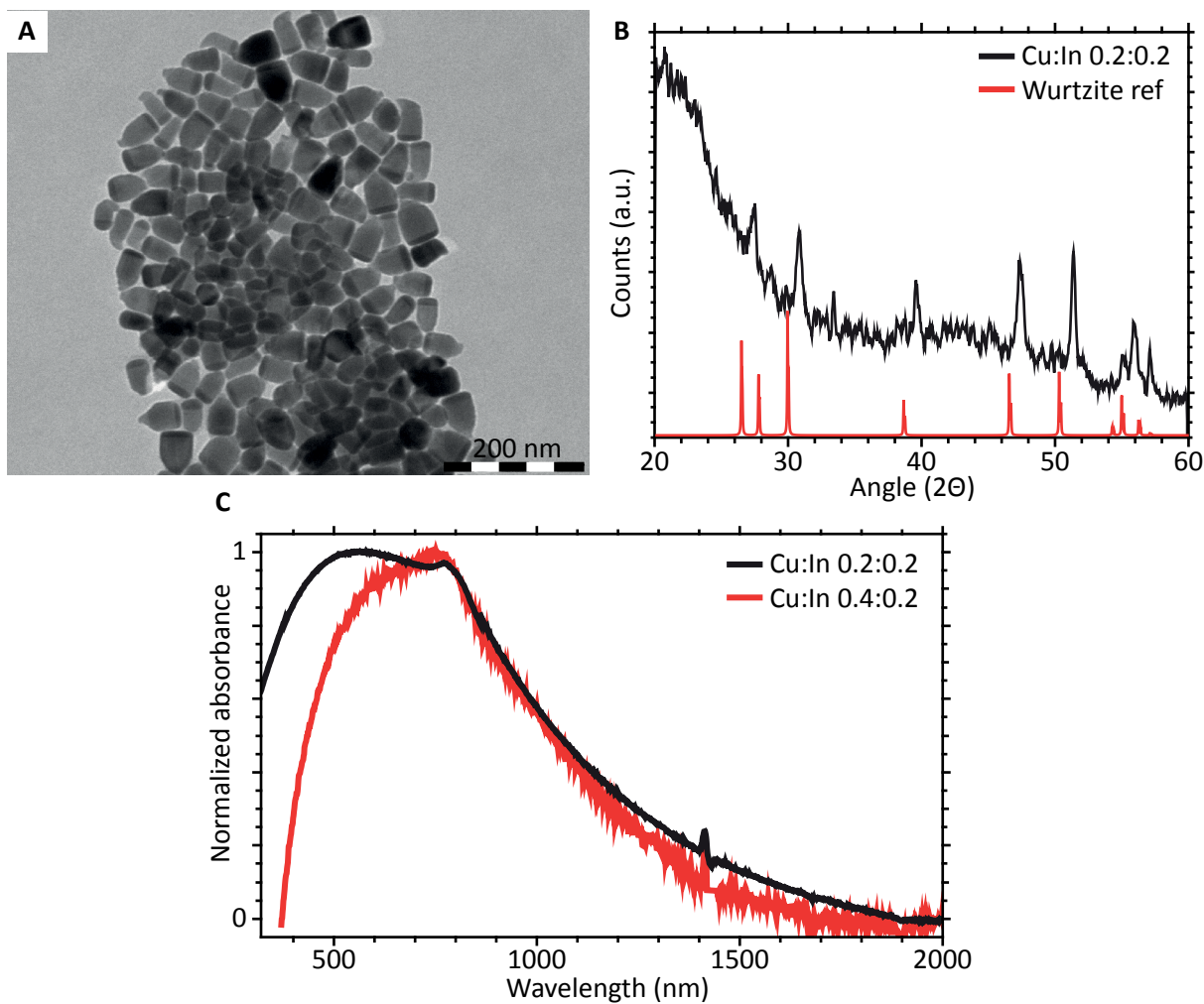


Figure 6.12. A: TEM image of NCs synthesized with Cu:In precursor ratio of 1:1, under N_2 atmosphere for 30 minutes at 240 °C. B: Corresponding X-ray diffractogram and wurtzite reference ICDD 04-016-2016. C: Absorption spectra of NCs synthesized with Cu:In precursor ratios of 1:1 and 2:1.

earlier reported for In_2S_3 .¹⁸ The absorption spectrum (Figure 6.13B) is remarkable, but cannot be compared to literature spectra, since no absorption spectra were earlier reported for In_2S_3 nanowires.^{18,19}

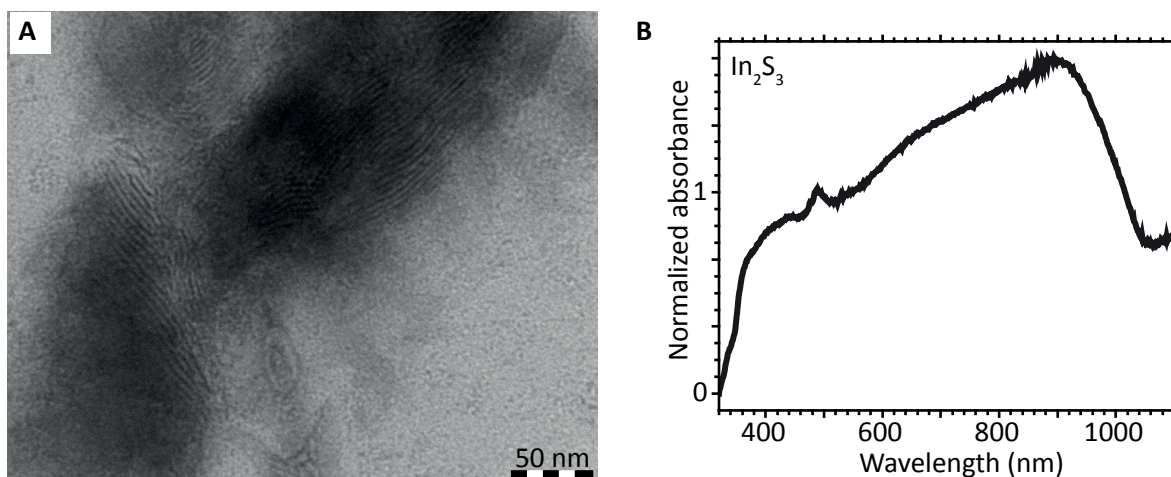


Figure 6.13. A: TEM image of ultra thin In_2S_3 wires synthesized during 1.5 hour at 250 °C under air. B: Corresponding absorption spectrum.

6.3.2. Seeded injection

Since the proposed formation mechanism of the Cu_{2-x}S heteronanorods involved a Cu_{2-x}S NC intermediate, it is interesting to investigate whether it is possible to grow CIS on preformed Cu_{2-x}S NC seeds and whether the shape and size of the CIS NCs could be controlled by the size and shape of the Cu_{2-x}S NC seeds. For this seed injection synthesis, Cu_{2-x}S platelets with a diameter of (19.6 ± 4.5) nm and a thickness of (11.1 ± 1.7) nm were used (see Figure 6.14A). These platelets were redispersed in DDT and injected to a mixture of indium nitrate and OA at a temperature of 240 °C. Samples were taken after 10, 20 and 30 minutes reaction and the resulting NCs are shown in the TEM pictures in Figure 6.14B, C and D respectively. The dimensions of the NCs remain the same over these 30 minutes (rod length of (19.2 ± 2.5) nm after 10 minutes, (18.8 ± 3) nm after 20 minutes and (19.9 ± 2.8) nm after 30 minutes), indicating that CIS formation is a fast process and only size and shape broadening take place after the initial growth. The diameter of the CIS part corresponds very well to the diameter of the original Cu_{2-x}S NC seeds ((19.6 ± 4.5) nm), namely (21.4 ± 2.8) nm after 10 minutes, (21.2 ± 2.9) nm after 20 minutes and (22.2 ± 3.9) nm after 30 minutes. The absorption spectra of the NC seeds, the heteronanorods obtained with the seeded injection and the heteronanorods obtained with the one-pot synthesis from the beginning of this chapter are shown in Figure 6.14E. The difference in shape of these spectra can at this point not be explained.

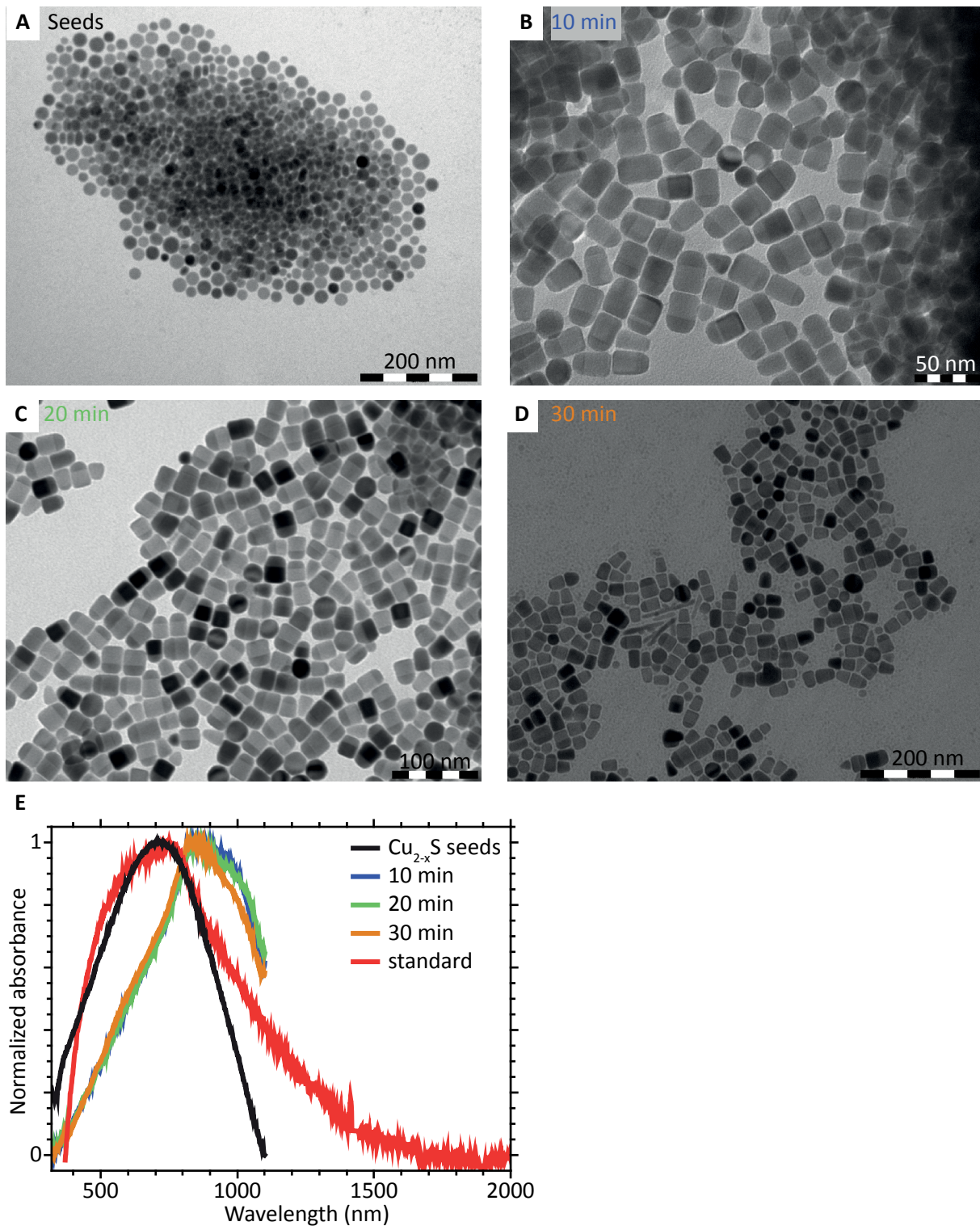


Figure 6.14. A: TEM image of the Cu_{2-x}S NC seeds. B: TEM image of sample taken after 10 minutes reaction at 240 °C under air, C: after 20 minutes reaction at 240 °C under air, D: after 30 minutes reaction at 240 °C under air. E: Absorption spectra of the Cu_{2-x}S NC seeds, samples taken during the seed injection reaction and the heteronanorods obtained with the synthesis described at the beginning of this chapter.

6.3.3. Self-assembly

For use in photovoltaic applications large area ordered structures of the heteronanorods are desired. Two NC assembly methods were reported earlier. In the first a TEM grid is placed in the dispersion under an angle of $\sim 40^\circ$ with the dispersion surface. Then the solvent slowly evaporates and the NCs are

deposited on the grid.²⁰ In the second method slow evaporation of the solvent of the NC dispersion placed on ethylene glycol as immiscible liquid substrate leads to self-assembly of the NCs.²¹ Several attempts with different concentrations and temperatures were undertaken but so far without any positive result. An overview of the results obtained is given in Appendix I.

6.4. Conclusion & Outlook

The formation of colloidal Cu_{2-x}S -CIS heteronanorods is proposed to be a three-step process. First a copper-DDT complex is formed from which Cu_{2-x}S NCs originate. The CIS nanorods then nucleate and grow on the Cu_{2-x}S crystal. This mechanism is somewhat different than the one that was proposed earlier by Kruszynska *et al.*¹⁵ who stated that the nucleation of CIS happens inside the Cu_{2-x}S crystal and that Cu_{2-x}S converts to CIS *via* cation exchange. This is not observed in this study, where the Cu_{2-x}S part of the heterocrystal retains its size and shape during the CIS growth and is solely located at one side of the heterocrystal.

The ratio of the copper and indium precursors in the reaction mixture is important, as it determines the resulting size and shape of both parts of the heteronanocrystal. Another way to control this is to use the seeded injection method, whereby preformed Cu_{2-x}S NC seeds are used, which, as we know from chapter 5, can be synthesized in a wide variety of sizes and shapes.

To fully exploit the possible application in solar cells, stabilization of the heteronanorod is important, as well as the assembly of the NCs. Furthermore, effective charge separation upon irradiation and charge transport have to be investigated.

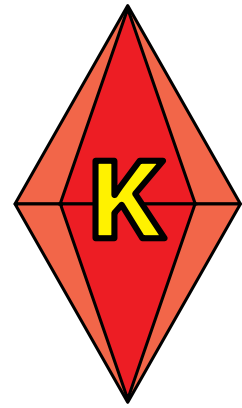
6.5. References

1. Kramer, I. J. & Sargent, E. H. The architecture of colloidal quantum dot solar cells: materials to devices. *Chem. Rev.* **114**, 863–82 (2014).
2. Pattantyus-Abraham, A. G. et al. Depleted-Heterojunction Colloidal Quantum Dot Solar Cells. *ACS Nano* **4**, 3374–3380 (2010).
3. Rath, A. K. et al. Solution-processed inorganic bulk nano-heterojunctions and their application to solar cells. *Nat. Photonics* **6**, 529–534 (2012).
4. Lan, X., Masala, S. & Sargent, E. H. Charge-extraction strategies for colloidal quantum dot photovoltaics. *Nat. Mater.* **13**, 233–40 (2014).
5. Tang, A. et al. One-pot synthesis and self-assembly of colloidal copper(I) sulfide nanocrystals. *Nanotechnology* **21**, 285602 (2010).
6. Hunger, R., Pettenkofer, C. & Scheer, R. Dipole formation and band alignment at the Si(111)/CuInS₂ heterojunction. *J. Appl. Phys.* **91**, 6560 (2002).
7. Van de Walle, C. G. & Neugebauer, J. Universal alignment of hydrogen levels in semiconductors, insulators and solutions. *Nature* **423**, 626–8 (2003).
8. Liu, G., Schulmeyer, T., Brötz, J., Klein, a. & Jaegermann, W. Interface properties and band alignment of Cu₂S/CdS thin film solar cells. *Thin Solid Films* **431-432**, 477–482 (2003).
9. Kolny-Olesiak, J. & Weller, H. Synthesis and application of colloidal CuInS₂ semiconductor nanocrystals. *ACS Appl. Mater. Interfaces* **5**, 12221–37 (2013).
10. Lu, X., Zhuang, Z., Peng, Q. & Li, Y. Controlled synthesis of wurtzite CuInS₂ nanocrystals and their side-by-side nanorod assemblies. *CrystEngComm* **13**, 4039 (2011).
11. Hsieh, H. C. The effect of Cu diffusion in a Cu₂S/CdS heterojunction solar cell. *J. Appl. Phys.* **53**, 1727 (1982).
12. Rau, U. & Schock, H. W. Electronic properties of Cu(In,Ga)Se₂ heterojunction solar cells-recent achievements, current understanding, and future challenges. *Appl. Phys. A Mater. Sci. Process.* **69**, 131–147 (1999).
13. Sankir, N. D., Aydin, E., Sankir, M. & Bozbey, A. Influence of excitation frequency on structural and electrical properties of spray pyrolyzed CuInS₂ thin films. *J. Mater. Process. Technol.* **214**, 1879–1885 (2014).
14. Oh, N. et al. Double-heterojunction nanorods. *Nat. Commun.* **5**, 3642 (2014).
15. Kruszynska, M., Borchert, H. & Kolny-olesiak, J. Synthesis and Shape Control of CuInS₂ Nanoparticles. *J. Am. Chem. Soc.* **132**, 15976–15986 (2010).
16. Kruszynska, M., Borchert, H., Parisi, J. & Kolny-Olesiak, J. Investigations of solvents and various sulfur sources influence on the shape-controlled synthesis of CuInS₂ nanocrystals. *J. Nanoparticle Res.* **13**, 5815–5824 (2011).
17. Akkerman, Q. Size, shape, composition and assembly control over colloidal copper chalcogenide nanocrystals. (2014).
18. Lutfi Abdelhady, A., Ramasamy, K., Malik, M. a. & O'Brien, P. Very narrow In₂S₃ nanorods and nanowires from a single source precursor. *Mater. Lett.* **99**, 138–141 (2013).

19. Li, Z., Tao, X., Wu, Z., Zhang, P. & Zhang, Z. Preparation of In₂S₃ nanoparticle by ultrasonic dispersion and its tribology property. *Ultrason. Sonochem.* **16**, 221–4 (2009).
20. Evers, W. H. et al. Entropy-driven formation of binary semiconductor-nanocrystal superlattices. *Nano Lett.* **10**, 4235–4241 (2010).
21. Evers, W. H. et al. Low-dimensional semiconductor superlattices formed by geometric control over nanocrystal attachment. *Nano Lett.* **13**, 2317–23 (2013).

7. Acknowledgments

The enormous amount of results described in this thesis, would not have been there without my daily supervisor, Ward. You helped me the first out of habit weeks to get around and in the months that followed you were always there to answer my questions, explain things and think along. I really appreciated your patience and enthusiasm. Where at first I did not really understand why someone would spend every second Sunday in a football stadium, after our visit to Utrecht - Cambuur I do. Thank you for organizing this wonderful experience and I hope 'Utrege' will one day be dominating the top of the competition. As Captain Kesterite you of course were the man behind this scientific *supper* successful and, more important, very social group of students. I enjoyed being part of it. Celso, thank you for always taking time for our work discussions. The not ceasing abundance of ideas and your enthusiasm always gave me new energy to get to the lab and, luckily, more is yet to come! I also really appreciate that you gave me the opportunity to visit ICL. Mathijs you are 1-0 ahead but I challenge you hereby for ICL 2017. Freddy, or more appropriate professor Rabouw, I would like to thank you for your help with the lifetime measurements and your patience with explaining Mathematica to me. The Friday morning measurements on the Eddy 1 with you and Ward were always fun. I really liked our discussions on the origin of the CIS emission and I am looking forward to really solving this difficult problem. Relinde and Hans, thank you for your help around the lab and solving many practical problems. Hans Meeldijk I would like to thank for taking time to do EDX and HRTEM measurements. Of course the group of (master) students, part of them fellow team Kesterite members (Quinten and Josine), made this a very nice year. The complete CMI group I would like to thank for a wonderful year and I am very happy I will be part of this family for the next four years as well.



8. Appendices

Appendix A

Overview of synthesis conditions used for samples described in chapter 3.

Table 8.1. Overview of synthesis conditions used for CIS samples

Sample	Cu : In ratio (mmol)	Ligands used	Reaction temperature (°C)	Reaction time (min)	Atmosphere	Figure in chapter
AB 1	0.4 : 0.4	DDT	230	11	N ₂	Figure 3.1A, Figure 3.2, Figure 3.4A, Figure 3.6
AB 6	idem	DDT, OA	230	11	idem	Figure 3.6
AB 8.1	idem	DDT	210	10	idem	Figure 3.1B
AB 8.2	idem	idem	idem	20	idem	idem
AB 8.3	idem	idem	idem	30	idem	idem
AB 8.4	idem	idem	idem	40	idem	idem
AB 8.5	idem	idem	idem	50	idem	idem
AB 13	0.8 : 0.4	idem	230	11	idem	Figure 3.4B
AB 16	0.3 : 0.6	idem	idem	idem	idem	Figure 3.4A, Figure 3.5
AB 18	0.2 : 0.8	idem	idem	idem	idem	Figure 3.4A
AB 21	0.3 : 0.6	idem	idem	idem	air	Figure 3.5
AB 22	0.3 : 0.6	idem	210	15	N ₂	Figure 3.5
AB 48	0.4 : 0.4	idem	210	40	idem	Figure 3.7B
AB 72	idem	idem	230	20	idem	Figure 3.1A
AB 73	idem	idem	230	11	air	Figure 3.2A

Appendix B

TEM pictures of several samples described in chapter 3.

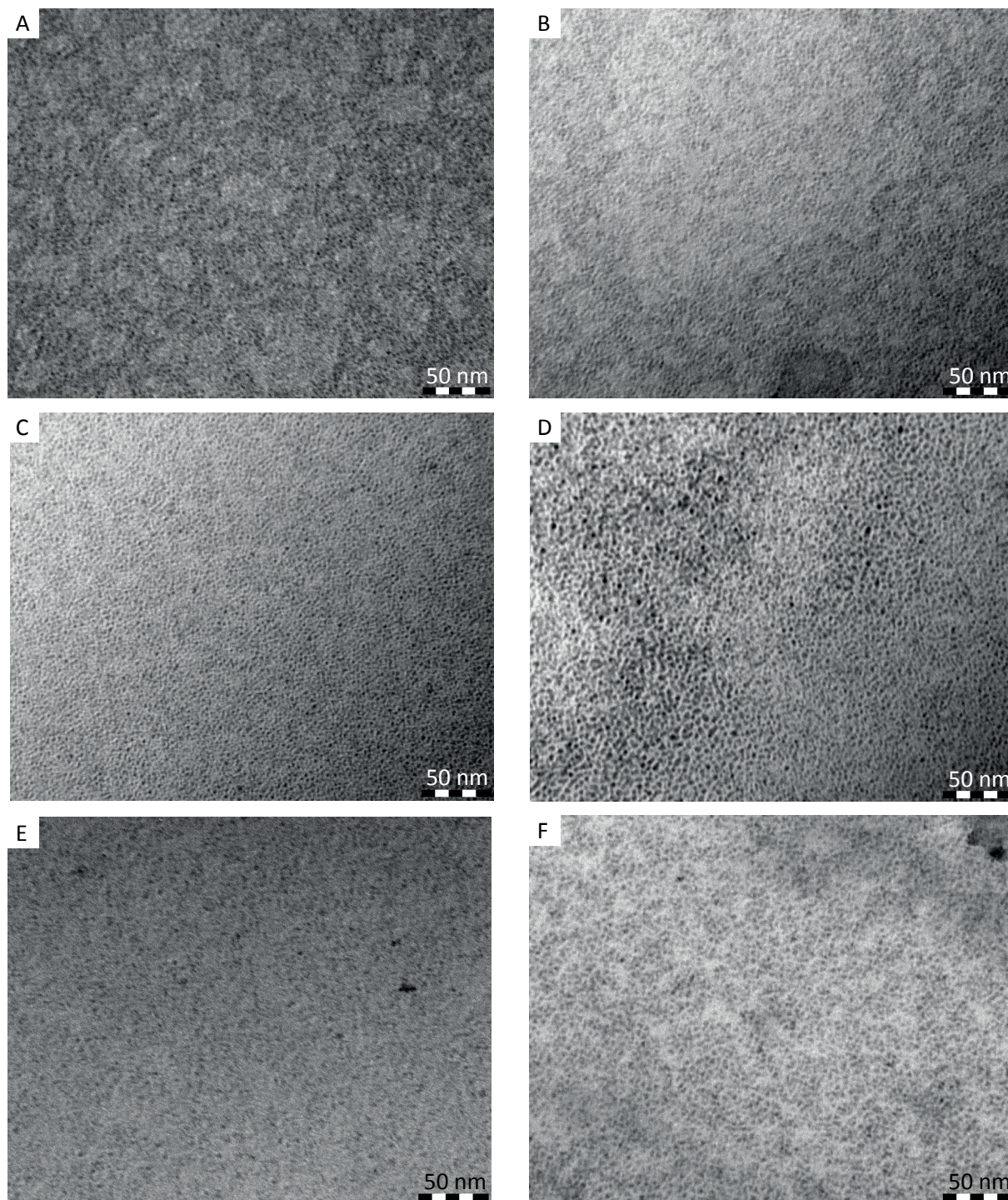


Figure 8.1. TEM pictures of several CIS samples discussed in chapter 3. A: AB 48, CIS NCs synthesized at 210 °C for 40 minutes. B: AB 8.4, CIS NCs synthesized at 210 °C for 40 min. C: AB 72; CIS NCs synthesized at 230 °C for 20 minutes. D: AB 73; CIS NCs synthesized at 230 °C for 11 minutes, under air. E: AB 16; CIS NCs synthesized at 230 °C for 11 minutes, with excess indium. F: AB 6; CIS NCs synthesized at 230 °C for 11 minutes with OA as extra ligand added.

Appendix C

Overview of QY estimations of several samples in chapter 4. See Appendix E for the exact reaction conditions per sample.

Table 8.2. Rough estimation of QY of several samples from chapter 4

Figure / sample	QY (%)
Figure 4.2	
AB 36; cores	12.4
AB 40.1 ; CIZS	17.3
AB 40.2; CIZS	17.9
AB 40.3; CIZS	22.2
AB 40.4; CIZS	22.0
AB 40.5; CIZS	25.4
AB 40.6; CIZS	18.1
AB 40.7; CIZS	26.7
AB 40.8; CIZS	28.2
AB 40.9; CIZS	30.3
Figure 4.4A	
AB 41; cores	0.3
AB 42.1; CIZS	1.0
AB 42.2; CIZS	1.0
AB 42.3; CIZS	0.9
AB 42.4; CIZS	1.3
AB 42.5; CIZS	1.4
AB 42.6; CIZS	1.4
Figure 4.6A	
AB 41; cores	0.3
AB 43.1 ; CIZS	3.9
AB 43.2; CIZS	5.9
AB 43.3; CIZS	5.5
AB 43.4; CIZS	7.1
Figure 4.6B	
AB 41; cores	0.3
AB 46.1; CIZS	3.6
AB 46.2; CIZS	6.2
AB 46.3; CIZS/Zns	8.3
AB 46.4; CIZS/ZnS	7.9

Appendix D

Proof of reproducibility of the CIS cores, see Figure 8.2.

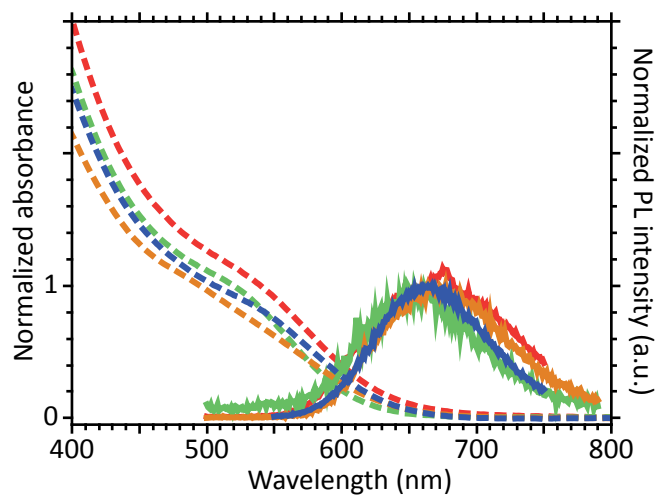


Figure 8.2. Absorption (dashed lines) and emission (full lines) spectra for four different CIS samples used as cores for the synthesis described in chapter 4. The absorption and emission spectra hardly shift, showing a good reproducibility.

Appendix E

Overview of synthesis conditions used for samples described in chapter 4.

Table 8.3. Overview of synthesis conditions used for CIS cores, CIZS NCs, CIZS/ZnS HNC and CIS/ZnS HNCs.

Sample	CIS cores	Shell precursors	Reaction temperature (°C)	Reaction time (min)	Method	Figure in chapter
AB 23	-	Zn stearate, DDT	210	90	heating up	Figure 4.3
AB 25.1	-	-	210	40	heating up	Figure 4.1A
AB 25.2	AB 25.1	Cd oleate, S	210	0	heating up	Figure 4.1A
AB 30.1	-	-	210	40	heating up	Figure 4.1B
AB 30.2	AB 30.1	Cd oleate, S	230	20	heating up	Figure 4.1B
AB 36	-	-	210	30	heating up	-
AB 40.1	AB 36	Zn stearate, DDT	150	30	hot injection	Figure 4.2
AB 40.2	idem	idem	150	60	sample	idem
AB 40.3	idem	idem	170	30	sample	idem
AB 40.4	idem	idem	170	60	sample	idem
AB 40.5	idem	idem	190	30	sample	idem
AB 40.6	idem	idem	190	60	sample	idem
AB 40.7	idem	idem	210	30	sample	idem
AB 40.8	idem	idem	210	60	sample	idem
AB 40.9	idem	idem	210	90	sample	idem
AB 41	-	-	210	25	heating up	-
AB 42.1	AB 41	Zn stearate, DDT	150	30	hot injection	Figure 4.4A
AB 42.2	idem	idem	idem	60	sample	idem
AB 42.3	idem	idem	idem	90	sample	idem
AB 42.4	idem	idem	idem	120	sample	idem
AB 42.5	idem	idem	idem	150	sample	idem
AB 42.6	idem	idem	idem	180	sample	idem
AB 43.1	AB 41	ZnCl ₂ , DDT	150	30	hot injection	Figure 4.6A
AB 43.2	idem	idem	idem	60	sample	idem
AB 43.3	idem	idem	idem	90	sample	idem
AB 43.4	idem	idem	idem	180	sample	idem
AB 46.1	AB 41	ZnCl ₂ , DDT	210	10	hot injection	Figure 4.6B
AB 46.2	idem	idem	idem	idem	sample	idem
AB 46.3	idem	idem	idem	idem	sample	idem
AB 46.4	idem	idem	idem	idem	sample	idem
AB 47.1	AB 41	Zn stearate, DDT	210	30	hot injection	Figure 4.4B
AB 47.2	idem	idem	idem	idem	sample	idem
AB 47.3	idem	idem	idem	idem	sample	idem
AB 47.4	idem	idem	idem	idem	sample	idem
AB 48	-	-	210	35	heating up	-
AB 52.1	AB 48	ZnCl ₂ , S-ODE	190	5	hot injection	Figure 4.7

Sample	CIS cores	Shell precursors	Reaction temperature (°C)	Reaction time (min)	Method	Figure in chapter
AB 52.2	idem	idem	idem	30	sample	idem
AB 52.3	idem	idem	idem	60	sample	idem
AB 52.4	idem	idem	idem	90	sample	idem
AB 55.1	AB 48	ZnCl ₂ , S-ODE, DDT	210	30	hot injection	Figure 4.8
AB 55.2	idem	idem	idem	60	sample	idem
AB 55.3	idem	idem	idem	90	sample	idem
AB 55.4	idem	idem	idem	120	sample	idem
AB 57.1	AB 48	ZnCl ₂ , S-ODE, OLAM	210	30	hot injection	Figure 4.9A
AB 57.2	idem	idem	idem	60	sample	idem
AB 57.3	idem	idem	idem	90	sample	idem
AB 57.4	idem	idem	idem	120	sample	idem
AB 59	-	-	210	40	heating up	-
AB 64.1	AB 59	ZnCl ₂ , S-ODE, OLAM	210	60	hot injection	Figure 4.11A
AB 64.2	idem	idem	idem	120	sample	idem
AB 64.3	idem	idem	idem	150	sample	idem
AB 64.4	idem	idem	idem	180	sample	idem
AB 67	AB 59	ZnCl ₂ , S-ODE, OLAM, ODA	210	80	drop wise addition	Figure 4.12A

Appendix F

HRTEM images and corresponding FFT of the lattice fringes of the hexagonal CIS/ZnS particles of chapter 4.

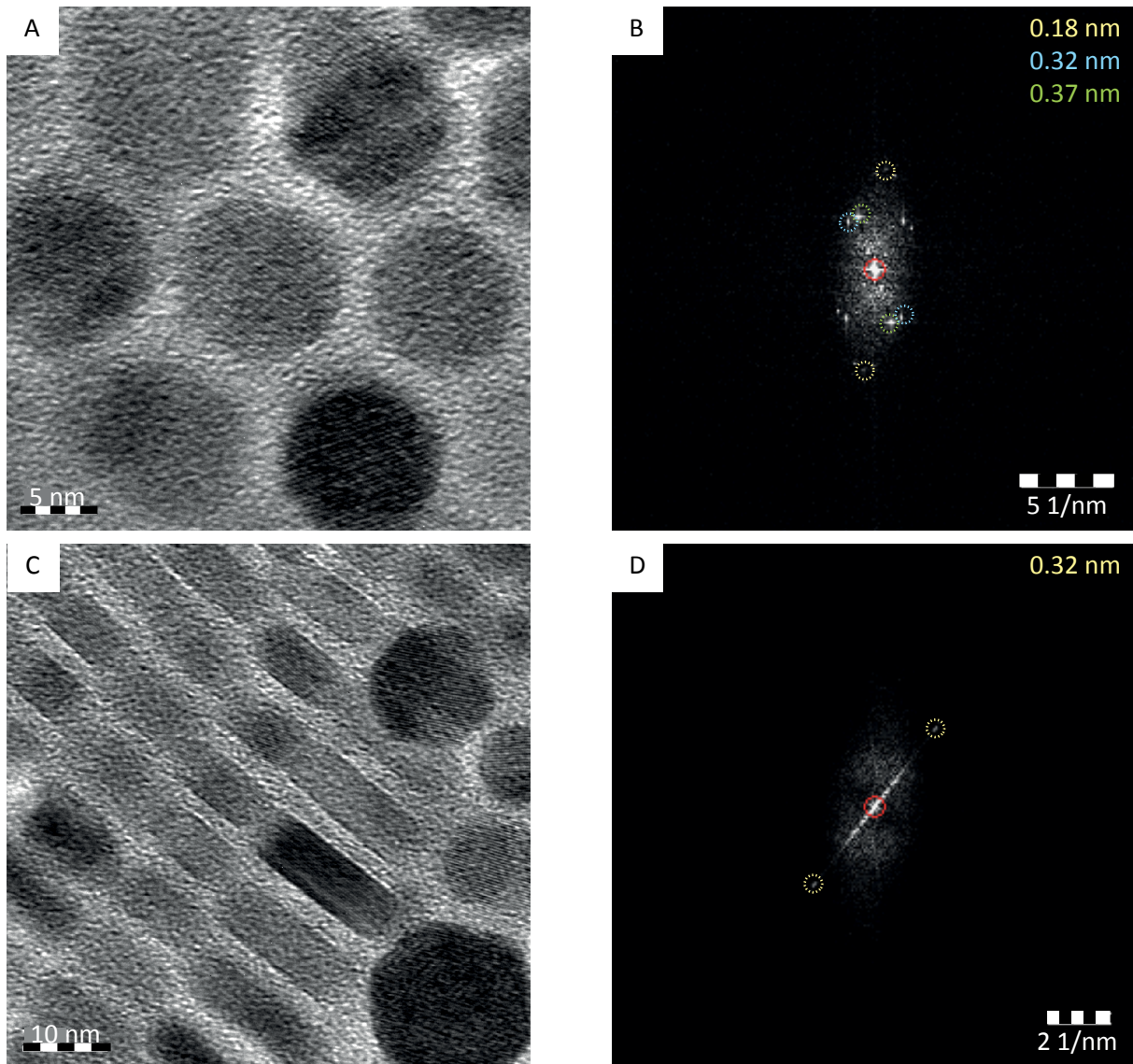


Figure 8.3. A: HRTEM image of the CIS/ZnS platelets on their back, B: corresponding FFT. C: HRTEM image of the CIS/ZnS platelets on their side, D: corresponding FFT. E: HRTEM image of the ripened CIS/ZnS HNCs, F: corresponding FFT.

Appendix G

Overview of synthesis conditions used for samples described in chapter 5.

Table 8.4. Overview of synthesis conditions used for cation exchange reactions

Sample	Seeds	Diameter (nm)	In precursor	Ligands (mL)	Solvent	Temperature (°C)	Time (hours)	Figure in chapter
AB 10.1	AB 5.1	13.5 ± 1.4	In(NO ₃) ₃	OLAM (0.5), TOP (3)	ODE	RT	1	Figure 5.1
AB 10.2	idem	idem	idem	idem	idem	RT	2	idem
AB 10.3	idem	idem	idem	idem	idem	50	1	idem
AB 10.4	idem	idem	idem	idem	idem	50	2	idem
AB 10.5	idem	idem	idem	idem	idem	100	1	idem
AB 11.1	AB 5.2	17 ± 1.5	idem	idem	idem	100	1	Figure 5.2
AB 11.2	idem	idem	idem	idem	idem	100	2	idem
AB 11.3	idem	idem	idem	idem	idem	150	1	idem
AB 11.4	idem	idem	idem	idem	idem	150	2	idem
AB 11.5	idem	idem	idem	idem	idem	200	1	idem
AB 74	idem	idem	idem	OA (0.5), TOP (3)	idem	100	1	x
AB 75	QA 103s1	4	idem	OLAM (0.5), TOP (3)	idem	idem	idem	idem
AB 19.1	QA 103s2	6	idem	OLAM (3)	idem	55	1	Figure 5.3A
AB 19.2	idem	idem	idem	idem	idem	100	1	idem
AB 19.3	idem	idem	idem	idem	idem	100	3	idem
AB 26	idem	idem	In(Ac) ₃	idem	idem	100	1	Figure 5.3B
AB 29	AB 27	gel	InCl ₃	OLAM (3), TOP (0.3)	idem	100-170-150	1.5-0.1-1	x
AB 31	AB 27	gel	idem	OLAM (0.5), TOP (0.3)	idem	100-190	0.5-2	idem
AB 44	AB 39	3.0 ± 0.5	In(NO ₃) ₃	OLAM (0.5, 1.5)	x	100-140	4-1	idem
AB 45	AB 39	3.0 ± 0.5	In(Ac) ₃	idem	idem	idem	idem	idem
AB 53	AB 39	3.0 ± 0.5	In(NO ₃) ₃	x	MeOH/TOL	RT	7 days	Figure 5.4A
AB 54	AB 39	3.0 ± 0.5	InCl ₃	idem	idem	idem	idem	Figure 5.4B

Sample	Seeds	Diameter (nm)	In precursor	Ligands (mL)	Solvent	Temperature (°C)	Time (hours)	Figure in chapter
WvdS 135	WvdS 120-2		In(NO ₃) ₃	idem	idem	idem	5 days	Figure 5.7
WvdS 137-1	JB 035		idem	idem	idem	idem	5 days	Figure 5.6

Appendix H

Overview of synthesis conditions used for samples described in chapter 6.

Table 8.5. Overview of synthesis conditions used for CIS samples

Sample	Cu : In ratio (mmol)	Reaction temperature (°C)	Reaction time (min)	Atmosphere	Figure in chapter
AB test	0.54:0.2	240	30	N ₂	Figure 6.6
AB 2	0.4:0.2	idem	idem	idem	Figure 6.11
AB 3	0.54:0.2	240,200	1,30	idem	Figure 6.7
AB 4	idem	200	30	idem	Figure 6.8
AB 5.1	idem	idem	60	idem	idem
AB 5.2	idem	idem	120	idem	idem
AB 7	0.4:0.2	240	30	Air	Figure 6.2
AB 9	0.54:0.2	200	2 days	N ₂	Figure 6.9
AB 12	0.2:0.2	240	30	Air	Figure 6.12
AB 17.1	0.4:0.2	200	-	idem	Figure 6.10
AB 17.2	idem	220	-	idem	idem
AB 17.3	idem	240	-	idem	idem
AB 17.4	idem	idem	10	idem	idem
AB 17.5	idem	idem	20	idem	idem
AB 17.6	idem	idem	30	idem	idem
AB 20	idem	250	15	idem	Figure 6.5
AB 24	0:0.2	250	30	idem	x
AB 28	idem	240	90	idem	Figure 6.13
AB 63	x	250	10	N ₂	Figure 6.14
AB 69.1	AB 63: 0.2	240	10	Air	idem
AB 69.2	idem	idem	20	idem	idem
AB 69.3	idem	idem	30	idem	idem

Appendix I

A description of the self-assembly protocols for AB7 and a brief overview of the results.

A. SA1:

100 μL AB 7 was mixed with 100 μL tetrachloroethylene and 20 μL oleic acid. Vial with TEM grid was tilted under an angle of $\pm 40^\circ$ above a heating plate at 75 $^\circ\text{C}$. After drying under air for a week, nothing was visible with TEM.

B. SA2:

50 μL AB 7 was mixed with 75 μL tetrachloroethylene and 10 μL oleic acid. Vial with TEM grid was tilted under an angle of $\pm 40^\circ$ above a heating plate at 75 $^\circ\text{C}$. Result after drying for four days under air and one night under vacuum is shown in Figure 8.4.

C.

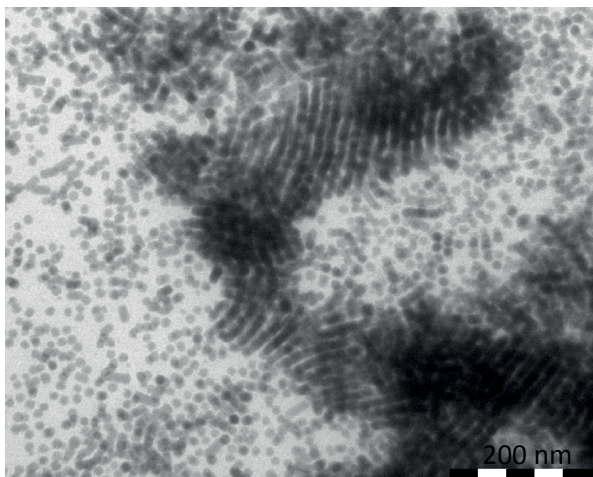


Figure 8.4. Result of SA2

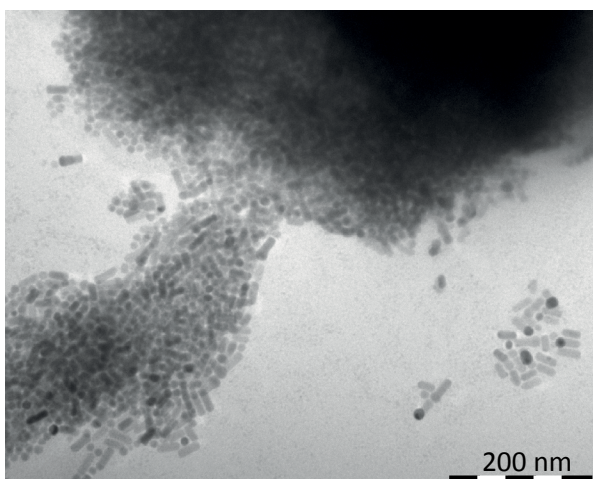
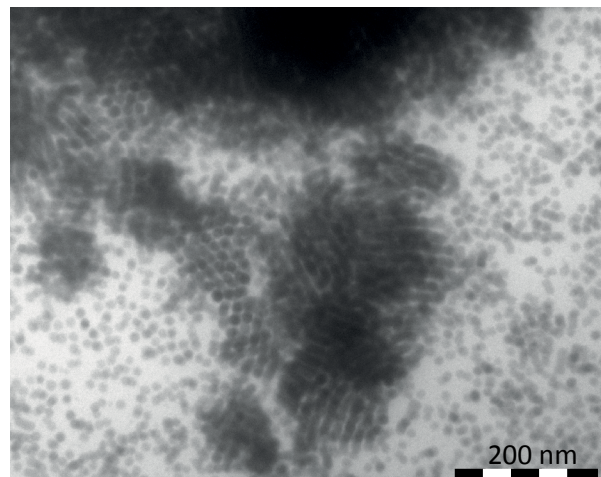
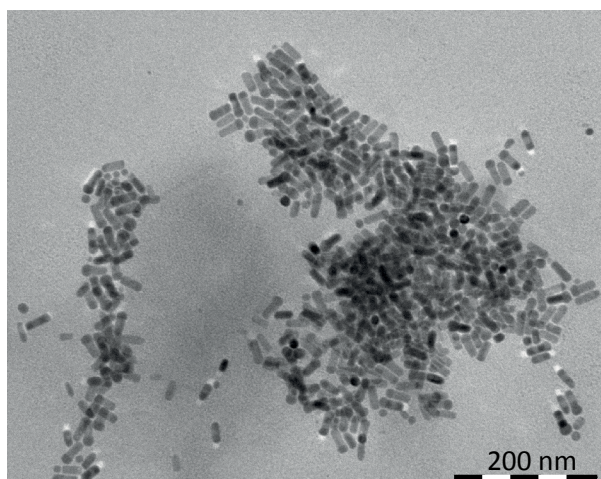


Figure 8.5. Result of SA3



D. SA 3:

50 μL AB 7 was added to 1 mL ethyleneglycol in a vial on a heating plate at 75 $^{\circ}\text{C}$. Result after drying for four days under air and 1 night under vacuum is shown in Figure 8.5.

E. SA 4:

50 μL AB7 was diluted with 50 μL TOL and three drops of this mixture were brought onto 1 mL ethyleneglycol. The result after drying for four days under air at a heating plate at 75 $^{\circ}\text{C}$ and one night under vacuum is shown in Figure 8.6.

F. SA 5:

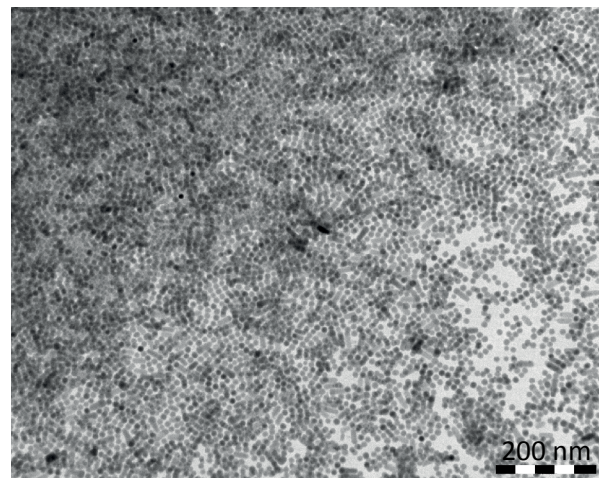
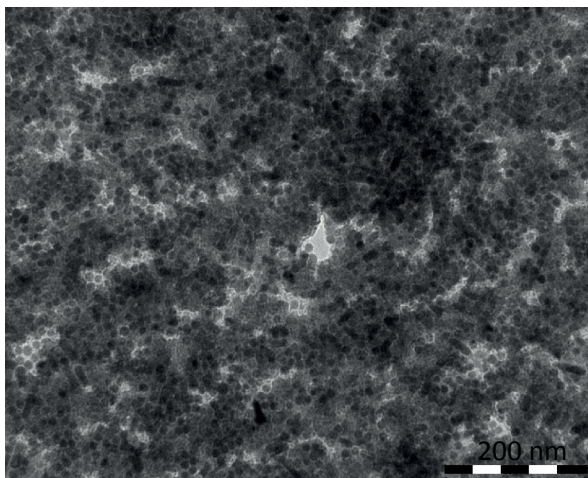


Figure 8.6. Result of SA4

25 μL AB7 was mixed with 50 μL tetrachloroethylene. Vial with TEM grid was tilted under an angle of $\pm 30^{\circ}$ above a heating plate at 75 $^{\circ}\text{C}$. Result after four days drying under air and one night under vacuum is shown in Figure 8.7.

G. SA 6:

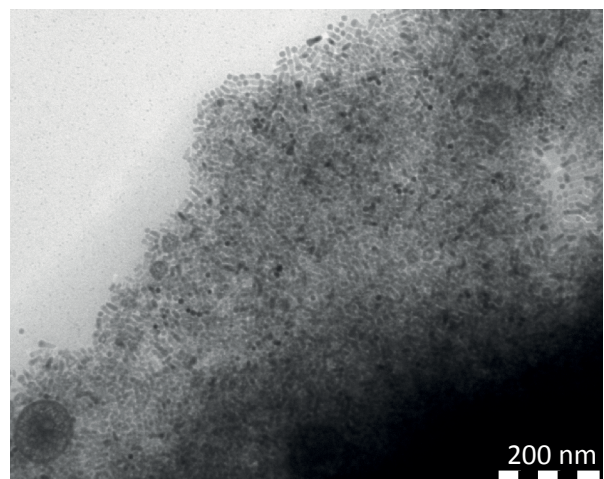
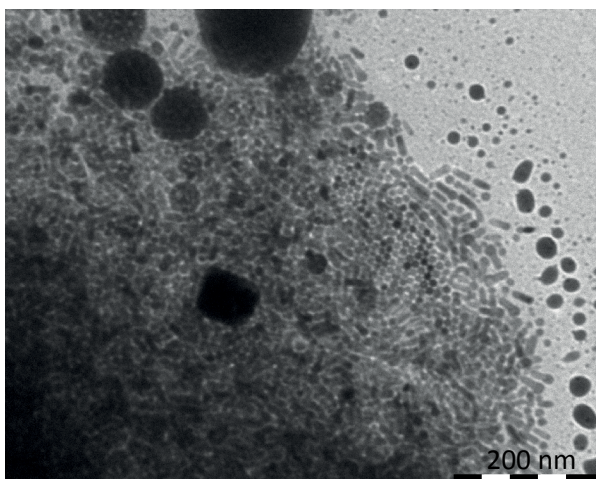


Figure 8.7. Result of SA5

50 μL AB7 was diluted with 50 μL TOL and one drop of this mixture was brought onto 1 mL ethyleneglycol. The result after drying for four days under air at a heating plate at 75°C and one night under vacuum is shown in Figure 8.8.

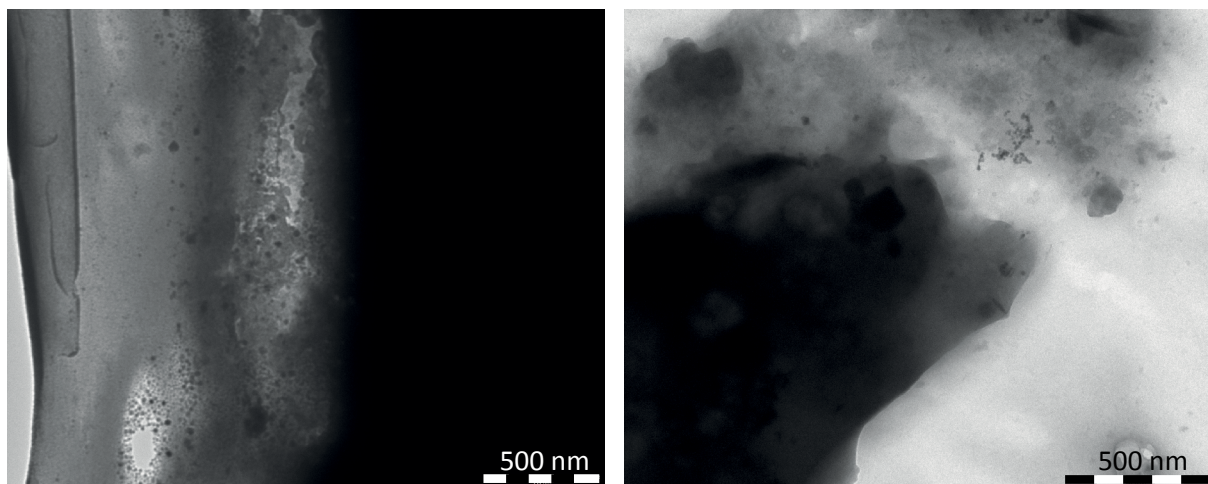


Figure 8.8. Result of SA6